Anthropogenic Changes in the Frequency and Severity of European Winter Storms:

Mechanisms, Impacts and their Uncertainties

Dissertation

zur Erlangung des akademischen Grades
eines Doktors der Naturwissenschaften
am Fachbereich für Geowissenschaften
der Freien Universität Berlin

vorgelegt von

Tobias Pardowitz

Berlin, 15. September 2014

(korrigierte Fassung vom 16. Dezember 2014)

1. Gutachter:	Prof. Dr. Uwe Ulbrich Institut für Meteorologie, Freie Universität Berlin
2. Gutachter:	PD Dr. Gregor C. Leckebusch School of Geography, Earth and Environmental Sciences, University of Birmingham
Disputationstermin:	15. Dezember 2014

Selbstständigkeitserklärung

Hiermit erkläre ich an Eides Statt, dass ich die vorliegende Arbeit selbstständig und ohne fremde Hilfe angefertigt, keine anderen als die angegebenen Quellen und Hilfsmittel benutzt und die den benutzten Quellen wörtlich oder inhaltlich entnommenen Stellen als solche kenntlich gemacht habe. Diese Arbeit hat in gleicher oder ähnlicher Form noch keiner Prüfungsbehörde vorgelegen.

Berlin, 15. September 2014

Contents

Abstract iii

Zusammenfassung v

1 Introduction 1
- 1.1 Objectives of the Thesis . . . 5
- 1.2 Outline of the Thesis . . . 5

2 Projected Changes in European Winter Storm Climate 9
- 2.1 Introduction and Current State of Research . . . 9
- 2.2 Data and Methods . . . 11
  - 2.2.1 Reanalysis Data . . . 11
  - 2.2.2 Global Climate Model Output . . . 11
  - 2.2.3 Wind Field Tracking . . . 12
  - 2.2.4 Storm Severity Index . . . 13
  - 2.2.5 Extreme Value Analysis . . . 15
- 2.3 Recent and Future Winter Storm Frequency . . . 20
  - 2.3.1 Statistical Uncertainty and Natural Variability . . . 24
  - 2.3.2 Scenario Uncertainty . . . 25
  - 2.3.3 Model Uncertainty . . . 27
- 2.4 Intensities of Recent and Future Winter Storms . . . 30
  - 2.4.1 Statistical Uncertainty . . . 35
  - 2.4.2 Scenario Uncertainty . . . 36
  - 2.4.3 Model Uncertainty . . . 37
- 2.5 Summary and Discussion . . . 41

3 Mechanisms Related to Changes in European Winter Storm Climate 45
- 3.1 Introduction and Current State of Research . . . 45
- 3.2 Data and Methods . . . 47
  - 3.2.1 Reanalysis Data . . . 47
  - 3.2.2 Global Climate Model Data . . . 47
  - 3.2.3 Assessment of the North Atlantic Oscillation . . . 48
  - 3.2.4 Eady Growth Rate . . . 49
  - 3.2.5 Hadley Cell Characteristics . . . 50
- 3.3 Changes in the North Atlantic Oscillation (NAO) . . . 50
  - 3.3.1 The NAO in Historical and Recent Climate . . . 50
  - 3.3.2 Future Changes in the NAO Strength . . . 51
  - 3.3.3 Changes in the NAO Shape . . . 52
- 3.4 Changes in Baroclinicity . . . 54
  - 3.4.1 Zonal Mean Eady Growth Rate . . . 54
  - 3.4.2 Changes in North Atlantic Eady Growth Rate . . . 55

3.4.3 Relation to the NAO . . . 56
3.5 NAO Influences on European Winter Storms and their Impacts . . . 57
3.5.1 Dependence of Winter Storm Frequency on the NAO . . . 57
3.5.2 Dependence of Storm Damages on the NAO Phase . . . 59
3.6 Tropical Origins of Changes in the North Atlantic Oscillation . . . 62
3.6.1 Assessment of Hadley Circulation Changes . . . 62
3.6.2 The Influence of the Hadley Circulation on the NAO . . . 64
3.6.3 A Rossby Wave Interpretation of the NAO . . . 68
3.7 Summary and Discussion . . . 72

4 Estimation of Impacts for Future Winter Storms 77
4.1 Introduction . . . 77
4.2 Current State of Research . . . 79
4.3 Data and Methods . . . 82
4.3.1 Insurance Data . . . 82
4.3.2 Reanalysis Data . . . 83
4.3.3 Regional Climate Model Data . . . 83
4.3.4 Wind Field Tracking for High Resolution Model Output . . . 84
4.4 Modeling of Storm Damages . . . 85
4.4.1 Basic Loss Model . . . 85
4.4.2 High-Resolution Refinement of the Storm Loss Model . . . 86
4.4.3 Optimization of Storm Damage Model . . . 88
4.5 Uncertainties in Regional Loss Projections . . . 91
4.5.1 Historical Losses . . . 92
4.5.2 Modeling Losses under Recent Climate Conditions . . . 94
4.5.3 Future Changes in Losses . . . 95
4.5.4 Uncertainties on Derived Changes . . . 96
4.6 Assessment of Dynamical Downscaling Uncertainties . . . 99
4.6.1 Ensemble Generation Technique . . . 101
4.6.2 Comparison of GCM and RCM . . . 102
4.6.3 Deriving Uncertainties in Modeled Storm Impacts . . . 103
4.6.4 Implications for Climate Change Assessment . . . 106
4.7 Estimates of Return Values for Loss Intensive Winter Storms . . . 107
4.7.1 Return Values of Historical Winter Storms . . . 107
4.7.2 Quantification of Uncertainties . . . 111
4.7.3 Derived Climate Change Signal and its Uncertainties . . . 118
4.8 Summary and Discussion . . . 120

5 Synthesis 125

Bibliography 131

A Supplementary Material 145

Acknowledgement 153

Abstract

The large scale fields of severe winds associated with deep extra tropical cyclones pose severe risks to society and economy by damaging both natural and man-made structures over vast areas. This work addresses anthropogenic changes in the frequency and intensity of European winter storm events, their potential impacts as well as the mechanisms related to such changes.

On the basis of global climate projections it is found, that severe wind storms over the North Atlantic are generally decreasing in terms of their frequency, however on a band across the North Atlantic and parts of Europe increased frequency of severe storms is identified in connection with increases in their intensities. Changes are consistently identified amongst multiple model projections and for different scenarios on future greenhouse gas emission. The strength of identified changes is however found to depend on the scenario and particularly on the considered climate model. For central Europe, increases in frequency towards the end of the 21st century are identified under SRES-A1B conditions, ranging between -11% and $+44\%$ and an ensemble average of 21%. In terms of intensity, storms affecting central Europe occurring once a year are found to increase in strength by about $+30\%$, with individual models projecting changes between -28% and up to $+96\%$. Considerable robustness of results is found, with 7 out of 8 simulations projecting both increased frequency and intensity of winter storms affecting central Europe.

With respect to underlying mechanisms for these changes, the relation to projected changes in the North Atlantic Oscillation (NAO), as well as changing baroclinic conditions of the atmosphere are investigated. It is found that the NAO undergoes fundamental changes with respect to both its phase as well as its shape. Consistent to diagnosed changes in storm frequency, the NAO is found shifting towards a more positive phase with its action centers shifting in north-eastward direction, which is related to more favorable growth conditions for cyclones over eastern parts of the North Atlantic and central Europe. The tropical influence on projected changes in the European storm climate are investigated by addressing the relation between the tropical Hadley circulation and the NAO, with a strong relation being identified between a projected northward expansion of the Hadley cell and changes in the NAO. Results from theoretical considerations, interpreting the NAO as a manifestation of a stationary Rossby wave induced by the overtopping zonal winds above the Rocky Mountains, are found to be well aligned with the projected eastward shift of the NAO action centers.

Compared to changes in the European storm climate on large scales, the assessment

of trends in storm related losses is associated with much larger uncertainty, which beside the large statistical uncertainty result from multiple uncertainty sources along the modeling chain. To quantify the uncertainty resulting from the dynamical downscaling of general circulation model (GCM) output, a methodology has been developed to generate high-resolution ensembles of potentially hazardous storms identified in GCM output. A large source of uncertainty is related to the modeling of local storm losses on the basis of near-surface wind gust estimates. Deriving storm-loss transfer functions on district level yields the advantage of including local differences in the vulnerability against severe winds, however uncertainties on determined vulnerability parameters are shown to be considerable. Grouping districts into larger regions is found to significantly reduce the involved uncertainty, correspondingly reducing the uncertainty inherent to future loss projections.

Besides addressing single sources of uncertainty, a methodology has been developed to derive cumulative uncertainty ranges on estimates of future return levels and return periods within an extreme value analysis framework. Results indicate, that under SRES-A1B conditions, the accumulated German wide losses of a winter storm event occurring once in 5 years increases towards the end of the 21st century by about +30%, with an estimated uncertainty ranging between −5% and +87%. Correspondingly, the return period of a 5 year event is found to decrease to about 4.3 years with an uncertainty range between 3.7 to 5.2 years. Even larger increases in losses and decreases in return periods can be identified for events being even more infrequent, however associated with strongly increasing uncertainties on these estimates.

Based on transient regional climate model (RCM) projections, German wide winter storm losses are found to increase by about +14% towards the end of the 21st century under SRES-A1B conditions, with individual RCM signals ranging between −14% and +39%, with 9 out of 12 models projecting increased losses. With respect to regional differences in such trends, north-western parts of Germany are found to be more affected with increases of up to 30% in ensemble average, while south-eastern parts feature only moderate increases in losses by about 5%.

Zusammenfassung

Die zerstörerische Wirkung extremer Winde im Zusammenhang mit intensiven extratropischen Zyklonen auf natürliche Ökosysteme und menschliche Strukturen stellt eine ernsthafte Bedrohung für Gesellschaft und Wirtschaft dar. Diese Arbeit untersucht anthropogene Änderungen in der Häufigkeit und Intensität Europäischer Winterstürme, potentielle Auswirkungen sowie Mechanismen welche im Zusammenhang zu diesen Änderungen stehen.

Auf Basis globaler Klimaprojektionen findet sich eine generelle Abnahme in der Häufigkeit von Winterstürmen über dem Nordatlantik, wobei es auf einem Band über dem Nord Atlantik und Teilen Europas zu einer Zunahme potentiell schadenrelevanter Sturmsysteme kommt, verbunden mit einer Intensivierung dieser Systeme. Diese Änderungen können dabei in Projektionen mit unterschiedlichen Globalmodellen sowie für verschiedene Szenarien bzgl. zukünftiger Treibhausgasemissionen identifiziert werden, wobei die Stärke der diagnostizierten Änderungen vom untersuchten Szenario und vor allem vom untersuchten Modell abhängt. Für Zentraleuropa kann für das Ende des 21. Jahrhunderts unter SRES-A1B Bedingungen eine Änderung in der Häufigkeit von Sturmereignissen zwischen -11% und $+44\%$ festgestellt werden, wobei das Ensemble Mittel eine Zunahme um 21% zeigt. Darüber hinaus finden sich Änderungen in der Intensität einjährig wiederkehrender Winterstürme in Zentraleuropa, welche einer Zunahme um $+30\%$ entsprechen, wobei individuelle Modellläufe Änderungen zwischen -28% und $+96\%$ projizieren. Die Robustheit der Ergebnisse wird dadurch unterstrichen, dass 7 von 8 Simulationen eine Zunahme in sowohl der Häufigkeit als auch Intensität von Winterstürmen in Zentraleuropa projizieren.

Im Hinblick auf zugrundeliegende Mechanismen wird in der Arbeit sowohl die Beziehung zu Änderungen in der Nord Atlantischen Oszillation (NAO), sowie die Änderung in den baroklinen Eigenschaften der Atmosphäre untersucht. Dabei können fundamentale Änderungen der NAO identifiziert werden, sowohl bezüglich ihrer Phase als auch ihrer Form. Konsistent zu den Änderungen in der Sturmhäufigkeit findet sich eine Verschiebung hin zu positiveren Phasen der NAO, wobei sich ihre Aktionszentren in nordöstliche Richtung verschieben, welches mit günstigeren Wachstumsbedingungen für Zyklonen über dem östlichen Nordatlantik und über Europa einhergeht. Ein tropischer Einfluss auf Änderungen im Europäischen Sturmklima wird untersucht, indem eine Beziehung zwischen Eigenschaften der Hadley Zirkulation und der NAO hergestellt wird. Dabei findet sich ein enger Zusammenhang zwischen einer nordwärts Ausdehnung der Hadley Zelle und den projizierten Änderungen der NAO. Theoretische Betrachtungen

der NAO als Ausprägung einer stationären Rossby Welle, induziert durch die zonale Anströmung der Rocky Mountains können dabei in Einklang gebracht werden mit der diagnostizierten ostwärts Verschiebung der NAO Aktionszentren.

Im Vergleich zu großskaligen Änderungen im Europäischen Sturmklima unterliegt die Abschätzung von Trends in sturminduzierten Schäden deutlich größeren Unsicherheiten, welche neben großen statistischen Unsicherheiten auf eine Reihe von Unsicherheitsquellen in der Modellkette zurückzuführen sind. Um die Unsicherheiten der dynamischen Regionalisierung globaler Klimamodelle (GCM) zu quantifizieren, wurde eine Methodik entwickelt um hochaufgelöste Ensemble Simulationen potentiell schadenrelevanter Sturmereignisse zu generieren. Eine große Unsicherheitsquelle stellt außerdem die Modellierung lokaler Sturmschäden auf Basis bodennaher Winden dar. Sturmschaden-Transferfunktionen können dabei auf Landkreisebene abgeleitet werden, mit dem Vorteil, dass lokale Vulnerabilitäten bzgl. extremer Winde abgebildet werden. Dabei entstehen jedoch große Unsicherheiten auf abgeleitete Modellparameter. Durch Zusammenfassen von Landkreisen zu größeren Regionen können diese signifikant reduziert werden, wodurch eine entsprechende Reduktion der Unsicherheit auf projizierte Schäden erreicht wird.

Um die separat quantifizierten Unsicherheitsquellen zu Gesamtunsicherheiten zu integrieren, wurde ein Verfahren entwickelt um die kumulativen Unsicherheitsspannen auf abgeleitete Wiederkehrniveaus und Wiederkehrperioden im Rahmen der Extremwertstatistik zu berechnen. Dabei zeigen die Ergebnisse, dass unter SRES-A1B Bedingungen der Deutschlandweite Schaden von Winterstürmen mit einer Wiederkehrperiode von 5 Jahren um etwa +30% zunimmt, mit einer Unsicherheitsspanne zwischen −5% und +87%. Entsprechend reduzieren sich die Wiederkehrperioden von 5 Jahren auf etwa 4.3 Jahre, mit einer Unsicherheitsspanne zwischen 3.7 und 5.2 Jahren. Für seltenere Ereignisse finden sich sogar stärkere Zunahmen in Schäden und entsprechend Abnahmen in den Wiederkehrperioden, wobei diese Abschätzungen mit deutlich größeren Unsicherheiten behaftet sind.

Auf Basis transienter regionaler Klimaprojektionen findet sich eine Zunahme Deutschlandweiter Schäden um +14% zum Ende des 21. Jahrhunderts unter SRES-A1B Bedingungen, wobei die Signale individueller Projektionen zwischen −14% und +39% liegen und 9 von 12 Modellsimulationen eine Zunahme projizieren. Im Hinblick auf regionale Unterschiede in diesem Trend, findet sich eine stärkere Betroffenheit der nordwestlichen Regionen Deutschlands mit einer Zunahme der Sturmschäden um etwa 30% im Ensemble Mittel. Für südwestliche Regionen hingegen finden sich nur moderate Änderungen der Schäden um etwa +5%.

Chapter 1

Introduction

Severe weather poses serious threats to both property and lives even in highly developed countries such as Germany. Long lasting heat waves in combination with severe drought conditions, severe and large scale rainfall causing major river flooding, severe wind storms associated with deep extra tropical cyclones and severe weather related to small scale convective events belong to the most relevant and costliest natural hazards within Europe and Germany. Causing about 30000 fatalities in Europe and major impacts on agriculture and forestry (UNEP, 2004), the 2003 heat wave can be considered the by far most harmful natural disaster in Europe with few -if any- events impacting the European society comparably within the past 100 years. With respect to economic losses however, the 2002 flood has been the costliest natural disaster in Germany since 1980 causing 11.6 billion US $ of economic losses, followed by winter storm Kyrill in 2007 (5.5 billion US $) and the severe thunderstorms related to the cold front passage of cyclone Hilal in May 2008 (1.7 billion US $) (MunichRe, 2012). Winter storms in particular pose severe risks to communities and insurances, since their large scale wind fields may damage building structures, infrastructure but also natural structures across vast areas, often severely affecting multiple countries within Europe (Fink et al., 2009). Moreover damaging winter storms occur on a rather "regular" basis, under particular large-scale atmospheric conditions even occurring in serial clusters with sequences of severe storms occurring within short times (Pinto et al., 2013), leading to disastrous accumulation of losses, as demonstrated by the storm series of 1990 (Daria, Vivian, Wiebke) and 1999 (Anatol, Lothar, Martin). Compared to other natural disasters in Germany, winter storms accounted for about 53% of economic losses and 64% of insured losses in the period 1970-1998 (MunichRe, 1999), distinctly exceeding impacts due to thunderstorm and hail events causing losses on a much more frequent basis however restricted to rather restricted areas in most cases. These accumulated damages of single severe winter storm events thus pose additional risks e.g. to insurance companies active in limited areas or specific sectors, but also to communes or states by exceeding their regional coping capacities.

Meteorological extreme events are likely to be altered under changed climate conditions, with respect to both frequency and intensity (IPCC, 2007a) severely impacting ecosystems, water resources, human health, agriculture and industry (IPCC, 2007b). There is evidence from observations that some extremes have changed in the past decades

as a result of anthropogenically forced increases in atmospheric concentrations of greenhouse gases (IPCC, 2012). In particular there are indications that decreases in the number of cold days and nights, increases in the frequency of heavy precipitation events in some regions and related flood events at regional scales, more intense and longer droughts and increases in coastal high water have occurred since the 1950s (IPCC, 2012). However, there are few data on extreme events available to make assessments regarding changes in their frequency or intensity, which leads to large uncertainties in trends of rare events, particularly on regional-scales (IPCC, 2012). Even though detection of long-term changes in cyclones are hindered by incomplete and changing observation systems leading to large uncertainties in detected trends, extreme extratropical storms are likely to have increased in frequency and intensity with a poleward shift in their tracks (IPCC, 2012). There are indications for an increase in storminess over Europe that has occurred during the past century (Donat et al., 2011c) with results suggesting that the identified trends may at least partly be a consequence of increasing GHG concentrations. However, large uncertainty remains whether these changes can be attributed to be anthropogenically forced or rather being an expression of (multi-) decadal variability. Higher confidence is found for increases in economic losses from weather- and climate-related disasters during the past decades, with increased exposure of people and economic assets being the major cause of those long-term increases (IPCC, 2012).

Based on global and regional climate model projections, continued emissions of greenhouse gases are found to cause further warming and changes in all components of the climate system during the 21st century (IPCC, 2013) intensifying trends in meteorological and climatological extremes, in particular in temperature and precipitation extremes. While in general the frequency of extratropical storms is likely to decrease in projected climates, the occurrence of severe storms is found to increase in some regions including parts of Europe. Recent studies identify increasing numbers of intense cyclones on a rather narrow pathway along the eastern Atlantic, the British Isles, the North Sea and southern Scandinavia, being related to changes in both frequency and intensity of extreme wind speeds over central and western Europe (Leckebusch and Ulbrich, 2004; Donat et al., 2010b). Furthermore, a robust feature identified in climate model projections is that extratropical storm tracks will tend to shift poleward, leading to a weakening of the Mediterranean storm track and a strengthening of the storm track north of the British Isles (Bengtsson et al., 2006; Ulbrich et al., 2009). It was noted however, that substantial uncertainties remain in projected changes in northern hemisphere winter storm tracks, especially for the North Atlantic basin (IPCC, 2013). This is particularly true when considering changes in high-impact storm events for which statistical sample sizes are limited.

By means of an event based identification of potentially hazardous storm events over

Europe, global climate projections shall be investigated in Chapter 2, studying possible changes in their frequency-intensity distribution under changed climate conditions. Such assessment is subjected to large uncertainties resulting from multiple sources, e.g. arising from assumptions on future socio-economic development, modeling uncertainties arising from the design of -and the simplifications necessary to run- global climate models at rather course resolutions and from statistical sampling uncertainties. Thus it shall be investigated, how the changes depend on the considered emission scenario as well as the climate model under investigation. Furthermore, statistical uncertainties resulting from limited statistical sample sizes shall be quantified, particularly for rare events in the framework of extreme value analysis.

Much of the mechanisms and driving factors for changes in extra tropical cyclones still need understanding with links between surface warming, extratropical storms and their influence on climate being more complex than simple responses to changes in global mean surface temperatures or baroclinicity (O'Gorman, 2010; IPCC, 2013). Besides quantifying changes in European winter storm climate, it is thus of great interest to investigate on the possible mechanisms related to such changes. Environmental factors contributing directly to the genesis and intensification of cyclones have been broadly investigated in the past, including factors such as the availability of latent heat, the presence of upper-air divergence in particular close to the jet exit region as well as upper-air baroclinicity. It shall be investigated, in how far projected changes in the temperature profile of the atmosphere alter the large scale baroclinic conditions of the atmosphere, possibly leading to changes in the storm climate of the mid-latitudes. Since the North Atlantic Oscillation (NAO) can be attributed to much of European climate variability and is strongly related to the occurrence of European winter storms, the NAO shall be investigated with respect to possible changes under future climate conditions. Variability of the North Atlantic Oscillation (NAO) occurs on a broad range of time scales, with driving factors and related mechanisms still being under debate (Pinto and Raible, 2012). Especially with respect to low-frequency variability and long term changes, no consensus has been found so far regarding the processes responsible for variations of the NAO. Besides external parameters like volcanos, solar activity, or stratospheric-tropospheric coupling, there is evidence for tropical origins of long term changes of the NAO (Hoerling et al., 2001; Hurrell et al., 2004). The tropical influence on projected changes of the NAO shall thus be highlighted, investigating on possible dynamical mechanisms for these teleconnections.

Anthropogenic changes in meteorological extremes will very likely have greater societal impacts and cause more serious disaster losses towards the end of the 21st century, especially impacting sectors with close links to climate, with increases strongly amplified by drivers of socioeconomic nature (IPCC, 2012). Where extreme weather events become more intense and/or more frequent, the economic and social costs of those events

will increase, with increases being substantial in the areas most directly affected (IPCC, 2007b). An increased frequency and intensity of severe winter storms related to deep extra tropical cyclones will thus be likely to have greater impacts causing increased losses in Europe and Germany. However, multiple sources of uncertainty can be identified when quantifying future storm impacts. Besides uncertainties about future emission scenarios, model simplifications in both global and regional climate models, the downstream modeling of storm impacts introduces additional uncertainties, e.g. related to the availability of suitable historical impact data and the statistical modeling to derive key parameters such as vulnerability and exposure. Since the impacts of severe weather are extremely multi-facetted, with multiple consequences of meteorological hazards being difficult to quantify, it is almost impossible to comprehensively estimate the impacts of future winter storms. However for specific sectors, particularly those covered by insurance, data on the impacts of severe weather exists in a good quality over the past decades. Such data, allowing for a statistical modeling of weather related impacts based on meteorological parameters, can thus be used to derive specific vulnerabilities towards specific hazards, e.g. the vulnerability of housing in Germany towards the occurrence of extreme wind speeds. Based on a simple approach to model winter storm losses in Germany (Klawa and Ulbrich, 2003) a refinement to include local vulnerabilities has been developed (Donat et al., 2011b) which shall be analyzed with respect to resulting uncertainties in the derived wind-loss transfer functions. It shall be investigated, in how far projections of winter storm losses on regional or local scales are reasonable by means of such storm-loss model, particularly in light of the large uncertainties involved in projecting changes of local wind extremes. As noted at the beginning, the accumulation of damages for single events poses one of the major risks imposed by severe winter storms, e.g. to insurance companies active in limited areas or specific sectors, but also to communes or states. In light of adaptation measures it is thus of great value, to be able to to estimate possible impacts of extreme winter storm events in future climate conditions. Changes in the risk of severe winter storm events shall thus be assessed by means of extreme value analysis, estimating return periods and return levels of high-impact events in recent and future climate conditions. With multiple sources of uncertainty affecting such estimates, a special focus will be on the quantification of uncertainties arising along the modeling chain.

1.1 Objectives of the Thesis

As stated in the previous introduction, this thesis aims at quantifying potential changes in the European severe winter storm climate, estimating potential impacts of severe winter storms under anthropogenic climate change and investigate on possible mechanisms related to such changes. The underlying questions of this thesis, arising from these three main objectives are summarized in the following.

Projected Changes in European Winter Storm Climate

- Which changes in the frequency of severe European winter storms are projected under anthropogenic climate change?
- Does the intensity of European winter storms change under anthropogenic climate change?
- Which uncertainties are associated with these estimations?

Mechanisms for Changes in European Winter Storm Climate

- Which changes in the North Atlantic Oscillation (NAO) are projected under anthropogenically changed climate conditions?
- How do environmental factors favoring the genesis and growth of mid-latitude cyclones change under altered climate conditions?
- Are there tropical influences related to changes in the European winter storm climate and the NAO?

Estimation of Impacts for Future Winter Storms

- Which changes in winter storm losses in Germany can be derived from regional climate projections?
- In how far can changes in regional impacts be discriminated within Germany?
- Which uncertainties are associated with projections of future winter storm losses?

1.2 Outline of the Thesis

The remainder of this thesis is organized according to these three underlying main objectives. Chapter 2 deals with the assessment of changes in frequency and intensities of winter storms, starting by introducing the analyzed global climate model projections, methods for the identification and characterization of severe wind storms and the methodologies

employed for the assessment of return characteristics by means of extreme value analysis. Projected changes in the European winter storm climate are subsequently analyzed in terms of their frequency, followed by an analysis of return periods and return levels of severe storm systems and closing with a summary and discussion of obtained results.

Chapter 3 discusses the Mechanisms for Changes in European winter storm climate, starting with a description to the analyzed data and the methodologies to assess and characterize the North Atlantic Oscillation, baroclinicity in terms of the Eady growth rate and the tropical Hadley cell. It follows an analysis of projected changes in the North Atlantic Oscillation and it's relation to European winter storms as well as the assessment of baroclinicity changes over Europe. Subsequently, tropical influences on mid-latitude storm climate and particularly the NAO is addressed, before closing the chapter with a discussion of results.

In Chapter 4, methods to assess losses caused by future winter storm events are developed and applied to regional climate model output. After introducing the analyzed model data, a description of the methodology to model winter storm damages is given, particularly addressing the uncertainties involved. Subsequently results applying such model to regional climate model projections are presented, analyzing possible regional trends in storm losses. Furthermore, an ensemble generation methodology to derive uncertainty information for regional climate simulations of severe winter storms is presented demonstrating its use in the estimation of uncertainty ranges of resulting winter storm impacts. Based on such ensemble simulations for a set of recent and future winter storms identified from global climate model simulations it is demonstrated, how changes in the return values of loss intensive winter storms over Germany can be derived quantifying the cumulative uncertainties arising from different steps in the modeling chain.

Finally, in Chapter 5 a synthesis of the results presented in this work is given.

Parts of this thesis have been published previously. This is the case for Section 4.7, with results on the estimation of return values of historical and future loss intense storm events in Germany published in

> Donat, M. G.; **Pardowitz, T.**; Leckebusch, G. C.; Ulbrich, U. und Burghoff, O. (2011b) High-resolution refinement of a storm loss model and estimation of return periods of loss-intensive storms over Germany. *Natural Hazards and Earth System Sciences*, 11, 2821-2833. The final publication is available at http://dx.doi.org/10.5194/nhess-11-2821-2011

> Held, H.; Gerstengarbe, F.-W.; **Pardowitz, T.**; Pinto, J. G.; Ulbrich, U.; Born, K.; Donat, M. G.; Karremann, M. K.; Leckebusch, G. C.; Ludwig, P.; Nissen, K. M.; Oesterle, H.; Prahl, B. F.; Werner, P. C.; Befort, D. J. und Burghoff, O. (2013) Projections of global warming-induced impacts on winter storm losses in the German

private household sector. *Climatic Change*, 121, 195-207. The final publication is available at Springer via http://dx.doi.org/10.1007/s10584-013-0872-7

The approach to estimate uncertainties from high resolution simulations of extreme wind storms and consequences for impacts presented in Section 4.6 has furthermore been submitted for publication to *Meteorologische Zeitschrift*

Pardowitz, T.; Befort, D. J.; Leckebusch, G. C. and Ulbrich, U. (2014) Estimating uncertainties from high resolution simulations of extreme wind storms and consequences for impacts. Submitted to *Meteorologische Zeitschrift*.

Chapter 2

Projected Changes in European Winter Storm Climate

2.1 Introduction and Current State of Research

The large-scale wind fields related to deep extra-tropical cyclones are the most destructive natural hazards present in Europe. About 50% of economic losses are caused by such winter storms (MunichRe, 1999, 2007). On average nearly 3 billion € total economic losses are caused per year by winter storms. These losses are mainly dominated by few single extreme winter storms such as Daria in 1990 with insured losses of roughly 10 billion € or Lothar in 1999 with losses of more than 7 billion €. The total economic losses of such extreme winter storms are of course much larger. The cyclone activity has been subject of several previous studies analyzing transient model simulations under increased Green-House Gas (GHG) concentrations. These studies agree with respect to the finding, that the total number of cyclones is likely to decrease in a climate of increased GHG concentrations (Knippertz et al., 2000; Lambert and Fyfe, 2006; Leckebusch et al., 2006). Also a pole-ward shift of cyclone activity can be identified on the northern hemisphere (Bengtsson et al., 2006; Knippertz et al., 2000). Unlike the decreasing trend in the total number of cyclones, studies reveal an increase in extreme cyclone activity for western central Europe (Leckebusch et al., 2006) as well as an intensification of storm related cyclones over the eastern Atlantic, the British Isles and the North Sea (Donat et al., 2010a). By means of extreme value analysis, it can be found that related to this increase in the number of intense cyclones, the return period of extreme cyclones is found to decrease for the British Isles, North Sea and Western Europe (Della-Marta and Pinto, 2009). Based on wind speed, investigations reveal an increase in the number of storm days for central Europe (Donat et al., 2010a), also related to increased mean wind speed as well as an increase of extreme wind speeds over North Europe and parts of the East Atlantic (Knippertz et al., 2000; Leckebusch et al., 2006).

This study is based on the so called storm severity index (SSI) which is an integrated measure for the meteorological strength of a storm system (Leckebusch et al., 2008). The base for the calculation of the SSI is a tracking algorithm, which constructs tracks of wind field clusters, which are defined by spatially adjacent exceedance of wind speed above a

local threshold. The calculation of the SSI is based purely on wind speeds close to ground and takes into account duration and extension of the wind fields. It is thus an objective measure for the potential impact of a cyclonic wind storm. Using the SSI values calculated from transient model simulations, extreme value analysis can be performed and results for the change in strength as well as frequencies of extreme storms can be derived. This contrasts to studies performing extreme value analysis based on core-pressure of cyclones (Della-Marta and Pinto, 2009) or single location (or gridded) wind speeds (Della-Marta et al., 2008; Hofherr and Kunz, 2010; Kunz et al., 2010).

The aims of this study are to evaluate (a) the uncertainties associated with estimates on the frequency of future severe winter storms over Europe as well as (b) their intensity-frequency distribution by means of extreme value statistics. The possible range of climate change signals for different emission scenarios shall be investigated to estimate uncertainties due to the specified climate forcing. Also a multi model ensemble shall be investigated to study the uncertainty associated with the model response to a specified climate forcing. To differentiate uncertainties due to different model responses from internal model variability, multi model results shall be compared to single model ensemble simulations. Finally, uncertainty ranges due to the different sources shall be compared, to deduce the individual contributions of each of the uncertainty sources to the overall uncertainty involved.

To do so, the wind field tracking algorithm described in Section 2.2.3 is applied to the reanalysis data set ERA-Interim for the Period 1979-2010 as well as for the individual model simulations described in Section 2.2.2. Resulting tracks and their associated storm severity values are evaluated with respect to the number of storm systems followed by an analysis of their frequency-intensity distribution by means of extreme value analysis.

2.2 Data and Methods

2.2.1 Reanalysis Data

The ERA-Interim reanalysis data set (Dee et al., 2011) is used. The reanalysis is computed on a T255 grid with 60 vertical model layers, supplying data on a grid with spacing of about 0.70° (≈ 79km) and is available for the period 1979-2010. 6 hourly instantaneous winds (at 0:00, 6:00, 12:00 and 18:00 UTC) in 10 m height are used as input for the wind field tracking algorithm as described in Section 2.2.3. To identify storm systems relevant for Europe, the region -60°E to 60°E and 25°N to 75°N is selected, thus including regions of high cyclogenesis in the north Atlantic. Tracking is applied to the winter months October through March, which is also the period used to calculate the 98th percentile of wind speeds to be used as a threshold in the wind field tracking.

Additionally the ERA-40 reanalysis (Uppala et al., 2005) is evaluated for the period 1958-2001. As for ERA-Interim, 6 hourly instantaneous winds at 0:00, 6:00, 12:00 and 18:00 UTC are used as input for the wind field tracking. The horizontal resolution is approximately 1.125°x 1.125° (T159). To evaluate possible dependencies of tracking results from the horizontal resolution, ERA-40 reanalysis data is interpolated onto a regular grid with 2.5°x2.5°, as well as 3.5°x3.5°. This corresponds to typical resolution of global climate model data (see following section).

2.2.2 Global Climate Model Output

Model	Institution	Resolution	# runs	References
BCCR-BCM2	Bjerkness Centre for Climate Research	T63, L45	1	(Furevik et al., 2003)
CNRM-CM3	Météo France/Centre National de Recherches Météorologiques	T63, L31	1	(Salas-Melia et al., 2005)
DMI-ECHAM5	Danish Meteorological Institute	T63, L31	1	(Jungclaus et al., 2006)
FUB-EGMAM	Freie Universität Berlin, Institut für Meteorologie	T30, L39	1	(Manzini and McFarlane, 1998; Legutke and Voss, 1999; Huebener et al., 2007)
IPSL-CM4	Institut Pierre Simon Laplace	2.5°x3.75°, L19	1	(Marti et al., 2005)
MPI-ECHAM5	Max Planck Institute for Meteorology	T63, L31	3	(Jungclaus et al., 2006)

Table 2.1: General Circulation Model (GCM) simulations analyzed from the ENSEMBLES project (van der Linden et al., 2009).

A multi-model ensemble consisting of 8 General Circulation Models (GCM, coupled atmosphere ocean models) simulations carried out in the framework of the ENSEMBLES project (van der Linden et al., 2009) is analyzed. The control period 1860-2000 (20C) of these simulations is forced with greenhouse gas (GHG) concentrations according to recent observations. Climate projections for the period 2001-2100 are forced with GHG concentrations following the SRES-A1B Scenario (Nakicenovic et al., 2000). The horizontal resolutions of the GCMs range from T30 corresponding to roughly 3.75° in FUB-EGMAM to T63 (1.875°) in the MPI-ECHAM5 simulations. Details can be found in Table 2.1. Maximum wind speed of the last 6 hours for the times 00, 06, 12 and 18 UTC is used. This quantity however is not available for some models (DMI-ECHAM5, BCCR-BCM2 and CNRM-CM3) and the instantaneous wind speeds at the given 6 hour intervals are used instead. In a different context it has been shown, that when considering the daily maximum wind speed differences are small between the maximum of 4 instantaneous values or the total maximum (Pinto et al., 2007). Additionally, a single model but multi-scenario ensemble using MPI-ECHAM5 model simulation runs is analyzed. For each of the SRES scenarios A1B, A2 and B1 a 3 run ensemble is available. As for the reanalyses, wind field tracking is applied to the winter half year (October through March), for the region -60°E to 60°E and 25°N to 75°N.

2.2.3 Wind Field Tracking

Reanalysis data as well as global climate model output is analyzed using a wind field tracking algorithm as described in Leckebusch et al. (2008). In the first step, the algorithm detects spatially contiguous clusters of wind speeds exceeding the local 98th percentile, calculated for the winter months October through March. In general the period 1971-2000 is used as a reference period for which the percentile is calculated, however in the case of ERA-Interim the reference period has been adopted to the available period 1979-2010. In the schematic representation in Figure 2.1 the threshold exceedances at 3 consecutive time steps are colored in red. Clusters must fulfill a certain size criterion (equivalent to two 2.5°x2.5° grid boxes or an area of 400 x 400 km^2) and are detected in 6 hourly maximum near surface wind fields. Cluster centers are determined by calculating the average longitude and latitude location, weighted with the cubic exceedance of the 98th percentile at each grid point belonging to the cluster. The resulting cluster centers are finally connected into a wind field track using a nearest neighbor method and any track lasting less than a minimum duration of 24 hours is discarded.

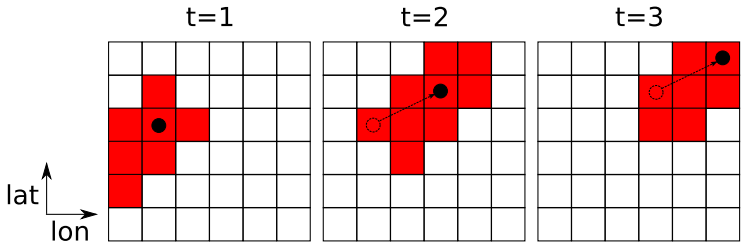

Figure 2.1: Schematic representation of the wind field tracking algorithm. Red areas indicate threshold exceedances in single time steps (wind field clusters). The respective cluster centers (black dots) are connected to the cluster centers of the previous time step (white dots) using a nearest neighbor matching algorithm.

2.2.4 Storm Severity Index

An integrative measure for a storm systems intensity considering it's spatial and temporal extent is the Storm Severity Index (SSI) presented in Leckebusch et al. (2008). The local loss potential of high wind speeds is modeled as the cube of the wind speeds exceedances of the local 98th percentile. The approach is based on studies showing that losses are likely to occur in the 2% windiest situations, thus wind above the 98th percentile. Furthermore, the dependency of losses with the cube of percentile exceedance has been found empirically (Klawa and Ulbrich, 2003). It can be argued, that the cube of wind speeds describes the advection of kinetic energy, giving a physical justification for the term. The storm severity for gridded data calculated for a certain area (Area Storm Severity index, ASSI) can then be formulated in the following way.

$$ASSI(t) = \sum_{x} A(x) \cdot max\left[0, \left(\frac{v(x,t)}{v_{98}(x)} - 1\right)^3\right], \tag{2.1}$$

where summation is performed over all grid cells belonging to a specified area. To calculate the storm severity for a storm system as detected by a wind field tracking algorithm described in the previous section, the event based storm severity index (SSI) is reformulated to

$$SSI = \frac{1}{A_0} \sum_{t} \sum_{\text{x} \in \text{ Affected Area}} A(x) \cdot \left(\frac{v(x,t)}{v_{98}(x)} - 1\right)^3, \tag{2.2}$$

with summation over all time steps that a wind field track exists. For each time step summation is now performed over the affected area (exhibiting wind speed above the local 98th percentile). The weighted sum is in the end normalized onto a reference Area A_0 corresponding to $1000 \cdot 1000 km^2$ (differing to the original formulation presented in Leckebusch et al. (2008)) to ensure the SSI being a dimensionless quantity. The basic local storm severity function for a grid cell x is thus described by the term $(v(x,t)/v_{98}(x) - 1)^3$.

By normalizing on the local 98th percentile for grid cell x an adaptation to the local wind climatology is assumed. In this way, for each grid cell it is ensured, that for the 2% of the highest wind speeds losses are likely to occur. For a specific grid cell affected by a storm system, summation over time results in the local storm severity shown in grey shading in Figure 2.2. At the example of storm "Anatol" in 1999, results of the wind

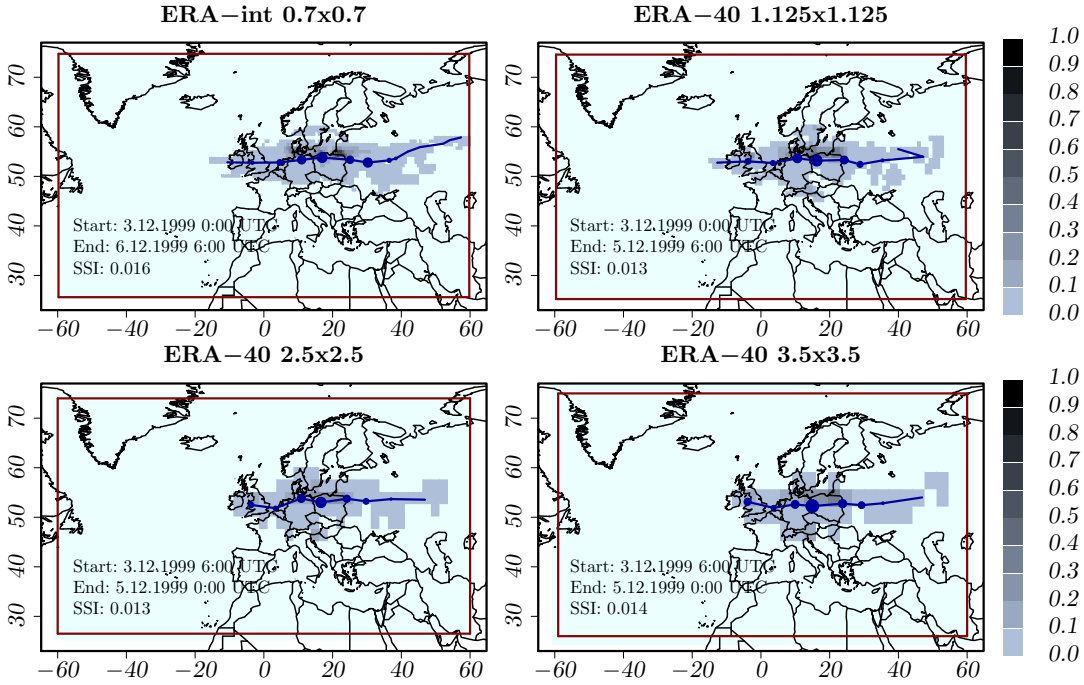

Figure 2.2: Example storm "Anatol". Results of the wind field tracking applied to ERA-Interim (top left, 0.7°x0.7°) and ERA-40 (top right, 1.125°x1.125°). The bottom row shows results applying the tracking algorithm to ERA-40 wind fields interpolated onto a 2.5°x2.5° (bottom-left) and a 3.5°x3.5° grid (bottom-right). Grey shadings represent the local storm severity (dimensionless), the locations of the cluster centers are shown in blue.

field tracking algorithm applied to the different reanalysis data sets is shown in Figure 2.2. Identified tracks slightly differ amongst the different data sets. E.g. the track is identified at an earlier starting as well as a later ending time step in the higher resolved analyses. However, the spatial structure of the footprint, as well as the total SSI values are comparable with a lower SSI in the ERA-40 reanalysis. This holds also, when applying the wind field tracking to the ERA-40 reanalysis data, which has been interpolated onto rather course grids of 2.5°x 2.5°or 3.5°x 3.5°horizontal resolution. Despite losing spatial details in the storm's footprint, the SSI value does not seem to systematically depend on the spatial resolution. This fact is important, since the resolution of the global climate models evaluated here differ (compare Table 2.1).

2.2.5 Extreme Value Analysis

From a statistical point of view, extreme events can be considered as very infrequent observations in a time series. Due to the rareness of such observations, their statistical analysis is particularly challenging. There are multiple applications in which return levels and/or return periods of rare events need to be assessed. One example is in flood management, where the occurrence of rare (and maybe not yet reached) water level heights need to be estimated from past observations to determine the dimensions of flood prevention measures (i.e. dyke heights). Similar questions are often faced in risk management (often accomplished by insurances), where monetary reserves need to be estimated to be able to withstand certain rare events.

Such questions are examples for the necessity of extreme value statistics. From past observations (which may exist only for a rather short period), estimations of return-levels (e.g. the water-level) for rare events having a certain return period (e.g. a flood occurring once every 100 years) shall be made. In many cases such questions require extrapolation, since the extremes in question may not have been observed so far. Extreme value statistics provide a framework in which such extrapolations can be performed. The basic paradigm in extreme value statistics is, that under certain conditions it becomes possible to derive limiting properties (for number of observations $n \to \infty$) from a limited observation data set (with finite number n of observations) Coles (2001) (p. 2). Practically this means, that the aim of extreme value statistics is to estimate the tail distribution function from a limited data set, from which quantiles such as return-levels and return periods can be determined. It can be shown, that asymptotically for large number of observations such tail distributions are limited to three families (I,II,III) of distributions Coles (2001) (p. 46 f.). The type I (Gumbel family) describes an exponentially decaying density function, while type II (Fréchet family) describes a polynomial decay function and type III (reversed Weibull) exhibits a distribution featuring an upper bound. This limitation of tail distributions to only these three possible types is referred to as the extremal types theorem. Furthermore all three families can be combined into a generalized extreme value (GEV) distribution (in other context called Fisher-Tippet distribution) comprising all three families. Besides a location parameter (ν), a scale parameter (σ) the parameter ξ describes the general tail distribution behavior as described above. The GEV distribution for $\xi < 0$ contains the Weibull distribution family, for $\xi = 0$ the Gumbel family and for $\xi > 0$ the Fréchet family. The practical importance of the governing parameter ξ gets obvious when considering the expectation value $E(x) = \int p(x)xdx$ of a variable x featuring the probability density $p(x)$. For a distribution featuring an upper bound ($xi < 0$) the expectation value obviously exists. Also for an exponentially decaying density function ($\xi = 0$) as well as for fast decaying density functions ($xi < 1$) an expectation value can be specified. For shape parameter values $\xi \geq 1$ though, the expectation value degenerates to

infinity. In summary that means for

$$\begin{aligned} \xi < 0 &\quad \text{a finite maximum and finite expectation value,} \\ 0 \leq \xi < 1 &\quad \text{an infinite maximum and finite expectation value,} \\ \xi \geq 1 &\quad \text{an infinite maximum and infinite expectation value.} \end{aligned}$$

As an example one might consider monetary losses occurring due to a certain (natural) hazard. In the first case, the risk bearer is able to eliminate the risk of insolvency by holding a save back larger than the (finite) maximal loss. The second case implies a certain risk of insolvency, nonetheless the risk might be insurable since long-term average losses do not exceed a certain amount. The third category poses an uninsurable risk since the long-term average of losses is expected to be infinite. An important issue when dealing with extreme values is instationarity, meaning for example that processes leading to a certain extreme value distribution change over time. In some cases, stationarity can be assumed even though not strictly given. Especially when dealing with meteorological extremes in a changing climate this is obviously not the case. Even more, since in many cases one is explicitly interested in assessing such changes in the extreme's distribution.

Peak Over Threshold Methods vs. Block Maxima

In classical extreme value analysis, block maxima (e.g. annual maxima) of time series data are analyzed. As an example, a random time series is depicted in Figure 2.3. Considering the annual maxima of this time series resulting in the green marked values. However,

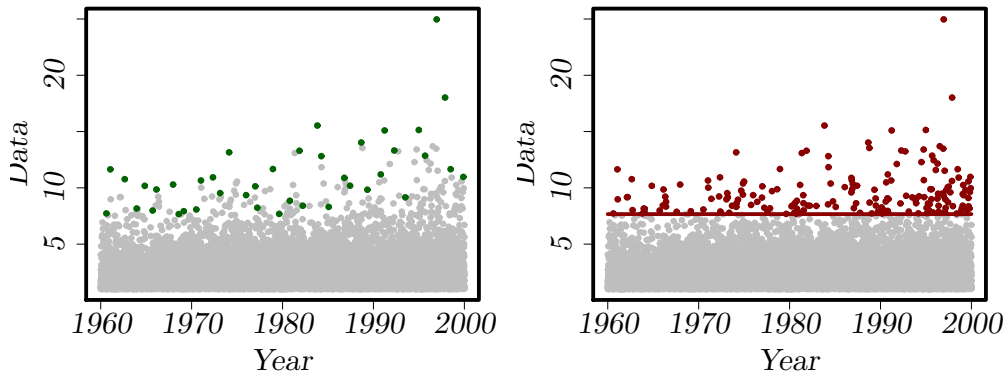

Figure 2.3: Example time series of daily random values, illustrating the block maxima approach with a block length of 1 year (left) and the peak over threshold approach (right).

in this approach many extreme values that may be higher than the annual maximum of

another year are omitted. Another approach to make better use of the available data is to consider all observations laying over a specified threshold. In the example from 2.3, taking into account all values above the maximum value from

Generalized Pareto Distribution

The general Pareto distribution, giving the probability of a value laying above x (under the condition of the value exceeding the threshold u) reads

$$H(x) = Pr\{X > x | X > u\} = \left[1 + \xi\left(\frac{x-u}{\sigma}\right)\right]^{-1/\xi}. \tag{2.3}$$

With the rate of threshold exceedances given by $\zeta_u = Pr\{X > u\}$, it can be written

$$Pr\{X > x\} = \zeta_u \left[1 + \xi\left(\frac{x-u}{\sigma}\right)\right]^{-1/\xi}. \tag{2.4}$$

The two parameters describing the distribution are the scale σ and the shape ξ. By the shape parameter, the different tail characteristics can be distinguished. For $\xi < 0$ the general Pareto distribution becomes an rotated Weibull distribution being bound, for $\xi = 0$ an (unbound) exponentially decaying distribution function and for $\xi > 0$ a Fréchet distribution. Using the general Pareto Distribution, the average return level that occurs once every m observation can then be calculated to be

$$Pr\{X > x_m\} = \frac{1}{m} = \zeta_u \left[1 + \xi\left(\frac{x_m-u}{\sigma}\right)\right]^{-1/\xi}. \tag{2.5}$$

Rearranging leads to

$$x_m = \begin{cases} u + \frac{\sigma}{\xi}\left[(m\zeta_u)^{\xi} - 1\right] & \text{, for } \xi \neq 0 \\ u + \sigma log(m\zeta_u) & \text{, for } \xi = 0. \end{cases} \tag{2.6}$$

Maximum likelihood fitting

For the estimation of the parameters σ and ξ, a maximum likelihood method is used. For that, the likelihood function

$$l(\sigma,\xi) = \begin{cases} -k\log\sigma - (1+1/\xi)\sum_{i=1}^{k}\log(1+\xi(x_i-u)/\sigma) & \text{, for } \xi \neq 0 \\ -k\log\sigma - \sigma^{-1}\sum_{i=1}^{k}(x_i-u) & \text{, for } \xi = 0 \end{cases} \tag{2.7}$$

which is derived from equation 2.3 is minimized with respect to the fit parameters.

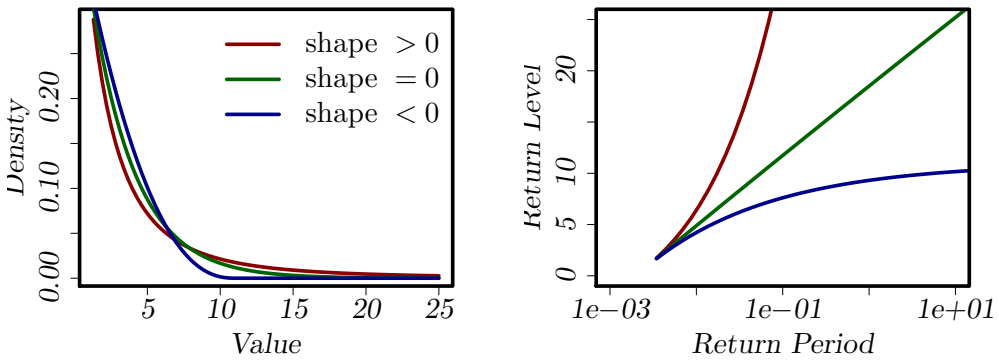

Figure 2.4: Generalized Pareto Distribution depending on the shape parameter ξ. (left) Probability density functions for $\xi > 0$, $\xi = 0$ and $\xi < 0$. (right) Corresponding return level plots.

Threshold Choice

One difficulty when performing extreme value analysis using the GPD model is to find an appropriate threshold u, since u has to be large enough to ensure near-asymptotic behavior (Della-Marta et al., 2008). This can be done by considering the so called mean-residual-life plot. From theoretical considerations (compare (Coles, 2001), p. 78 ff.) it can be derived, that if asymptotic conditions are met the expectation value of exceedances over a threshold u are linearly depending from the chosen threshold. As proposed by Coles 2001, the near-asymptotic behavior can also be identified by the assessment of the dependency of the parameters shape and modified scale on the threshold choice (Coles, 2001) (p. 83 ff.). If asymptotic conditions are met these parameters are expected to be invariant against changes in the chosen threshold. Examples for the assessment of suitable thresholds can amongst others be found in Coles (2001).

Estimation of Confidence Intervals

Confidence intervals for x_m can be derived by the delta method using the variance-covariance matrix resulting from the maximum likelihood fitting procedure.

$$V = \begin{pmatrix} v_{\sigma,\sigma} & v_{\sigma,\xi} \\ v_{\xi,\sigma} & v_{\xi,\xi} \end{pmatrix} \tag{2.8}$$

The confidence intervals for the return levels are then calculated by

$$x_m^{\pm 95} = x_m \pm 1.96\sqrt{Var(x_m)} \tag{2.9}$$

$$\tag{2.10}$$

where $Var(x_m) \approx \nabla_{x_m}^T V \nabla_{x_m}$ and

$$\begin{aligned} \nabla_{x_m}^T &= \left[\frac{\partial x_m}{\partial \sigma}, \frac{\partial x_m}{\partial \xi}\right] = [\xi^{-1}\{(m\zeta_u)^\xi - 1\}, \\ &\quad -\sigma\xi^{-2}\{(m\zeta_u)^\xi - 1\} + \sigma\xi^{-1}(m\zeta_u)^\xi \log(m\zeta_u) \end{aligned} \tag{2.11}$$

Including the uncertainties of ζ_u, which can be approximated to be $Var(\zeta_u) \approx \zeta_u(1-\zeta_u)/n$ into the calculation of confidence intervals, the variance-covariance matrix becomes

$$V = \begin{pmatrix} \zeta_u(1-\zeta_u)/n & 0 & 0 \\ 0 & v_{\sigma,\sigma} & v_{\sigma,\xi} \\ 0 & v_{\xi,\sigma} & v_{\xi,\xi} \end{pmatrix} \tag{2.12}$$

and $\nabla_{x_m}^T$ becomes

$$\begin{aligned} \nabla_{x_m}^T &= \left[\frac{\partial x_m}{\partial \zeta_u}, \frac{\partial x_m}{\partial \sigma}, \frac{\partial x_m}{\partial \xi}\right] = [\sigma m^\xi \zeta^{\xi-1}, \xi^{-1}\{(m\zeta_u)^\xi - 1\}, \\ &\quad -\sigma\xi^{-2}\{(m\zeta_u)^\xi - 1\} + \sigma\xi^{-1}(m\zeta_u)^\xi \log(m\zeta_u)] \end{aligned} \tag{2.13}$$

As suggested in Coles (2001), better estimation of the confidence intervals is achieved by analysis of the profile likelihood. For return levels, a re-parameterization is done by rearranging Equation 2.6

$$\sigma = \begin{cases} \frac{(x_m - u)\xi}{(m\zeta_u)^\xi - 1} & \text{, for } \xi \neq 0 \\ \frac{x_m - u}{\log(m\zeta_u)} & \text{, for } \xi = 0. \end{cases} \tag{2.14}$$

This function is substituted into 2.7, which can be maximized with respect to ξ. The resulting equation, as a function of x_m, gives the profile log-likelihood function for the m-observation return level. At the same time, as a function of the return period $(m\zeta_u)$, it gives the profile likelihood to estimate the confidence intervals for the return period of a fixed return value x_m.

2.3 Recent and Future Winter Storm Frequency

At first, the European winter storm climatology and possible changes shall be assessed in terms of winter storm frequencies, i.e. the number of winter storms affecting a certain area per year. For that, the wind field tracking algorithm (Section 2.2.3) is applied to both reanalysis data sets ERA-Interim and ERA-40 as well as to the global climate model simulations as described in Sections 2.2.1 and 2.2.2. For a specific location, the frequency of winter storms is then assessed by identifying all tracks passing by in a circle of 500 km radius around the location. This size of the radius is chosen, since large scale cyclonic systems have a typical scale of extent of 1000 km. Thus a track (with its center) passing closer than 500 km might possibly affect the site under consideration. The number of tracks per year is then evaluated on a regular 2°grid for the region -60°E to 60°E and 25°N to 75°N and shall be called track density in the following. Resulting track density

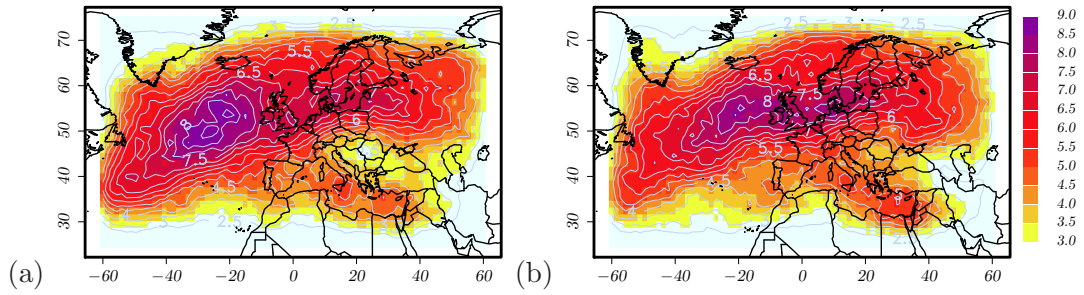

Figure 2.5: Track density in units of tracks per year for (a) ERA-Interim with a resolution of 0.7°x0.7° and (b) ERA-40 with a resolution of 1.125°x1.125° for the winter months October through March of 1979-2001.

calculated for the reanalysis data sets ERA-Interim and ERA-40 are shown in Figure 2.5 (a) and (b). For ERA-Interim (evaluated for the period 1979-2001), a pronounced maximum in the track density is found in the Northern Atlantic, where values of up to 8.5 tracks per year are identified. A path of main wind storm activity is found across the Northern Atlantic, the British Isles and reaching till Western Russia. Furthermore, the track density features a lower secondary maximum over the Mediterranean with values reaching up to 5 tracks per year. Track density derived from ERA-40 reanalysis with a lower horizontal resolution of 1.125°are well comparable to these results and feature a similar spatial structure. Also the absolute number of identified tracks per year are well comparable, however the maximum frequencies across the main path of storm activity over the Northern Atlantic is less pronounced. Maximum storm frequencies derived from ERA-40 account for about 8 tracks per year west of the British Isles which is considerably lower compared to the results from ERA-Interim. Furthermore, the areas of highest storm

activity is found to extend further towards the east in ERA-40 with track density reaching 8 events per year over northern parts of Germany and Denmark.

It can be assumed, that the differences in the horizontal resolution of the two data sets influence the results obtained for the winter storm frequencies. E.g. the model's representations of orographic elevation might well influence in how far storm systems, reaching European land, dissipate their energy. In a lower resolved orography in ERA-40 compared to ERA-Interim, this might for example lead to an enhanced track density over northern Europe as diagnosed. To exclude the possibility, that these effects are caused by the differing resolution of the wind data used in the tracking algorithm (thus being artefacts of the tracking procedure rather than physical model differences), the wind field tracking is applied additionally to ERA-40 winds which are interpolated onto a regular grid with grid spacing of 2.5°x2.5° as well as a grid spacing of 3.5°x3.5° (compare Figure 2.2 in Section 2.2.4). Resulting track density evaluated for the full period of data availability (1958-2001, Figure A.1 (c) and (d) of Appendix A) are found to differ only insignificantly to results achieved with data in the original resolution of ERA-40. Similar

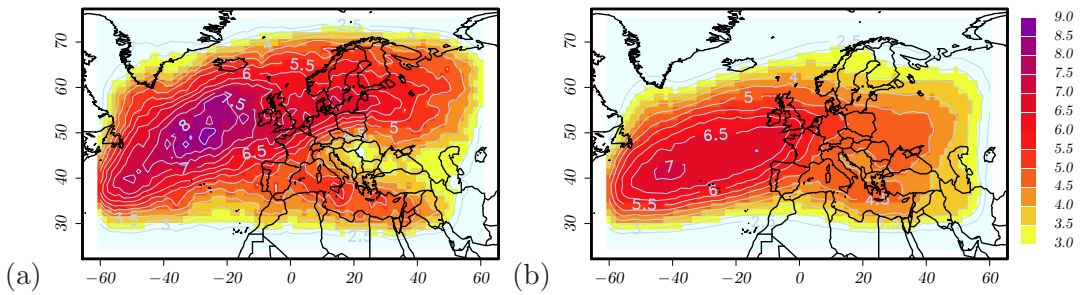

Figure 2.6: Track density in units of tracks per year derived from (a) ERA-Interim for October-March of 1979-2010 and (b) the multi-model (ensemble mean) for October-March of 1971-2000 under recent climate conditions.

the wind field tracking is applied to the output of the 8 global climate model simulation as described in Section 2.2.2. For recent climate conditions (20C) track density are evaluated for the period 1971-2000 and averaged to gain the ensemble mean track density as shown in Figure 2.6 (b). Comparison to track density from ERA-Interim (Figure 2.6, a) shows that the general spatial structure is comparable, however the maximum in the Northern Atlantic is less pronounced, reaching up to 7 tracks per year. Moreover the main path of storm activity is shifted southward and is more zonally orientated. Thus especially in the Baltic and Scandinavian regions track density are considerably lower. Over the whole investigation area, the number of events identified per winter half year is considerably underestimated by the GCMs with 54 events p.a. (ensemble mean) comparing to 61 events p.a. in ERA-Interim and 64 events p.a. in ERA-40, however with considerable

spread amongst the individual model simulations ranging from 48 (BCCR-BCM2) to 66 (DMI-ECHAM5). At the same time, the mean duration of identified storm events can be assessed in both reanalysis and model simulations. Exemplary, the tracks passing by the location [10°E, 51°N] have a mean duration of 13.2 time steps in ERA-Interim, corresponding to a mean lifetime of about 72 hours. Averaging over all 8 models, the mean lifetime in the 20C model simulations is only 12.1 time steps corresponding to about 66 hour mean lifetime of events. This lower lifetime of wind field tracks might indicate that storm systems, in comparison to reanalysis, dissipate at an earlier stage (or do not find suitable conditions for further intensification) and thus do not reach as far east.

Changes in the occurrence frequency of winter storms are assessed by calculating the track density for the model projections under SRES-A1B scenario conditions. Ensemble mean track density for 3 future periods 2011-2041, 2041-2070 and 2071-2100 are shown in Figure 2.7 (a)-(c) respectively and changes compared to the reference period 1971-2000 shown in Figure 2.7 (d)-(f). It can be found, that the spatial distribution undergoes distinct changes, namely a (gradual) focusing or narrowing of the main track of winter storm activity with decreasing track density north and south of this path and increasing track density on this path. Most pronounced, this increase can be seen in the southwest of the British Isles, where track density increase by around 1 track per year towards the end of the 21st century from 6.5 to 7.5 tracks per year. Besides this focusing, a distinct increase of track density is found at the East end of the main path of storm activity. This indicates, that the winter storm systems seem to travel further East over European inland. For areas in Western Russia this leads to an increase of storm activity from 4.5 to 5.5 tracks per year. In Figure 2.7 (d)-(f), green (dark green) contours indicate the regions where an agreement on the increase (decrease) between the individual model projections exists. Thin lines indicate regions where at least 6 of the 8 model simulations, thick lines indicate regions where all model simulations agree on the detected increase/decrease. Considerable (6 out of 8) agreement is found for the last future period (2071-2100) in the increase of track density over central Europe covering the British isles, Northern Germany and the Baltic region, while for only a small regions all models agree on an increase. 6 out of 8 models show a decrease in track density over the North-Western Atlantic, while all models agree on a decrease of track density south of the main path of storm activity and over the Mediterranean.

Over the whole domain, a decrease in winter storm events identified by means of the tracking algorithm is identified towards the end of the 21st century. Averaging over the 8 model simulations the number of events identified per winter season decreases from 48.5 p.a. in 20C to 45.6 p.a in the period 2071-2100 of SRES-A1B with 6 out of the 8 model simulations showing a decrease. At the same time, mean duration of identified events, evaluated for the location [10°E, 51°N], increases from 12.1 time steps to 12.3 time steps

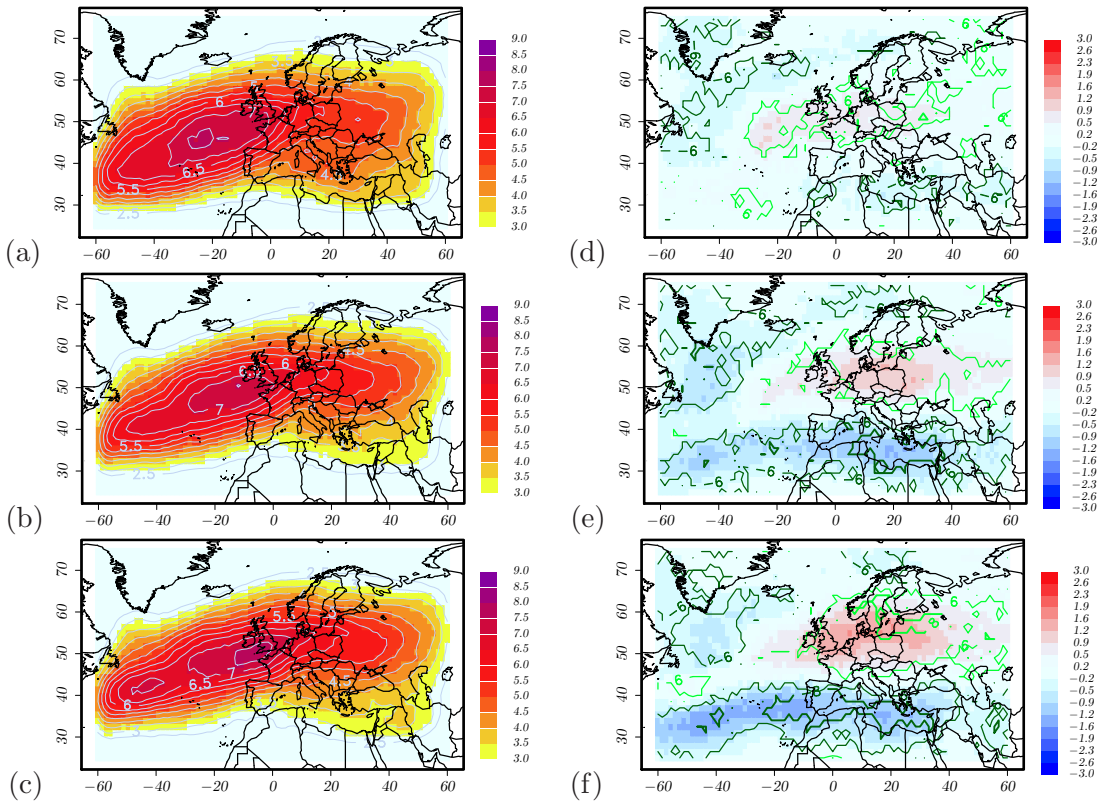

Figure 2.7: Ensemble mean of the track density in units of tracks per year, derived from the multi-model ensemble for the periods (a) 2011-2040 (b) 2041-2070 (c) 2071-2100 under SRES-A1B conditions. (d)-(f) show the respective differences in track density compared to the reference period 1971-2000. Thin contours in light-green (dark-green) indicate areas in which 6 out of 8 models project an increase (decrease) in track density, thick contours indicate areas in which all models project an increase (decrease).

corresponding to an average increase in mean lifetime of about 1 hour.

In the following, different sources of uncertainties shall be assessed and quantified. At first, the statistical uncertainties are quantified which result from a limited sample of 30 years that are analyzed for a single model simulation. Furthermore, the uncertainties resulting from unknown future GHG emissions shall be assessed by analyzing 3 different future scenarios (SRES-A1B, SRES-A2 and SRES-B1). Of course these 3 scenarios do not at all represent all possible emission pathways, which is why this analysis is to be interpreted as a sensitivity analysis rather than an estimation of uncertainties themselves. At last, modeling uncertainties are assessed by analyzing climate change signals from different model simulations (using different model formulations). Again, the set of models evaluated do not represent the full set of possible model implementations. Since many assumptions enter in different physical parameterization schemes, such a full set of model simulations is impossible to generate with current computing power.

2.3.1 Statistical Uncertainty and Natural Variability

Considering changes in climatological mean quantities as done in the previous section, questions about whether identified change signals pose (statistically) significant as well as relevant changes with respect to recent climate conditions. Statistical uncertainty in the case of track density (which is calculated by basically counting the number N of winter storm events) assuming a Poisson process can be simply calculated by $\Delta_N = \sqrt{N}$. Considering the number of tracks per year $X = N/t$ this becomes $\Delta_X = \sqrt{N}/t$. For ERA-Interim, statistical uncertainty on the derived track density is shown in Figure 2.8 (a). Since scaling with track density to the power of 0.5, areas of highest statistical uncertainty correspond to areas of highest track density, with values reaching up to 0.6 tracks per year. For the areas of strongest change signals in track density, namely central and northern Europe, values range between 0.4 to 0.5 tracks per year. Comparing future- to recent-track density as derived from the individual model simulations including the respective statistical uncertainties (compare Section 2.3.3) it is found that for most of the model simulations significant patterns of track density changes are derived. By considering the ensemble mean of 8 model simulations thus enlarging the data sample from 30 to 240 years for each period statistical uncertainties (scaling with $1/sqrt(t)$) are considerably reduced by a factor of about $\sqrt{(}30)/\sqrt{(}240) \sim 1/3$. Correspondingly, changes in track density shown in Figure 2.7 (d)-(f) are found to be highly statistically significant with insignificant changes not being shown. Changes in mean track density might be found

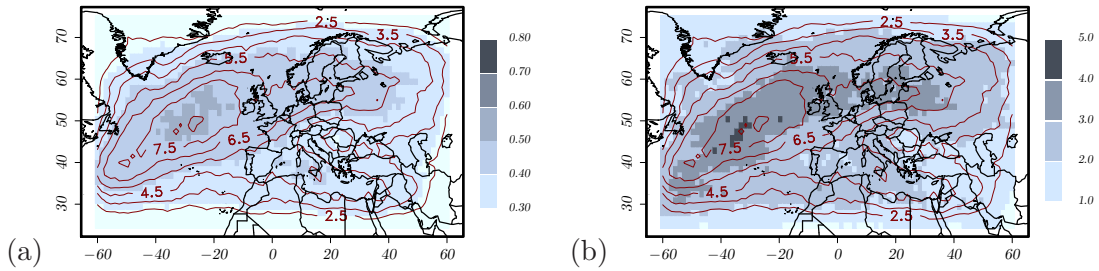

Figure 2.8: (a) Statistical uncertainty (Δ_X) on the track density and (b) inter annual variability of track density based on the results from ERA-Interim. Red contours show the mean track density derived from ERA-Interim over the period 1979-2010.

to be statistically significant, however not being of relevance in terms of (inter annual) variability under recent climate conditions. Inter annual variability, calculated by means of one standard deviation σ of yearly track density are shown in Figure 2.8 (b) for ERA-Interim. Highest variability is found in the areas of highest track density (shown as red contour lines) with σ reaching up to 5 tracks per year over the Northern Atlantic. Over Europe, values range between 2 tracks per year in Southern regions and 4 tracks

per year over the North-Sea and the Baltic region. Track density in these regions were found to increase by about 1 track per year thus corresponding to an increase of about 0.25σ. Similarly the track density is found to decrease by about 1 track per year over the Mediterranean, corresponding to a decrease by roughly 0.5σ. Diagnosed changes in winter storm frequencies are thus found to be considerable as well as statistically significant, distinctly exceeding changes due to recent climate natural variability.

2.3.2 Scenario Uncertainty

The most obvious uncertainty when considering future climate conditions (and thus on the implications for the European winter storm climate) lies in the unknown socioeconomic development and related emissions of greenhouse gases (GHG) such as C02. Since these future developments are (nearly) unpredictable, different scenarios have been developed by the Intergovernmental Panel on Climate Change (IPCC) which have been presented in the Special Report on Emission Scenarios (SRES) (Nakicenovic et al., 2000). Each scenario presents one of many possible pathways of future development including assumptions of society, world population and economic growth. Instead of focusing on one such scenario, the consideration of multiple pathways offers the possibility to assess the possible range of climate change signals resulting from the uncertainty about future emission and thus GHG concentrations. Thus in this section, the dependence of the changes detected in the previous section on the considered scenario shall be investigated. We chose to investigate the Scenarios SRES-A1B, SRES-B1 as well as SRES-A2. Belonging to the A1 scenario family (which describes a rapid economic growth development, a global population that peaks in mid-century, the rapid introduction of new and more efficient technologies) the SRES-A1B scenario assumes a balanced use of fossil and non-fossil energy sources in the future (Nakicenovic et al., 2000). The SRES-A2 scenario describes a heterogeneous development including localized development of economy, with a continuous increase in world population and a slow introduction of new technologies. Different to this, the SRES-B1 scenario considers a homogenous development of economic structures leading to reductions in material intensity and the introduction of clean and resource-efficient technologies, while world population is assumed similar to the one in SRES-A1B. Of course, these 3 considered scenarios do not represent in any way a complete set of possibilities on future development of GHG concentrations. However they should be used to assess the sensitivity of the derived climate signals, keeping in mind that the full range of possibilities might result in considerably larger spread. For MPI-ECHAM5, 3 simulation runs are analyzed for each of the 3 scenarios. Derived change signals in the track density for the period 2071-2100 are shown in Figure 2.9 (a)-(c) for the SRES-A1B, SRES-B1 and the SRES-A2 scenario respectively. The spatial structure of derived signals are found to be very similar, with an increase in track density across the main path of storm activity,

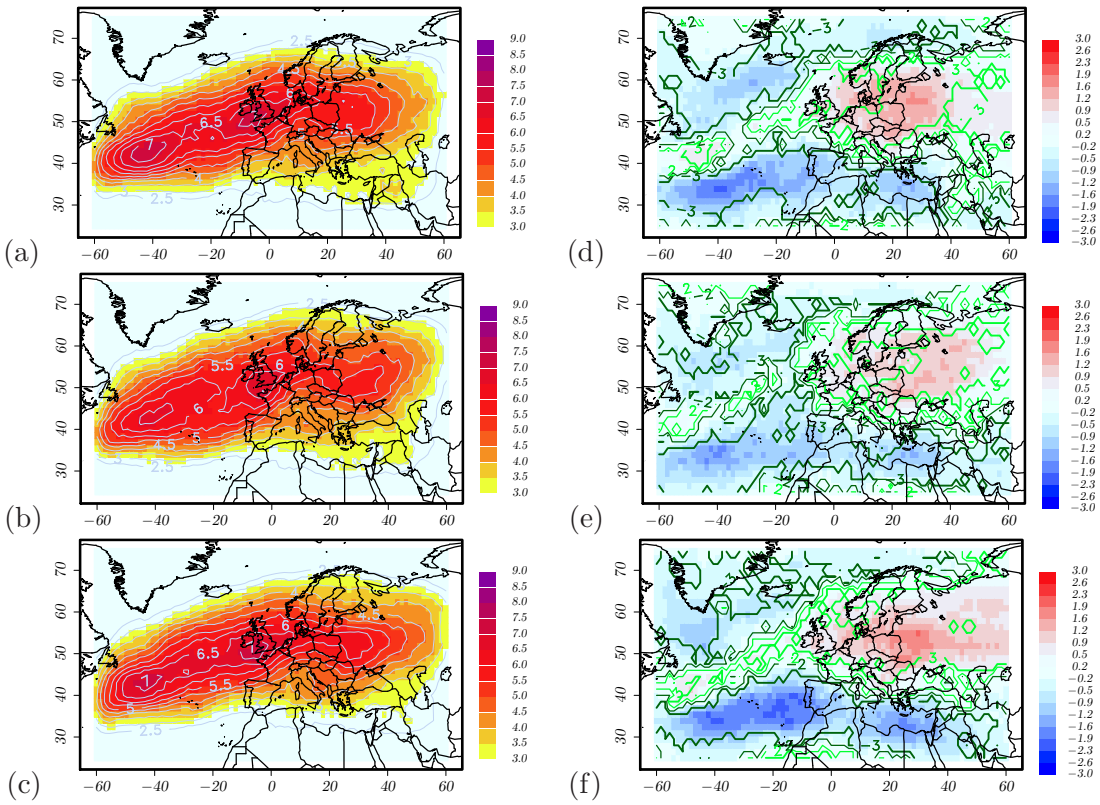

Figure 2.9: Ensemble mean track density in units of tracks per year, derived from the MPI-ECHAM5 ensemble under (a) SRES-A1B, (b) SRES-B1 and (c) SRES-A2 conditions for the period 2071-2100. The respective changes in the track density compared to the reference period 1971-2000 are shown in (d)-(f). Thin contours in light-green (dark-green) indicate areas in which 2 out of 3 runs project an increase (decrease) in track density, thick contours indicate areas in which all 3 runs project an increase (decrease).

especially around the British isles, Northern Germany, the Baltic region as well as the Western part of Russia. Furthermore a decrease in track density is found North and South of these regions. Furthermore, the strength of this signal is found to be dependent on the considered scenario. For SRES-B1, the weakest signal is found, while for SRES-A1B and SRES-A2 the signals are found to be rather similar in strength. Even though an ensemble of three model simulations has been analyzed, with internal variability in each projection being independent, the signal strength is regionally subjected to considerable variations due to (multi-) decadal variabilities which may not cancel out fully using such small set of projections. Thus on local scales it may be difficult to judge for which of the scenario signals are strongest.

2.3.3 Model Uncertainty

Considering the track density derived from individual model simulations for recent climate conditions reveals high inter model differences (Figure 2.10, left column), which distinctly exceed random variations explained by internal climate variability within an individual simulation. For example in the IPSL-CM4 model simulation, featuring very high track density reaching above 10 tracks per year over the Northern Atlantic, nearly twice as many storm systems are identified compared to the BCCR-BCM2 model simulation. Track density variability diagnosed in the corresponding long term reference simulations (1861-2000) can be found to be much smaller and can thus not account for these large differences. Instead, these differences reveal the different underlying model formulations, including differing parameterizations or simplifications, necessary since many physical processes can't be explicitly be resolved in state of the art GCMs due to limitations in computing capacities. Even though the methodology to identify and characterize the intensity of storm systems was found to be largely independent of the model resolution (compare Section 2.2.4), differing model resolution can additionally affect the representation of physical processes on regional scales e.g. through a different representation of the underlying model topography. Different model formulations and model resolution can thus generate large biases in local gust climatology produced by the individual model, strongly influencing the derived track density. The analysis of the MPI-ECHAM5 ensemble, consisting of three independent model simulations which should not feature any systematic biases, reveals that natural variability can however account for a considerable additional spread in the track density of individual model simulations. Despite the

Model-Scenario	1971-2000	2071-2100	Relative Change
ERA-Interim	$5.69 \pm 0.42^{*}$	-	-
MPI-ECHAM5 (1)	4.40 ± 0.38	5.73 ± 0.43	+30.3 %
MPI-ECHAM5 (2)	4.47 ± 0.39	5.47 ± 0.43	+22.39 %
MPI-ECHAM5 (3)	4.63 ± 0.39	5.07 ± 0.41	+9.35 %
FUB-EGMAM	4.90 ± 0.40	7.03 ± 0.48	**+43.54** %
BCCR-BCM2	4.50 ± 0.39	5.96 ± 0.45	+32.54 %
CNRM-CM3	6.30 ± 0.46	8.20 ± 0.52	+30.16 %
DMI-ECHAM5	5.37 ± 0.42	6.70 ± 0.47	+24.84 %
IPSL-CM4	6.77 ± 0.48	6.00 ± 0.45	**-11.33** %
ENSEMBLE	5.17 ± 0.15	6.27 ± 0.16	+21.37 %

*Table 2.2: Track density in units of tracks per year for the location [10° E, 51° N] for the individual model projections under recent climate conditions (1971-2000) and SRES-A1B scenario conditions (2071-2100). * for ERA-Interim the reference period is 1979-2010 instead of 1971-2000.*

large inter model spread, all models can be found to reproduce the main band of winter storm activity over the Northern Atlantic, consistent to the results from reanalysis data. However with respect to absolute values of track density as well as the location of typical storm paths, biases and internal climate variations result in considerable model differences which need to be kept in mind when interpreting projected changes in winter storm frequencies. Resulting changes in the track density, derived from the 8 individual projections of the multi model ensemble are shown in Figure 2.10. Consistent to the large inter model spread diagnosed for the track density under recent climate conditions, large differences in derived changes in track density are revealed. For example, changes in track density around the British Isles ranging from a slight decrease of -0.5 to -1 tracks per year diagnosed from IPSL-CM4 (h) to strong increases of more than +3 tracks per year projected by the CNRM-CM3 (e) model. Similarly, the decrease of track density in the Southern parts of the North Atlantic exhibits a large ensemble spread ranging from values close to zero up to a decrease of 2.5 tracks per year. However, all models share the common feature of projecting an increase in the number of storm systems in regions across the main path of winter storm activity, described in Section 2.3. Aloof this path, decreases in the track density are diagnosed for all model projections. The strength of the individual parts of these patterns are however strongly depending on the considered model simulation. E.g. for the IPSL-CM4, the pattern is dominated by the decrease which is found over nearly the entire North Atlantic, while small increases in track density are found further east, compared to the other simulations of the multi-model ensemble. In contrast, for the CNRM-CM3 simulations the increases in track density along the typical storm paths dominate the diagnosed change pattern, while the decreases around Iceland and around the Azores are rather small. For the grid point representative for Germany [10°E and 51°N], resulting track density and their changes according to the SRES-A1B scenario are listed in Table 2.2, with changes ranging between −11% (IPSL-CM4) and +44% (FUB-EGMAM). However, only one projection (IPSL-CM4) features a decrease in the track density for this grid point with an increase by about 21% being diagnosed in average over the ensemble.

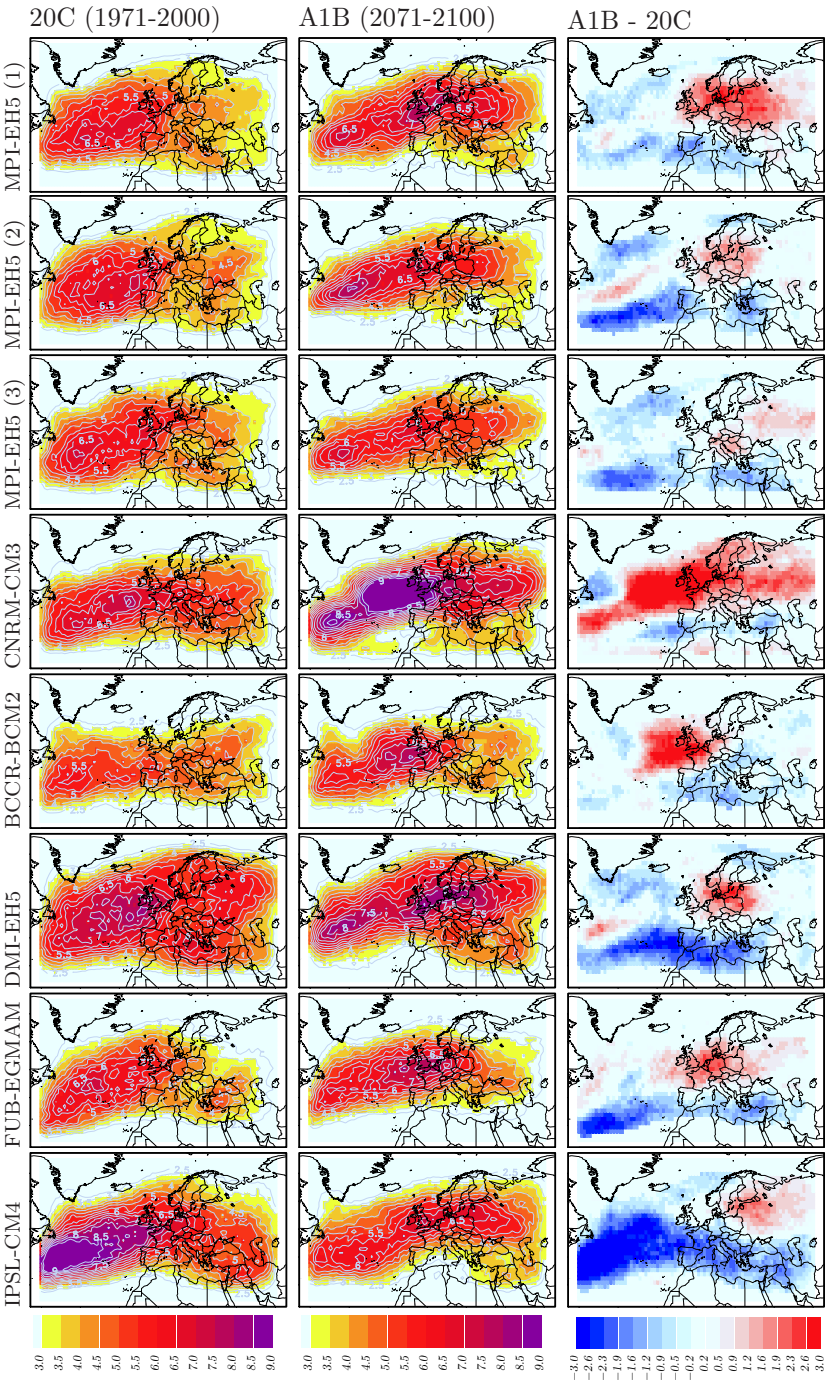

Figure 2.10: Track density in units of tracks per year, derived from the individual GCMs. (left column) Individual model's track density for the period 1971-2000 under recent climate conditions. (middle column) Same for the period 2071-2100 under SRES-A1B conditions and (right column) significant differences compared to 1971-2000.

2.4 Intensities of Recent and Future Winter Storms

In the previous section the track density (i.e. frequency) of winter storm events, identified by means of an objective wind-field tracking algorithm, were analyzed finding fundamental changes in the spatial distribution of the track density over the North-Atlantic and Europe under changed climate conditions. Given these changes in storm frequencies it can well be assumed that the entire frequency-intensity distribution of storm events is significantly modified under altered climate conditions, which may strongly affect the occurrence of extreme winter storm events. Thus in this section such changes in the frequency-intensity distribution shall be assessed by means of extreme value analysis (Section 2.2.5) to derive possible changes in return levels and return periods of rare winter storm events. Similar

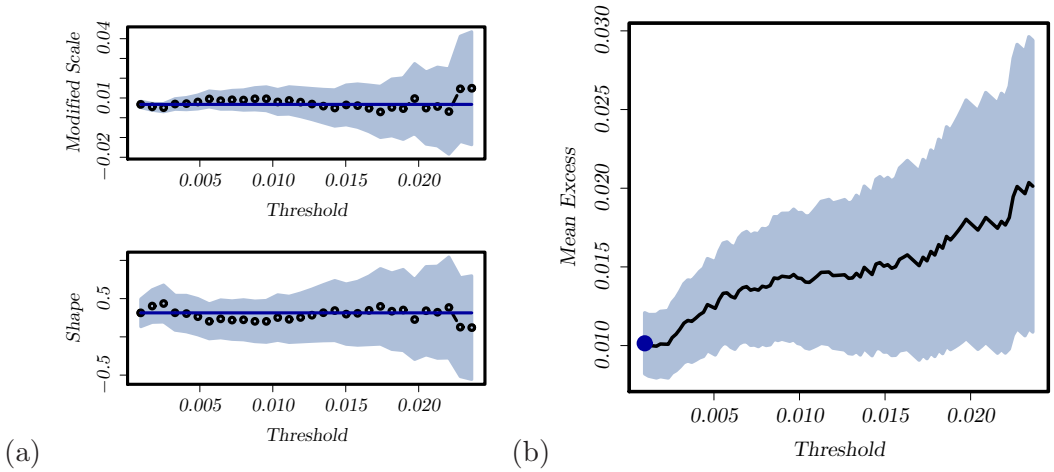

Figure 2.11: Validation of the threshold choice for the GPD fit to SSI values from ERA-Interim (1979-2010). (a) Stability of fit parameters. (b) Mean residual life plot.

to the approach chosen for the calculation of track density, for a specific location all tracks are considered passing a circle of 500 km radius around this location. For the selected set of storm events, the Storm Severity Index (see Section 2.2.4) is analyzed by means of peak over threshold analysis. As described in Section 2.2.5, for this approach at first a suitable threshold needs to be defined which can be done by considering the GPD (Generalized Pareto Distribution) parameter stability or the so called MRL (Mean Residual Life) plot. Considering all events identified from ERA-Interim (1979-2010) around the location [10°E, 51°N] representing the center of Germany, the parameter stability plots (left) as well as the MRL-plot (right) are shown in Figure 2.11. As explained in Section 2.2.5, the optimal threshold is to be chosen as the smallest one, for which stability of parameters is given for increasing thresholds. Resulting parameter stability plots show, that actually there is

no objection against choosing the lowest possible threshold, namely taking all detected events into account. Also considering the MRL-plot in Figure 2.11 (b) confirms the suitability of this threshold choice, since a linear increase of Mean Excess with increasing threshold can reasonably assumed, especially when taking into account the rather large confidence intervals (grey shaded areas). The finding, that all events may be included in the GPD analysis states that the thresholds used within the wind-field tracking procedure (namely detecting exceedances of local 98th percentile with a minimum area and minimum lifetime requirement) are in fact sufficient to ensure the near-asymptotic behavior of the SSI distribution. For ERA-Interim, the resulting return level plot using the minimum

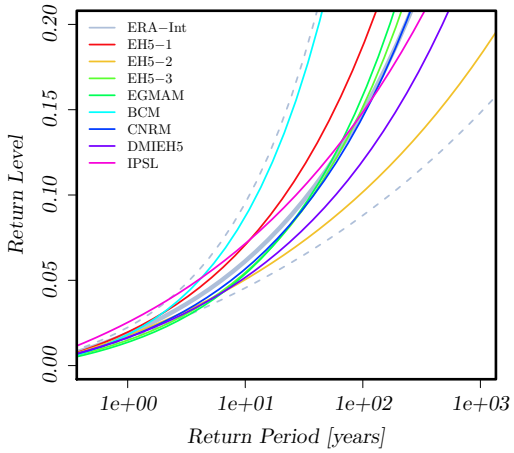

Figure 2.12: Return level plot for SSI values of wind-field tracks affecting the location representing the center of Germany [10° E, 51° N]

of all considered SSI values as a threshold is shown in Figure 2.12 in grey with 95% confidence intervals as dashed lines. By means of the GPD analysis, the example storm "Anatol" (compare Figure 2.2) for which an SSI value of 0.016 has been calculated can now be assigned with a return period of 0.8 years. Similarly return periods can be assigned to other prominent winter storm events, such as Kyrill for which a return period of 2.2 years is calculated and Vivian-Wiebke with a return period of 14 years. Considering a larger set of historical storm events that produced large damages in Germany (e.g. as listed in Table 2 of Donat et al. (2011b)) most events can be found within the list of wind-field tracks identified from ERA-Interim. However, the height of damages they produced is not necessarily reflected by the return period that can be calculated here since the full SSI (which may for include large areas of threshold exceedances over sea and thus not fully affecting Germany) is taken into account. The actual modeling of winter storm damages and a re-assessment of the storm's return periods with respect to

their damages will however be described in detail in Section 4.7. Peak over threshold

Model-Scenario	1 year return level	10 year return level	100 year return level
ERA-Interim	0.019 [0.016 0.022]	0.061 [0.039 0.083]	0.15 [0.05 0.25]
MPI-ECHAM5 (1)	0.020 [0.016 0.023]	0.071 [0.039 0.103]	0.19 [0.03 0.35]
MPI-ECHAM5 (2)	0.018 [0.015 0.021]	**0.050** [0.033 0.068]	**0.10** [0.03 0.17]
MPI-ECHAM5 (3)	0.015 [0.012 0.018]	0.055 [0.032 0.077]	0.15 [0.04 0.27]
FUB-EGMAM	**0.014** [0.011 0.016]	0.054 [0.030 0.078]	0.16 [0.03 0.29]
BCCR-BCM2	0.018 [0.014 0.022]	**0.087** [0.038 0.137]	**0.32** [0.02 0.67]
CNRM-CM3	0.016 [0.014 0.019]	0.057 [0.033 0.081]	0.15 [0.03 0.26]
DMI-ECHAM5	0.016 [0.014 0.019]	0.052 [0.033 0.070]	0.12 [0.04 0.20]
IPSL-CM4	**0.025** [0.021 0.029]	0.072 [0.048 0.095]	0.15 [0.06 0.24]
ENSEMBLE	0.018 [0.017 0.019]	0.062 [0.053 0.071]	0.16 [0.12 0.20]

Table 2.3: Resulting SSI return levels (dimensionless) from GPD analysis for SSI values of tracks passing a 500 km circle around the location [10° E and 51° N].

analysis can similarly be performed on the basis of SSI values for events identified from the individual GCM simulations as described in Section 2.2.2. Resulting return level plots for the respective 20C climate conditions (1971-2000) are shown in Figure 2.12 as colored lines and for return periods of 1, 10 and 100 years derived return levels are specified in Table 2.3. Given the rather large statistical uncertainties especially for high return values (indicated as dashed lines for the GPD-fit of ERA-Interim), there is a well agreement of the model simulations compared to ERA-Interim. However the ensemble reveals a considerable model spread resulting in differences in the fitted distributions. For an event with a return period of 1 year, this inter model spread spans a range from 0.014 to 0.025 comparing to a 1 year return level of 0.019 diagnosed from ERA-Interim. It can be noted, that this inter model spread is comparable to the statistical uncertainties derived (using the profile likelihood method) for the return period from ERA-Interim. Finally, the SSI values from the individual model simulations can be pooled together, to derive a GPD fit on an enlarged data base reducing the statistical uncertainties considerably. Resulting 1 year return level from GPD analysis gives 0.018 with a confidence interval of [0.017 0.019], which compares very well to the result from ERA-Interim. Having demonstrated the methodology for a single location, the analysis can be expanded to a grid ranging from -60°E to 60°E and 25°N to 75°N with regular grid spacing of 2.5°. For each grid point the analysis described analysis is carried through to derive the specific return periods and return levels. Resulting 1 year return levels are shown in Figure 2.13 as derived from ERA-Interim (a) and ERA-40 (b). Maximum return levels are found in the Northern Atlantic with values ranging up to 0.025 with a spatial distribution rather similar to the derived

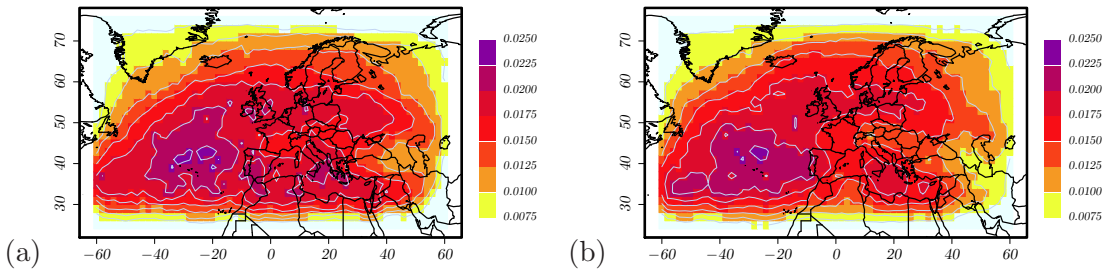

Figure 2.13: SSI return level (dimensionless) of storm systems occurring once a year, derived from (a) ERA-Interim 1979-2010 and (b) ERA-40 1958-2001.

track density (see Figure 2.6 (a)). However the highest return values are found about 10 degrees southward compared to the location of highest track density. Furthermore, besides a large area of high return levels over the Northern Atlantic, a band of high return values is found across the British Isles and Germany reaching as far as Western Russia. Also high return values are found in the Mediterranean area (similar to the findings for the track density), which in some areas even exceed the values found on the northern storm track. In comparison the results derived from both reanalysis data sets are in good agreement. Especially over the North Atlantic, both absolute values as well as the spatial distribution of return levels are comparable. Towards the east of the considered region however, results from ERA-40 show slightly lower return values over both the Mediterranean as well as the northern band of storm activity. It needs to be noted however, that the period of investigation differs amongst ERA-Interim and ERA-40. On the one hand, due to long term variability involved this might alter the respective return values. Also due to the rather short investigation period of 32 years in case of ERA-Interim this leads to higher statistical uncertainties in the derived return values. This also reflects in the fact that for ERA-Interim, the spatial field of return level is less smooth in comparison to the field for ERA-40.

Deriving return values from the multi model ensemble (by pooling the available model simulations to a total sample of $8x30 = 240$ years) as shown in Figure 2.14 (a) reveals a rather similar spatial distribution. The resulting field is much smoother which is due to the larger statistical data sample. The general picture found for ERA-Interim is confirmed with high return levels found over the Northern Atlantic. However the area of maximum of return levels over the North Atlantic is found to be more localized and is oriented more as a zonal band of high return values with higher absolute values compared to the reanalysis data. This is similar to the findings with respect to the track density (compare Section 2.3), with highest return values being found about 5° southward of the band of highest track density. Again high return levels are found on the path across the Mediterranean with values considerably higher than identified from reanalysis. The northern band of high

return values identified in reanalysis however is rather poorly resolved and becomes only visible on a narrow band extending over the British Isles reaching the North Sea. This has been similarly diagnosed in terms of track density (compare Figure 2.6) with considerably lower track density, especially towards the east of the northern branch of storm activity, in particular over the Northern and Baltic Sea. Analyzing the multi model ensemble

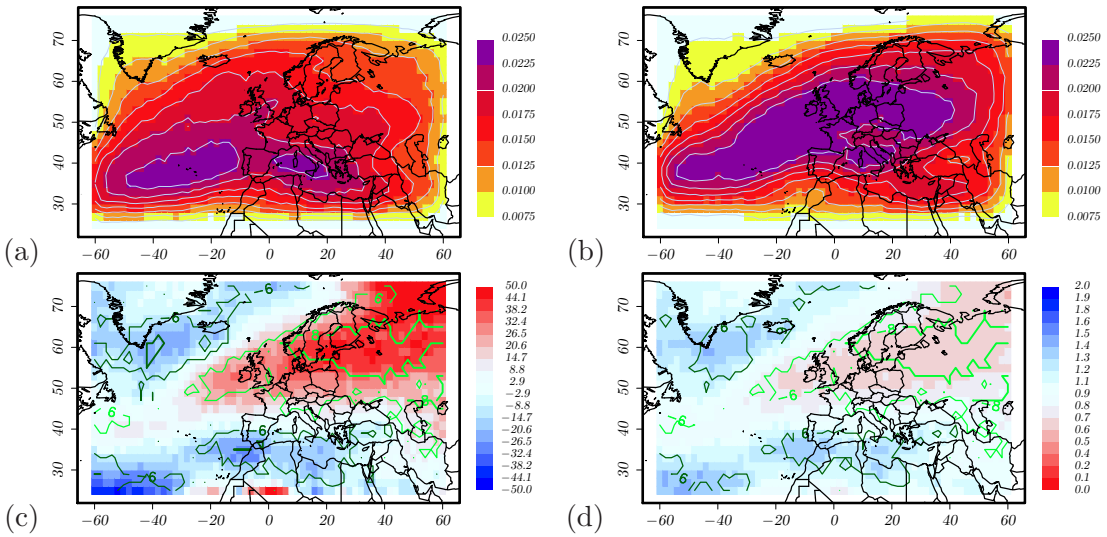

Figure 2.14: SSI return levels (dimensionless) of storm systems occurring once a year, derived from the pooled multi-model ensemble for (a) the period 1971-2000 and (b) the period 2071-2100 under SRES-A1B conditions. (c) Relative increases in return levels for 2071-2100 compared to 1971-2000. (d) Return period (in years) for 2071-2100 of storms occurring once a year under recent climate conditions.

for SRES-A1B conditions in the period 2071-2100, again pooling together the 8 model simulations, return levels can be similarly assessed for the future period (as shown in 2.14 (b)). Similar to the findings regarding track density fundamental changes in spatial pattern of the 1 year return levels can be identified. The areas of highest return levels, identified over the Northern Atlantic in 20C, extends much further eastwards stretching far over the central European continent for SRES-A1B conditions. Also a general northward shift of the area with highest return values over the North-Atlantic by a few degree can be diagnosed. Relative changes $(100\% \cdot (A1B - 20C)/20C)$ are shown in Figure 2.14 (c). In this representation, the northward shift over the Northern Atlantic can be identified as an area of decreasing return values (by about 20% to 30%) south of approximately 30°, while a slight increase in return levels of up to 10% is identified further North. Further north, starting at approximately 50°, decreases in return levels of about 15% to 20% are identified. The general picture detected in terms of track density with a focusing of the main storm paths on a narrow path across the Northern Atlantic can thus be confirmed

in terms of intensities of severe storm events. Most pronounced changes however feature strong increases in return levels over the British Isles, the Northern Sea, Scandinavia and large areas stretching towards the eastern border of the investigated region. These changes range up to 50% with maximum increases identified over the Baltic region and the Barents Sea. While over the Northern Atlantic the channelization effect on a main storm path is characterized mostly in terms of decreasing return levels northward and southward, over Europe the increases of return levels on this path dominate. Similarly to the assessment of changes in return levels for fixed return periods, changes in the return periods themselves can be assessed by means of the GPD analysis. For an event occurring with a 1 year return period under 20C conditions, Figure 2.14 (d) shows return periods derived for 2071-2100 under SRES-A1B conditions. Results are inverse to the findings with respect to return levels, with extended return period off the main storm path and decreased return periods of about 0.5 years on the main path of storm activity. Thus over northern Germany, the Baltics and North-Western Russia initially 1 year recurring events will double in terms of their occurrence frequencies.

It was described in Section 2.3, that over the whole domain a decrease in the total number of identified events can be noticed, with at the same time slightly increasing mean lifetimes of the wind field tracks. This might indicate, that the strong increases in return levels over central and eastern Europe is at least partly a manifestation of severe storm events forming over the Northern Atlantic reaching further east compared to recent climate conditions. It will be investigated in Section 3.4, in how far evidence can be found for more favorable cyclone growth conditions over Europe in the future climate simulations, which could support this assumption.

2.4.1 Statistical Uncertainty

Confidence intervals for derived return levels and return periods can be calculated within the framework of the extreme value analysis as described in Section 2.2.5. The profile likelihood method, able to reproduce unsymmetrical confidence bounds has been used to determine the 90% confidence intervals shown in Figure 2.12 as the area between the two dashed lines. These confidence intervals are estimated on the data basis of ERA-Interim with a 32 year period of data. Estimations of confidence intervals for specific return periods can be found in Table 2.3 showing rather large statistical uncertainties particularly for high return periods. It can be found, that based on the GPD analysis for individual model simulations, these uncertainty ranges are well reproduced. Furthermore within these uncertainty ranges the derived return levels for the global climate simulations under 20C conditions compare well to the respective values from reanalysis. By pooling the 8 individual model simulations to enlarge the statistical data base, these confidence intervals can be considerably reduced, particularly for high return periods.

As will be further discussed in Section 2.4.3 the derived changes in return levels from individual model simulations are significant (if at all) mostly in case of rather frequent events with low return periods. As listed in Table 2.5 for 100 year events affecting Germany, the data base of 30 years is insufficient to derive significant change signals on the basis of the individual model simulations. However by pooling together the 8 individual model simulations to form a data sample corresponding to $8x30$ years for each of the investigated periods, robust change signals can be derived even for these rare events.

2.4.2 Scenario Uncertainty

As in Section 2.3.2 for track density, the dependence of change signals in the return characteristics is analyzed for the different scenarios SRES-A1B, SRES-B1 and SRES-A2 using the 3 member MPI-ECHAM5 ensemble. For future track density changes (i.e. number of events per year), differences depending on the scenario under consideration were found, which were however rather small. While SRES-B1 showed the weakest change signal, for SRES-A1B and SRES-A2 rather similar change signals were derived. Figure 2.15 (middle column) shows the relative changes in the intensity of events occurring once a year for SRES-A1B (top), SRES-B1 (middle) and SRES-A2 (bottom). Considering the increase in intensity over central and eastern Europe, a clear dependence on the scenario can be found, with SRES-B1 showing the weakest, SRES-A1B a medium and SRES-A2 showing the strongest intensity increase. Furthermore the agreement with respect to derived changes amongst the individual simulations is found to be lowest in SRES-B1 and highest in SRES-A2 (indicated by green isolines in Figures 2.15 (middle column)). Under SRES-B1 conditions, there are only small areas over central Europe, where all 3 runs show an increase in the one year return level. In SRES-A1B, model agreement about the intensity increase is larger, and in SRES-A2 over whole Central and Eastern Europe the 3 simulations uniformly indicate increasing 1 year return values. As shown in Figure 2.15 (right column), the dependence on the considered scenario can be identified similarly in the changes of return periods. Return periods of events featuring a 1 year return period in recent climate are found to shorten to about 0.75 years in according to the SRES-A1B scenario over central Europe, while shortening to about 0.8 years in SRES-B1 and to less than 0.7 years in SRES-A2. Even though on large scales, the climate change signals show a clear dependence on the considered scenario, this does not hold when considering changes on a local (grid point) scale. For the grid point [10°E and 51°N] representing the center of Germany, resulting changes in return levels are listed in Table 2.4. Considering different scenario periods (2011-2040, 2041-2070 and 2071-2100) and the 3 different scenarios, variations are found to pose considerable variations onto the detected dependence of large scale signals on the scenario. For example, in the future period 2071-2100 under SRES-B1 scenario conditions, largest increase in the one year

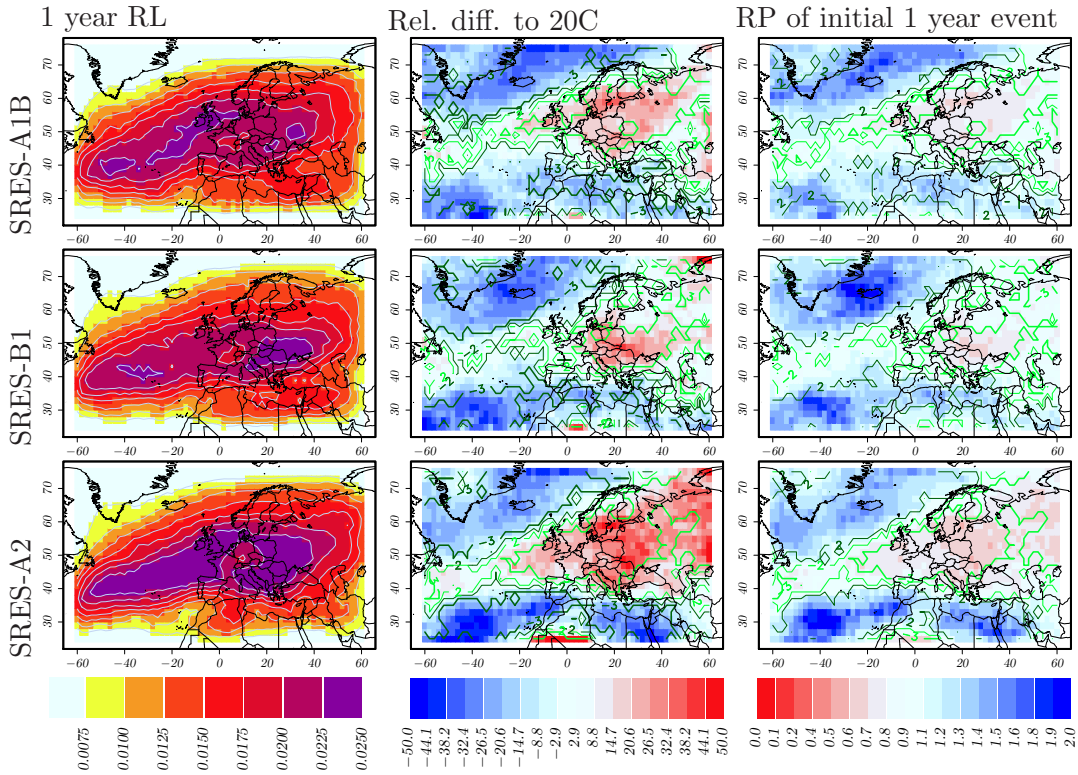

Figure 2.15: (left panel) One year SSI return levels derived from the pooled MPI-ECHAM5 ensemble for the period 2071-2100 under SRES-A1B, SRES-B1 and SRES-A2 conditions. (middle panel) Relative changes in the SSI return levels compared to 1971-2000. Thin contours in light-green (dark-green) indicate areas in which 2 out of 3 runs project an increase (decrease) in return level, thick contours indicate areas in which all 3 runs project an increase (decrease). (right panel) Return period (in years) for 2071-2100 of storms occurring once a year under recent climate conditions. Model agreement on a decrease (increase) in return periods are indicated as before by light-green (dark-green).

return level is found, while for SRES-A1B and SRES-A2 similar increases are detected. As listed in Table 2.4 this holds for higher return periods also. As discussed in terms of diagnosed changes in the track density, on local scales long term natural variability, which may not cancel out analyzing only 3 model projections, can overshadow the detected large scale climate change signals, particularly when considering return characteristics of rare events.

2.4.3 Model Uncertainty

Return levels derived from the single model simulations for recent climate (1971-2000) are shown in Figure 2.16 (left column). Comparing to the corresponding track densities for the individual models (Figure 2.10) it can be confirmed that highest return levels are generally

Scenario	Period	1 year return level	10 year return level	100 year return level
	2011 2040	+10 [-2 +21] %	+10 [-16 +37] %	+11 [-38 +61] %
A1B	2041 2070	+18 [+6 +30] %	+16 [-12 +43] %	+15 [-35 +65] %
	2071 2100	+18 [+6 +30] %	+13 [-13 +40] %	+12 [-36 +59] %
	2011 2040	+10 [-1 +21] %	+7 [-17 +31] %	+5 [-38 +48] %
B1	2041 2070	+8 [-3 +20] %	+20 [-12 +53] %	+39 [-30 +108] %
	2071 2100	+25 [+12 +38] %	+21 [-7 +50] %	+19 [-33 +70] %
	2011 2040	-1 [-11 +10] %	+4 [-21 +29] %	+11 [-39 +60] %
A2	2041 2070	+14 [+4 +25] %	-4 [-23 +15] %	-20 [-49 +9] %
	2071 2100	+19 [+7 +31] %	+13 [-12 +39] %	+12 [-33 +58] %

Table 2.4: Resulting return level changes (%) from GPD analysis for SSI values of tracks passing a 500 km circle around [10° E and 51° N] for the three run MPI-ECHAM5 Ensemble.

Model-Scenario	1 year return level	10 year return level	100 year return level
MPI-ECHAM5 (1)	+15 [-4 +35] %	-1 [-38 +36] %	**-12** [-72 +48] %
MPI-ECHAM5 (2)	+10 [-8 +29] %	+20 [-27 +66] %	+38 [-61 +136] %
MPI-ECHAM5 (3)	+29 [+5 +54] %	+36 [-28 +99] %	+43 [-81 +167] %
FUB-EGMAM	+96 [+61 +131] %	+71 [+1 +140] %	+54 [-59 +166] %
BCCR-BCM2	+52 [+19 +86] %	+47 [-40 +133] %	+47 [-114 +207] %
CNRM-CM3	**+96** [+63 +130]%	**+82** [+8 +156] %	**+73** [-55 +201] %
DMI-ECHAM5	+18 [-1 +38] %	+18 [-26 +62] %	+25 [-58 +108] %
IPSL-CM4	**-28** [-41 -15]%	**-11** [-49 +27] %	+14 [-76 +104] %
ENSEMBLE	+30 [+21 +38] %	+31 [+11 +51] %	+38 [±0 +75] %

Table 2.5: Derived change signals in return levels (in %) resulting from GPD analysis for the location [10° E and 51° N], comparing the period 2071-2100 under SRES-A1B conditions to 1971-2000 under recent climate conditions.

found to be shifted southwards relative to the maximum frequency of winter storm tracks. As noted for the track density the spatial patterns of high return levels are found to be rather zonally orientated when comparing to reanalysis data. Furthermore, considerable inter model differences in both absolute values as well as the spatial patterns can be found. Particularly over the Mediterranean, where return values are generally found to be higher compared to ERA-Interim, models show a large spread. It can be argued, that in these regions, the distribution of SSI values is considerably different from the northern areas particularly the main storm path over the Northern Atlantic. While generally less frequent, the events tend to feature a broader tail distribution (with larger shape parameters ξ). Such distribution generally feature a much stronger increase in return

values with increasing return period, which also leads to larger statistical uncertainties. Derived change signals in the intensity of a storm system with a return period of one year for the individual model projections are shown in Figure 2.10 (right column). Compared to the analysis regarding the occurrence frequency of severe storms, it shows that inter model variations are much larger. However, the spatial patterns are found again to agree at least in principle. Intensities of severe winter storms is found to increase on the path of main storm activity in all models (exceptions pose the IPSL-CM4 and the CNRM-CM3 model simulation), with both absolute increases as well as the spatial patterns varying stronger amongst the individual models. For Germany, results from single model GPD analysis are listed in Table 2.5. In terms of relative increase, change rates are calculated to range between -28 % and +96 % for one year return levels. With respect to confidence intervals (calculated by means of the profile likelihood method), specified in brackets, 4 of the 8 model simulations show significant increases, while only the IPSL-CM4 model shows a significant decrease. Since statistical uncertainties strongly increase with increasing return periods, in case of a 10 year return level, only 2 models show significant increase with no model showing significant decreases. Consistently for 100 year return levels detected signals based on single model output are insignificant in all cases. GPD analysis based on the full ensemble shows a considerable reduction of statistical uncertainty, enabling the diagnosis of statistically significant changes in 1 year return levels of +30% with a confidence interval between +21% and +38%. In case of 10 year return levels, slightly higher relative increase of 31% is found with confidence interval between +11% and +51%. For a 100 year return level a change of +38% is derived, with an increase being close to being significant, once more demonstrating the additional value of an ensemble in comparison to single model evaluation.

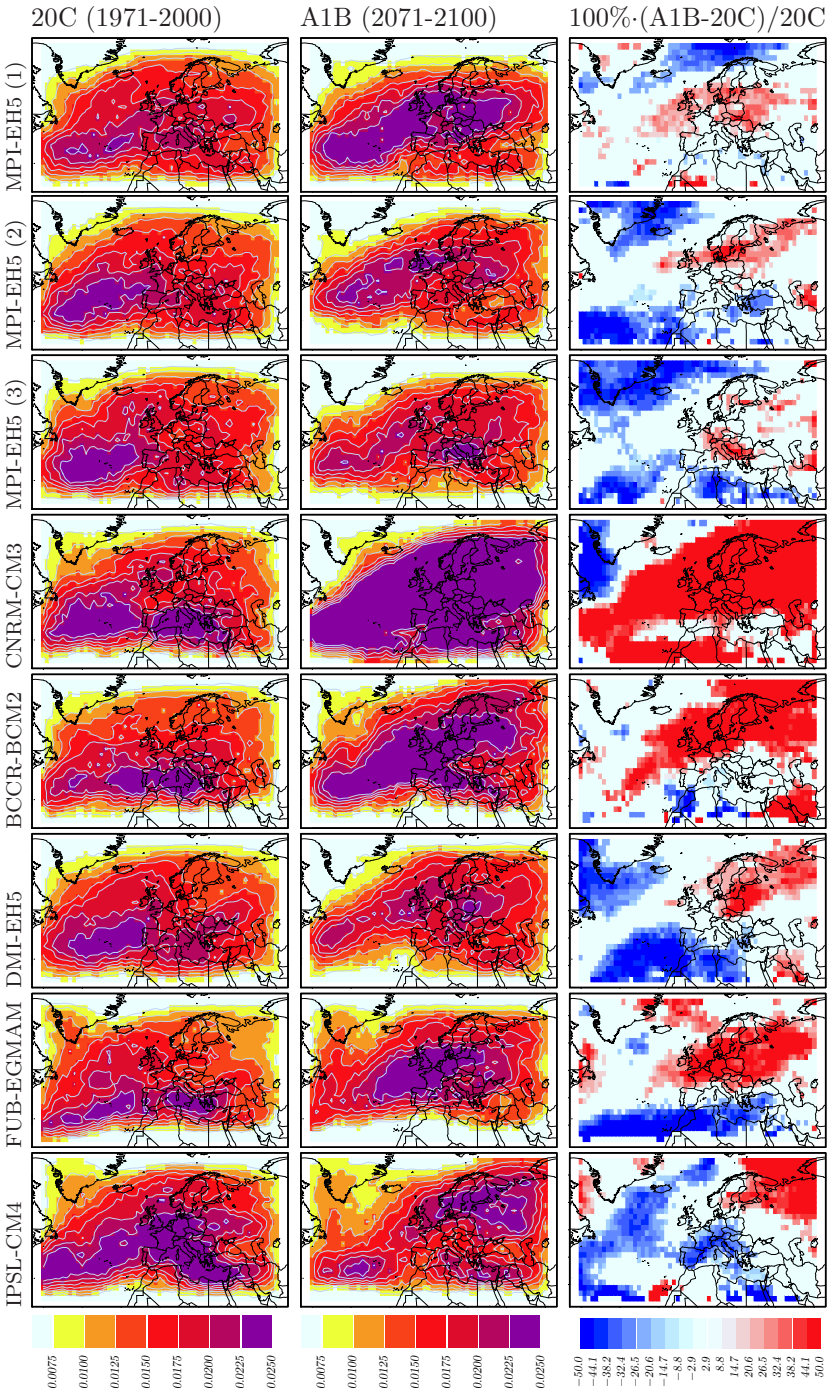

Figure 2.16: One year SSI return levels (dimensionless) derived from the individual GCMs for the period 1971-2000 (left) under recent climate conditions and for the period 2071-2100 (right) under SRES-A1B conditions. (right) Relative differences compared to 1971-2000.

2.5 Summary and Discussion

By means of an objective wind field tracking algorithm developed by Leckebusch et al. (2008), winter storm events were identified in different reanalysis data sets as well as GCM simulations under recent and future climate conditions. In the algorithm continuous areas (with an equivalent area of at least 400x400 km^2) of surface winds exceeding the local 98th percentile of winds are identified in 6 hourly surface winds. These clusters are connected into wind field tracks by means of a nearest neighbor algorithm. Finally, the wind field track must exist for at least 30 hours to be identified as a winter storm event. For historical climate conditions, winter storm events are found to occur most frequently on a band of main storm activity over the northern Atlantic, starting from the typical cyclogenesis regions in the western Atlantic across the British Isles, northern Germany, the Baltic region and reaching towards western Russia. Highest storm frequencies are found to occur west of the British Isles, with approximately 8 to 9 events per winter season, depending on the reanalysis data set and time period under investigation. For Germany track densities are found to vary between 5 events per winter season in the South-East to approximately 7 events per season in the North-West. In terms of the Storm Severity Index (SSI), the intensities of single winter storm events can be assessed. The SSI takes into account the spatial and temporal extent of a wind field related to severe cyclones while assuming a cubic dependence of local impacts related to severe winds. By means of extreme value analysis, return characteristics, i.e. return levels and return periods have been assessed. On the basis of reanalysis data it was found, that areas of highest intensities compare rather well with areas of highest storm frequencies. However areas of highest intensities are shifted slightly south compared to the path of highest storm activity. This is found both over the Northern Atlantic as well as over Europe. While in terms of frequency highest storm activity in Europe is found over the North Sea and the Baltic, according to intensities highest return values are shifted southward centering over Northern Germany. Besides a band of high return values over northern and eastern Europe rather high return values are found over the Mediterranean sea, which can consistently be found in terms of high storm frequencies in these regions. Nissen et al. (2010) presented a climatology of cyclones related to wind storms over the Mediterranean and found areas with high wind activity located south of the Golf of Genoa and south of Cyprus which is in agreement with results presented here. Furthermore, Nissen et al. (2010) find that the majorities of wind storms over the Mediterranean are caused by cyclones located in the Mediterranean regions, while only 31% can be attributed to North Atlantic or Northern European cyclones. Previous studies with respect to the estimation of return values of historical European winter storms mainly focused on extreme value analysis of wind speeds on grid point level (Della-Marta et al., 2008; Kunz et al., 2010; Hofherr and

Kunz, 2010), which essentially differs from the approach chosen here. Based on ERA-40 reanalysis, return levels of severe wind speeds are found to be highest over the Northern Atlantic, while lower values are found over European land (Della-Marta et al., 2008). Over Germany a gradient with highest values close to the Northern Sea coast and decreasing values towards south east is found (Della-Marta et al., 2008) which is in line with results presented here. Sienz et al. (2010) analyze North Atlantic cyclones by means of extreme value statistics and find that extreme cyclones are mainly identified south of Greenland and east of Newfoundland (compare Figure 5 in Sienz et al. (2010)). Considering that often wind fields related to extreme cyclones feature their maximum intensities south of cyclone pressure minima, this corresponds well to the findings achieved with respect to the return values derived for severe wind storm events.

The analysis of GCM model output under recent climate conditions showed, that models are in general able to reproduce observed winter storm climatology in both frequency as well as intensity. However maximum track density in the Northern Atlantic is found to be less pronounced and the main path of storm activity being shifted southward and more zonally orientated. Similarly, intensities of storm events are generally found to be reproduced rather well, however overestimated in the south particularly in the Mediterranean. On the main storm paths over central and northern Europe return values are slightly underestimated respectively. The ability of state of the art global climate models to reproduce observed storm climate has been investigated before, e.g. with respect to MSLP variability patterns (referred to as MSLP storm-track). In comparison to reanalysis data, similar storm-track patterns are found for global climate models with comparable storm-track maxima in both the Pacific as well as the Atlantic sector (Ulbrich et al., 2008). Furthermore, a considerable underestimation of the models storm-track in the Norwegian Sea, which is associated to a commonly observed feature of GCMs called the "zonalization" (Ulbrich et al., 2008; Doblas-Reyes et al., 1998) featuring a too zonally oriented storm track, in line with findings in this study. Renggli et al. (2011) investigated the skill of seasonal forecasts on the basis of track densities with wind field tracks identified using the tracking algorithm as presented in Leckebusch et al. (2008). They find that models are generally able to capture the main features of observed track density over the North-Atlantic and Europe, with most of the models overestimating the track density and reproducing the center of storm tracks shifted to the southwest compared to reanalysis. In line with these results, the results presented here reproduce this southward shifted and too zonally oriented storm track, however in contradiction an underestimation of track density is found for the majority of models. However, the results cannot be directly compared to each other, due to different investigation areas, differences in the considered months of the winter season and different models considered. Also Renggli et al. (2011) discuss, that slight modification in the wind field tracking parameters (e.g.

adopting the minimum lifetime criterion of an event) compared to the original values can lead to systematic (positive) biases in resulting track density. Considering the intensity of rare winter storm events, the evaluation of the model simulation under recent climate conditions shows good agreement with results from historical data sets, with both absolute values as well as the spatial patterns of return levels over the Northern Atlantic and Europe being comparable. Again, highest return levels are found southward of areas with highest storm frequencies. The results presented here suggest that when considering an integrative measure for a storms intensity rather than single location gusts, areas such as the British Isles, Northern Germany, Denmark and parts of the Baltic regions can be found to be highly affected by North Atlantic storm systems on their path towards eastern Europe.

Under changed climate conditions fundamental changes in frequency as well as intensity of European winter storms are diagnosed. Areas of highest track density over the Northern Atlantic are found to be slightly shifted northward with a focusing or narrowing of main paths of storm activity. Most pronounced changes are found over central, northern and in particular over eastern Europe, with strong increases in track density of about 1 event per year (from about 6.5 to 7.5 p.a.) towards the end of the 21st century according to the SRES-A1B scenario. These findings are in agreement with previous findings (Leckebusch et al., 2006; Bengtsson et al., 2006; Donat et al., 2010b), considering the frequencies and intensities of European cyclones and related severe wind speeds over Europe. Donat et al. (2010b) identify an increase of storms related cyclones on a band which lies slightly more north compared to the band of increased storm frequency found here for wind storm tracks. This can be explained by the fact, that generally fields of high wind speeds related to deep extra tropical cyclones are found south to the cyclone core (due to addition of geostrophic wind speed and system translation speed). Also the magnitude of change in frequencies is comparable, however increase rates are slightly higher in the results presented here. Consistenly to the results obtained for winter storm frequencies, changes in return levels (i.e. intensities) of rare winter storm events reaching the eastern parts of Europe and particularly the Baltic region and the Barents Sea are found to increase by up to 50% according to the SRES-A1B scenario. For Germany 1 year return levels are found to increase by about 30% while events with higher return periods feature even stronger increases of up to 38% for 100 year events. In line with these results Della-Marta and Pinto (2009) quantified changes in storm frequency and intensity over the North Atlantic and Europe in terms of pressure minima and vorticity maxima of cyclones. Under SRES-A1B and SRES-A2 scenario conditions they find significantly shortened return periods particularly for the area between the British Isles, the North-Sea and western Europe. Consistently studies have shown that return levels (return periods) of windstorms and associated loss potentials significantly increase (decrease), particularly

over central Europe.

Statistical uncertainties, especially when deriving intensities of events with high return periods were found to be extremely large when considering single model output hindering the diagnosis of robust (significant) results. By analyzing the multi model ensemble which enlarges sample sizes, statistical uncertainties can be reduced considerably enabling the diagnosis of statistically significant trends in return values even for 100 year events. Scenario uncertainties were assessed by means of a multi-scenario but single model ensemble using MPI-ECHAM5 output. Changes in the frequency and intensity of severe wind storms are found to depend on the considered scenario with strongest changes identified for the SRES-A2 scenario, intermediate changes for the SRES-A1B scenario and less pronounced changes for the SRES-B1 scenario. Despite the differences in magnitude, spatial patterns of detected changes are consistent for the 3 considered scenarios underlining the robustness of the results. It was found however that on regional scales, the magnitude of identified changes can considerably vary due to the large statistical uncertainties and due to natural variability. This holds particularly when considering the return periods or return values of very rare events. By analyzing a multi model ensemble consisting of 8 model simulations with 5 different model formulations it was shown that model uncertainties in fact pose the dominating source of uncertainty. Even though all considered models feature a narrowing of storm paths over the North Atlantic, associated to increased storm frequencies and intensities over central and Northern Europe, both magnitude and spatial patterns of change signals strongly depend on the model under consideration. This underlines the necessity of multi-model investigations as presented here. Donat et al. (2011a) argue, that by considering a multi-model ensemble, differences in derived changes due to both internal variability as well the individual model formulations are sampled and would tend to be cancelled out. Whether the range of possible model formulations and thus the inherent uncertainties are sufficiently sampled by the models available today still remains an open question.

Chapter 3

Mechanisms Related to Changes in European Winter Storm Climate

3.1 Introduction and Current State of Research

Changes in the winter storm climate in Europe under possible future climate conditions have been analyzed in Chapter 2. Main findings were that significant increases in both number as well as intensity of severe storm systems, traveling along the main path of storm activity across the Northern Atlantic towards Europe, can be found. Offside this main path of storm activity, decreases in storm frequency and intensity have been found. Indicated by an increase in the mean lifetime of wind storm events and the general finding that the overall number of identified events over the North Atlantic sector is decreasing, it can be argued that intense storm systems over the Atlantic tend to reach further east before dissipating their energy and thus loosing their intensity. It shall be investigated in this section, in how far the conditions supporting the growth and intensification of cyclones may change in an altered climate. Due to its central role, governing much of weather variability in Europe, the North-Atlantic-Oscillation (Walker and Bliss, 1932) will be assessed, focusing on possible modifications with respect to its phase and its spatial pattern. Changes in the North-Atlantic-Oscillation shall furthermore be related to features of the large scale atmospheric circulation, namely the tropical Hadley cell circulation. By transporting energy and angular momentum poleward the Hadley cell is playing a fundamental role in the earth's climate Lu et al. (2007) affecting also mid-latitude climate conditions, e.g. by influencing the location of jet streams and storm tracks (Seidel et al., 2008). Environmental factors contributing to the genesis and intensification of cyclones have been investigated in the past (Schultz et al., 1998; Ulbrich et al., 2001; Pinto et al., 2008). Conditions favoring the growth of cyclones have been found to be the availability of latent heat (Chang et al., 1984; Ulbrich et al., 2001), the presence of upper-air divergence in particular close to the jet exit region (Uccellini and Johnson, 1979; Baehr et al., 1999; Ulbrich et al., 2001) as well as upper-air baroclinicity (Hoskins and Valdes, 1990; Ulbrich et al., 2001; Pinto et al., 2008). In a baroclinic atmosphere, planes of constant pressure

(isobaric planes) are tilted against planes of constant temperatures (isothermal planes) allowing the conversion from potential to kinetic energy through a horizontal motion of air masses. In such conditions, wave perturbances can take up energy by lowering their center of mass converting potential into kinetic energy and grow into a cyclonic system (e.g. Bott (2012), p. 309 f.). Areas of high baroclinicity can for example be found at the polar front being one major cyclogenisis region. In a warmer climate, changes in storm tracks have been related to altered conditions in terms of baroclinicity, with findings indicating that it is rather upper level than lower level baroclinicity responsible for diagnosed change signals Lunkeit et al. (1996); Ulbrich and Christoph (1999). It has been shown that there are strong connections between the phase of the North Atlantic Oscillation (NAO) and the occurrence and intensity of European winter storms (Donat et al., 2010a), with positive NAO phases correlating with favorable cyclone growth factors (Pinto et al., 2008). In fact, much of wintertime variations in the North Atlantic and European climate is influenced by the NAO which has been first described by Walker and Bliss (1932). The NAO consists of two centers of action, a low pressure center located over Iceland and high pressure center over the Azores. In it's positive phase the low pressure and high pressure systems are strengthened, leading to a strengthened westerly flow across the mid-latitudes, colder and drier conditions in northwestern Atlantic and Mediterranean regions and warmer and wetter in northern Europe, the eastern United States, and parts of Scandinavia (Visbeck et al., 2001). In it's negative phase, the westerly flow is reduced and related anomalies in temperature and humidity are inversed (compare e.g. Figure 9 of Wanner et al. (2001)). Variations of the NAO occur on a large range of time scales from days to centuries, however most dominant on the inter annual to decadal time scales (Pinto and Raible, 2012). It has been found, that under increased greenhouse gas forcing (GHG), the strength of the NAO increases (Stephenson et al., 2006; Osborn, 2004; Gillett et al., 2003). Furthermore findings indicate that under future climate conditions, NAO action centers feature an eastward shift with implications on storm track activity over Europe (Ulbrich and Christoph, 1999). Variability of the NAO occur on time scales including inter-annual to multi-decadal variations (Visbeck et al., 2001; Pinto and Raible, 2012). The origins for NAO variability, particularly the lower frequency variability and long term changes, are currently under debate with multiple factors being related to the NAO (Pinto and Raible, 2012) and no consensus has been found regarding the processes that are responsible for observed low-frequency variations of the NAO (Visbeck et al., 2001). While authors have suggested external parameters like volcanos, solar activity, or stratospheric-tropospheric coupling being the major drivers of the low frequency variability, others have suggested internal variability of the atmosphere being the driving factors (Pinto and Raible, 2012). Some studies consider sea surface anomalies (SST) over the North Atlantic Ocean, which can be related to the the Atlantic meridional overturning

circulation, as a crucial influence on the NAO (Timmermann et al., 1998; Marshall et al., 2001). Recent studies however provided evidence of links between long term trends in the NAO and precipitation trends over the tropical ocean (in particular the Indian ocean) which are related to a warming of the underlying ocean (Selten et al., 2004; Hurrell et al., 2004; Hoerling et al., 2004). It was found that extratropical response to tropical ocean warming occurs on rather short time scales of about 40 days, which is why the authors argue for dynamical processes responsible for this teleconnection. It was speculated that the response to Indian ocean forcing is accomplished through an adjustment of local storm tracks, the precise mechanisms however remain subject to further research (Hoerling et al., 2004). A poleward shift and intensification of storm tracks have consistently been identified in model projections during the 21st century (Ulbrich and Christoph, 1999; Yin, 2005; Wu et al., 2010) and have been found to be related to a poleward shift and an upward expansion of the mid-latitude baroclinic regions (Yin, 2005). These baroclinicity changes are in turn consistent to an enhanced warming in the tropical upper troposphere (Yin, 2005) and have been related to a general widening of the tropical circulation, namely the Hadley cell (Seidel et al., 2008; Lu et al., 2007). Thus, after an assessment of changes in the phase of the NAO (Section 3.3) and changes in mid-latitude baroclinicity (Section 3.4) and their relation to the growth of intense cyclones, the changes in the Hadley cell characteristics shall be assessed and investigated with respect to their influence on the NAO.

3.2 Data and Methods

3.2.1 Reanalysis Data

The ERA-Interim reanalysis data set (Dee et al., 2011) is used. The reanalysis is computed on a T255 grid with 60 vertical model layers, supplying data on a grid with spacing of about 0.70 °(≈ 79km) and is available for the period 1979-2010. For the assessment of the NAO, monthly mean MSLP (Mean Sea Level Pressure) fields for the area -90°to 30 °E and 20°to 85°N are evaluated. Furthermore, to assess the characteristics of the tropical circulation, the zonal mean stream function is calculated, based on monthly mean meridional wind components on the pressure levels 10, 30, 50, 70, 100, 150, 200, 250, 300, 400, 500, 700, 850 and 1000hPa. For evaluation of corresponding upward and downward fluxes, vertical wind components are used additionally.

3.2.2 Global Climate Model Data

The NAO and respective changes shall be assessed for the model projections evaluated in the previous Chapter (compare description of model simulations in Section 2.2.2).

Monthly mean MSLP fields for the region -90°to 30 °E and 20°to 85°N are evaluated for all members of the multi model ensemble from the ENSEMBLES project (van der Linden et al., 2009) as listed in Table 2.1. These include recent climate simulations for 1860-2000 (20C), forced with constant Green House Gas (GHG) concentrations according to recent observations and climate projections for the period 2001-2100, forced with GHG concentrations following the SRES-A1B Scenario (Nakicenovic et al., 2000). Furthermore, analysis of baroclinicity and Hadley cell characteristics are conducted on the basis of the ECHAM5-MPIOM single model ensemble (compare Section 2.2.2). Zonal mean baroclinicity is assessed, with calculations based on monthly mean temperatures and geopotential heights at the pressure levels 10, 30, 50, 70, 100, 150, 200, 250, 300, 400, 500, 600, 700, 775, 850, 925 and 1000hPa. Hadley cell characteristics, analogously to reanalysis data are assessed using monthly mean meridional and vertical wind components at these pressure levels. Furthermore, to relate baroclinicity to growth properties of cyclones, 6 hourly resolved temperature fields, horizontal wind fields (including zonal and meridional wind components) and geopotential heights are used to calculate the Eady growth rate. As described in Section 3.2.4, the Eady growth rate is calculated between two model layers. To calculate upper troposphere Eady growth rate, listed variables at the model layers 300 and 500 hPa are used and lower troposphere Eady growth rate is calculated using the data on pressure levels 700 and 850 hPa.

3.2.3 Assessment of the North Atlantic Oscillation

The North Atlantic Oscillation (NAO) is described as a spatial oscillation in the troposphere over the North Atlantic European sector, strongly influencing the regional weather and climate in Europe, particularly during winter (Pinto and Raible, 2012). Early descriptions of the NAO were based on surface pressure measurements at single observation stations (Walker, 1924; Walker and Bliss, 1932), with indices to assess the phase of the NAO being calculated as the difference of normalized pressures over the Azores/Lisbon and Iceland (Hurrell, 1995). With the emergence of computing resources, definitions of the NAO derived by means of principle component analysis aroused (e.g. Barnston and Livezey (1987)), extracting the leading mode of variability over the North Atlantic from mean sea level pressure data. The methodology employed in the following sections takes into account monthly mean MSLP anomaly fields for the area -90°to 30 °E and 20°to 85°N. The anomaly fields are subjected to an EOF analysis, resulting in a set of principle components (PC's) and respective principle component loadings. The leading mode, represented by a variability pattern, as shown in Figure 3.2 (left) for ERA-Interim reanalysis, with its action centers over Iceland and close to the Azores is regarded as the NAO pattern. Normalizing the respective PC loading on a mean of zero and standard deviation of 1 yields the definition of the NAO index used in the following. It needs to be

kept in mind, that different NAO definitions, as well as the choice of the analysis region influences both the derived NAO pattern as well as the NAO index (Pinto and Raible, 2012). Moreover, due to long term variations and long term trends, the NAO might undergo certain changes in both shape as well as phase which is important to keep in mind. Furthermore, the representation of the NAO might differ in reanalysis and model data, resulting in differing NAO patterns derived. To assess and compare NAO characteristics amongst different data sources, one way is to calculate the NAO pattern from the reference data source (e.g. reanalyses) and calculate the NAO indices as the principle component loadings by projecting onto this pattern. Alternatively, NAO patterns can be derived by means of PC analysis from each individual data source (reanalysis and individual models), taking into account the possible differences in the NAO representations. In the following sections, NAO patterns are determined individually for each model simulation (as well as reanalysis) for the reference period (1971-2000). To study changes in the phase of the NAO, PC loadings are then calculated for future climate simulations by projecting onto the respective NAO patterns from 1971-2000. Secondly principle component analysis is repeatedly performed for different future periods to investigate on changes in the NAO pattern itself.

3.2.4 Eady Growth Rate

In the formulation based on the horizontal gradients in temperature and a measure of the static stability, the zonal mean Eady growth rate (σ_{BI}) will be calculated as

$$\sigma_{BI} = 0.31 \cdot g \cdot N^{-1} \cdot T^{-1} \cdot \left| \frac{\partial T}{\partial y} \right|, \tag{3.1}$$

where T is the zonal mean temperature and N is the Brunt-Vaisala frequency being a measurement of the static stability (compare (Lindzen and Farrell, 1980; Yin, 2005)). This calculation of σ_{BI} is purely based on the zonal mean temperature profile, if assuming dry conditions in the calculation of N.

The zonal averaging is of course an oversimplification of the 3 dimensional structure of the atmosphere. Thus, additionally the horizontal characteristics of σ_{BI} will be assessed by calculating their respective fields on a fixed level height. For this, σ_{BI} is calculated in terms of vertical gradients in horizontal winds and a measure of the static stability (Hoskins and Valdes, 1990; Paciorek et al., 2002). In this formulation the Eady growth rate is calculated as

$$\sigma_{BI} = 0.31 \cdot f \cdot N^{-1} \cdot \left| \frac{\partial \vec{v}}{\partial z} \right|, \tag{3.2}$$

with $\vec{v} = (u, v)$ beeing the horizontal wind vector, and N beeing the Brunt-Vaisala frequency.

3.2.5 Hadley Cell Characteristics

The general circulation of the atmosphere, forced by a surplus of net radiation in equatorial regions and a deficit in polar regions, can be described in simple 3 cell model illustrated in Figure 3.1. It features the Hadley cell (HC) as a large scale circulation cell with warm air rising near the equator being transported poleward in high altitudes. Cooling down the air sinks at around 30°N leading to a very stable high pressure belt in these latitudes. Similarly but less intense, the polar cell (PC) includes rising air at around 60°N and sinking air in polar regions, which analogously leads to a stable low pressure system around 60 °N. The mid-latitudes (called Ferrel cell in the 3 cell model) are predominantly influenced by these 2 pressure belts at 30°N and 60°N. As proposed by Oort and Yienger

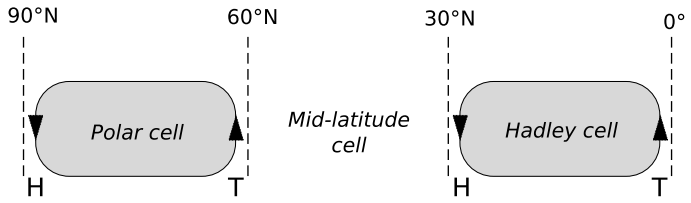

Figure 3.1: Simplified 3 cell representation of the atmospheric circulation featuring the tropical Hadley cell, the mid-latitude Ferrell cell and the polar cell.

(1996) and Mitas and Clement (2005), the structure of the Hadley cell can be assessed by means of the zonal mean of the stream function for the mean poleward flow. This two dimensional stream function $\psi(\phi, p)$, with ϕ being the latitude and p being the pressure, is computed by vertical integration of monthly meridional winds (Oort and Yienger, 1996; Mitas and Clement, 2005) and is given in kgs^{-1}. Identifying the maximum of the stream function within the Hadley cell yields an estimate for the Hadley cell strength. Assessing the zero points of the stream function in 500 hPa ($\psi_{500} = 0kgs^{-1}$) then yields an estimate for the location of the outer boundaries of the Hadley cell (compare e.g. (Lu et al., 2007; Johanson and Fu, 2009)), since the stream function being zero indicates that at the respective latitude no meridional mass transport is diagnosed.

3.3 Changes in the North Atlantic Oscillation (NAO)

3.3.1 The NAO in Historical and Recent Climate

The NAO pattern, as represented by the normalized EOF pattern resulting from principle component analysis (compare Section 3.2.3) based on monthly mean MSLP anomaly fields is shown in Figure 3.2. Based on the ERA-Interim reanalysis for the period 1979-2010 (left), NAO centers of action are identified with their centers over Iceland and close to the

Azores, leading to an enhanced pressure gradient over the Northern Atlantic and Europe, particularly over the British Isles, the North Sea as well as the Baltic Sea. Similarly, the NAO is assessed from the global climate model simulations under recent climate conditions (compare Section 3.2.2). Averaging the normalized EOF patterns (interpolated onto a unique grid of 2.5°resolution) derived from single model output yields the ensemble mean representation of the NAO pattern shown in Figure 3.2 (right). With grey contour lines showing the NAO pattern from ERA-Interim, the NAO centers of action are found to be slightly shifted, namely towards Greenland in case of the Iceland low and north-east in case of the Azores high. Except for these shifts, patterns derived from model simulations are well comparable to historical reanalysis data. Evaluating the NAO patterns for the single model simulations (shown in Figure A.2 of Appendix A), reveals considerable differences in the representation of the NAO, with respect to both the location of pressure centers as well as their extent. Particularly the IPSL-CM4 model simulation produces an enhanced intensity of the southern action center, while the FUB-EGMAM model shows a strongly increased intensity of the northern action center with a much enlarged extent stretching over large parts of Greenland and Iceland. Furthermore, notable differences in the NAO pattern are found for the CNRM-CM3 model, producing a southern action center shifted south-east and being located over North-West Africa and Spain.

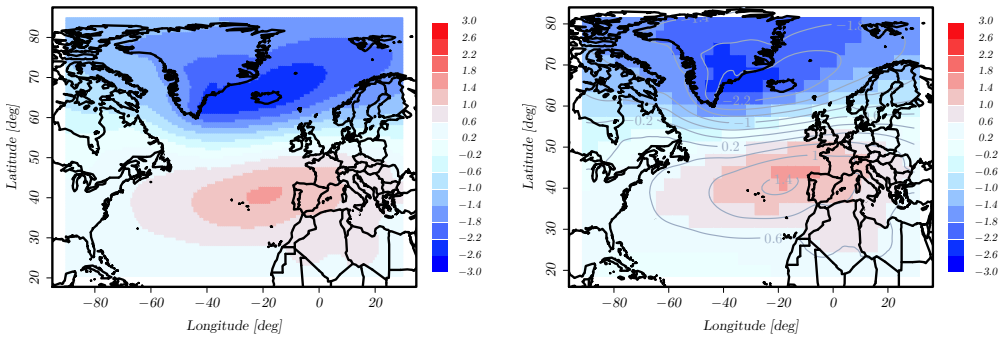

Figure 3.2: (left) First EOF of monthly mean MSLP anomaly fields from ERA-Interim (October-March of 1979-2010). (right) Ensemble averaged EOF of the multi-model ensemble for October-March of 1971-2000.

3.3.2 Future Changes in the NAO Strength

By projecting the monthly mean MSLP fields from the individual model simulations onto the respective NAO patterns (as shown in Figure A.2), the PC loadings are calculated and normalized for the period 1861-2000 to be interpreted as the NAO index. Resulting 15 year running mean NAO indices are shown in Figure 3.3 (left) for the individual model simulations for the Period 1860-2100 with recent climate GHG forcing conditions until

2000 followed by the transient simulations according to the SRES-A1B scenario conditions. Comparing the period 2071-2100 to the reference period 1971-2000, it can be found that

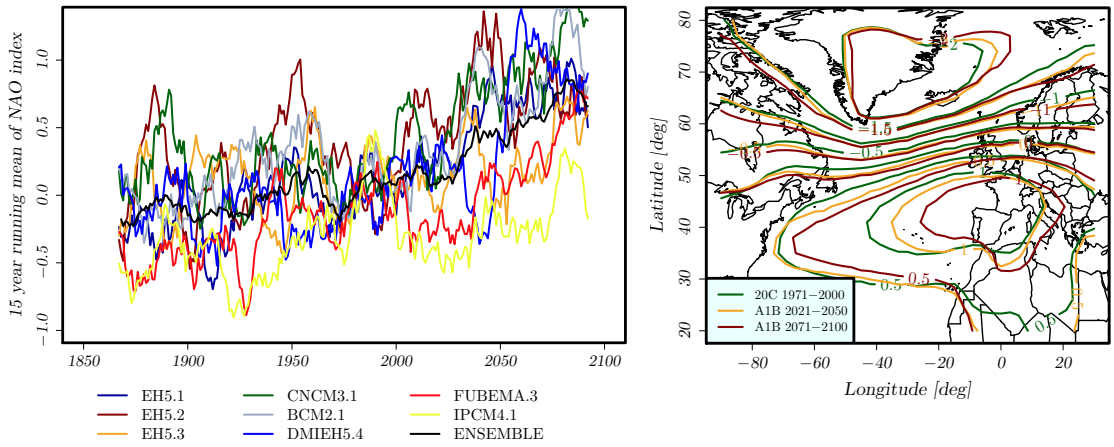

Figure 3.3: (left) 15 year running mean NAO index, calculated from the individual models of the multi-model ensemble for 1861-2100 analyzing recent climate simulations before year 2000 and followed up by the SRES-A1B projections thereafter. (right) Ensemble averaged EOF of the multi-model ensemble for 1971-2000 (green), 2021-2050 (yellow) and 2071-2100 (red).

all model simulations except for the IPSL-CM4 simulation show significant increases in the NAO index, indicating a shift towards the positive phase of the NAO. In terms of the yearly NAO index, the increase (as listed in Table 3.1) ranges from $+0.59\sigma_{20C}$ for the FUB-EGMAM simulation and $+1.15\sigma_{20C}$ in the CNRM-CM3 simulation (σ_{20C} being the standard deviation of the yearly NAO index of the individual model simulation in the period 1971-2000). The IPCM as the only model producing a slight decrease in the mean NAO index, accounting for $0.08\sigma_{20C}$, can be found to be in a positive NAO phase in the period 1971-200 when comparing to the total 20C period starting 1860 with generally negative NAO index values (compare Figure 3.3 (left)). Thus, choosing a different reference period than 1971-2000, results would be altered. In the ensemble mean, the NAO index is found to increase by $+0.7\sigma_{20C}$.

3.3.3 Changes in the NAO Shape

Besides changes in the NAO index, changes in the shape of the NAO pattern are investigated. For this, principle component analysis is performed separately for the period 1971-2000 of the 20C simulations and for the periods 2021-2050 and 2071-2100 from the SRES-A1B scenario simulations. The resulting ensemble average of resulting EOF's is shown in Figure 3.3 (right). Compared to recent climate conditions, a consistent and gradual eastward shift of the southern action center is found during the 21st century.

	A1B		A2		B1	
	∅	σ	∅	σ	∅	σ
MPI-ECHAM5 (1)	0.60	1.04	0.95	1.19	0.56	1.04
MPI-ECHAM5 (2)	0.65	1.18	1.11	1.31	0.65	1.35
MPI-ECHAM5 (3)	0.63	0.78	0.87	1.10	0.57	0.87
CNRM-CM3	1.15	1.01				
BCCR-BCM2	1.11	0.98				
DMI-ECHAM5	0.96	1.02				
FUB-EGMAM	0.59	0.60				
IPSL-CM4	−0.08	0.83				
Ensemble	0.70	1.00				
MPI-ECHAM5 Ensemble	0.63	1.00	0.98	1.19	0.59	1.09

Table 3.1: Mean yearly NAO index and its standard deviation in the period 2071-2100, both specified in units of σ_{20C} being the standard deviation of yearly NAO index in the reference period 1971-2000.

Also changes in the shape of the northern action center are detected, with an expansion of the Iceland low towards the east. In it's positive phase, these changes in the NAO's shape have major implications on the pressure gradients present over Northern Europe being increased compared to the recent climate NAO (compare 3.3 (right)). Considering changes in the NAO patterns, based on the single model simulations (as shown in Figure A.3) substantial inter model differences in the changes of the NAO pattern are found. While MPI-ECHAM5 (2), MPI-ECHAM5 (3), BCCR-BCM2, DMI-ECHAM5 and FUB-EGMAM show distinctive eastward shifts in the southern action center, IPSL-CM4 shows very slight eastward shifts and CNRM-CM3 shows no clear shift at all. An exception poses the 1st run of MPI-ECHAM5, for which a northward rather than an eastward shift is found. Regarding the northern action center, the MPI-ECHAM5 simulations produce a consistent eastward expansion, however with varying strength. Also the other models are found to generate such eastward expansions, with an exception being FUB-EGMAM showing an opposite trend with the northern action center retreating in its eastward extent.

The diagnosed changes in the NAO can be related well to the diagnosed changes in track density as discussed in Section 2.3.3. CNRM-CM3, showing the strongest increase in the NAO index, consistently produces the strongest track density increases along the path of storm activity. On the opposite the IPSL shows a slight decrease in NAO strength being also the simulation exhibiting a general decrease in track density. The moderate increases in track density over the Baltic region produced by the IPSL-CM4 however relate well to the changes in the NAO shape including a slight shift of NAO action centers towards the

east. In general it can be noted, that the combination of a shift in NAO phases combined with distinct changes in the NAO pattern itself is related to the diagnosed track density changes. While the shift towards a more positive NAO phase leads to increased pressure gradients over the northern Atlantic which relates well to the the finding of a generally increased storm frequency over the Northern Atlantic, the shift of action centers towards the east can be assumed to be at least partly related to the finding that most distinct track density changes are identified over the British isles, the Northern sea and the Baltic region (compare Figure 2.7).

3.4 Changes in Baroclinicity

3.4.1 Zonal Mean Eady Growth Rate

Temperature increases in a warmer climate are not uniformly distributed across the hemisphere. Global climate projections feature enhanced warming of the (north-) polar lower troposphere as well as an enhanced warming of the tropical upper troposphere. These non uniform changes in the atmospheric temperature profile obviously lead to distinct changes in the atmospheric baroclinicity. Figure 3.4 (left) shows changes in the zonal mean temperature profile (for December through March) as derived from the ensemble of 3 ECHAM5-MPIOM simulations. The temperature profile for the period 2071-2100 (according to the SRES-A1B scenario) features a typical upward shift of the tropical tropopause, accompanied by a strong warming in the upper tropical troposphere. Highly

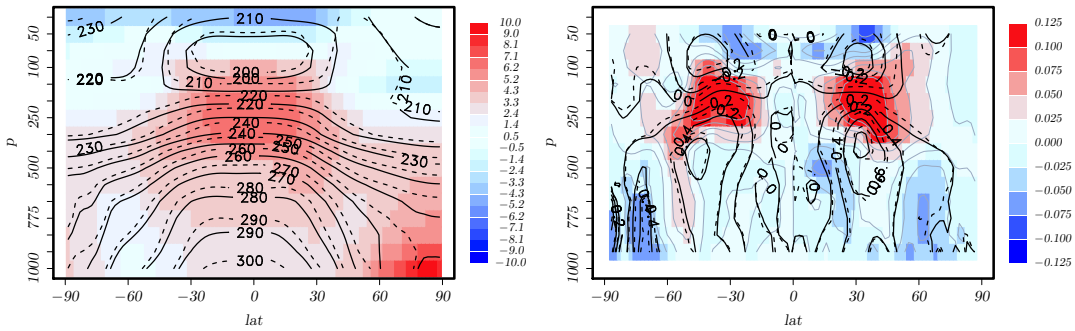

Figure 3.4: (left) Changes in the mean temperature profile (in Kelvin) according to the three run ensemble of MPI-ECHAM5. Temperature isolines for the period 1971-2000 (20C) are shown in solid and for the period 2071-2100 (A1B) as dashed lines. (right) Resulting changes in σ_{BI} (in day^{-1}).

baroclinic zones are identified from this temperature profile in regions of strong temperature gradients (on constant pressure planes) which are typically found in the mid-latitude upper troposphere. Zonal (and temporal) mean Eady growth rate (according to Equa-

tion 3.1) is depicted in Figure 3.4 (right) as black solid isolines for the recent climate conditions, identifying the maximum baroclinicity at around 30°North and in about 400 hPa height. Similarly a maximum in baroclinicity is identified on the southern hemisphere at about 45°South in a similar height. Under SRES-A1B conditions (2071-2100) the regions of high baroclinicity are found to shift poleward and extent further upward which can be seen in Figure 3.4 (right) by a dipole structure of decreasing Eady Growth Rate (EGR) at around 20°North in 500hPa height and strongly increasing EGR values at approximately 35°in 200 hPa height. These results based on a single model ensemble using ECHAM5-MPIOM is consistent with results from a multi model study analyzing 15 coupled atmosphere ocean models (Yin, 2005). The authors identify poleward shifts in storm tracks accompanied by a poleward shift and upward expansion of the mid-latitude baroclinic regions consistent to the results presented here.

3.4.2 Changes in North Atlantic Eady Growth Rate

For the North-Atlantic and Europe changes in the maximum Eady Growth Rate (σ_{BI}) as described by Equation 3.2 (compare Lindzen and Farrell (1980), Hoskins and Valdes (1990) and Paciorek et al. (2002)) is evaluated. Calculations are based on 6 hourly resolved fields from ECHAM5-MPIOM for the region $60°W - 60°E$ and $25°N - 75°N$. The EGR is assessed for the upper troposphere taking into account the pressure levels 300 and 500 hPa. Resulting EGR values are analyzed with respect to their long term means for the months December through February. The ensemble mean of σ_{BI} for the 3 ECHAM5-MPIOM simulations in the period 1971-2000 (20C) is shown in Figure 3.5 (left) as black isolines. It features a zone of high baroclinicity over the North-Atlantic stretching from Newfoundland towards Northern Europe, with mean EGR values ranging up to 1.4 day^{-1}, which corresponds well to the North-Atlantic storm track. Towards the North and particularly towards the South, EGR values are strongly decreasing with mean values of 1.1 day^{-1} over Greenland and values below 0.9 day^{-1} south of 30°N. Under SRES-A1B conditions for the period 2071-2100, mean EGR are found to undergo distinct changes (indicated by dashed contours in 3.5, left). Mean EGR values are found to increase (except for some regions over North Africa and parts of the Mediterranean) throughout the investigation area. Particularly, the highly baroclinic zone related to the NA storm track is found to expand, reaching further towards Northern Europe in the SRES-A1B simulations. Particularly over Northern and Eastern Europe as well as Russia this leads to strong increases in the mean EGR of about 0.1 day^{-1}, corresponding to an increase of about 10%. These findings are in agreement with previous studies (Lunkeit et al., 1996) and (Ulbrich and Christoph, 1999), identifying increases in the upper tropospheric baroclinicity over the North-East Atlantic. Comparing to diagnosed changes in frequencies of winter storms (compare Section 2.3), particularly the increased mean Eady growth rate

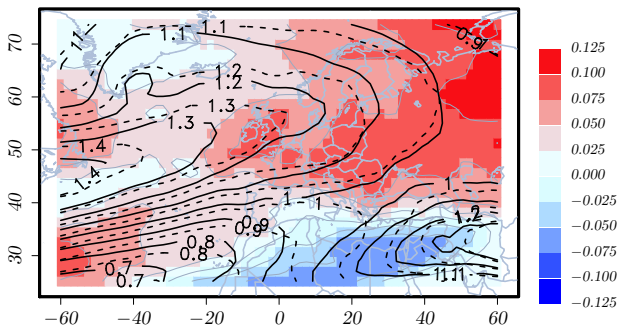

Figure 3.5: Changes in the upper tropospheric Eady growth rate (σ_{BI} in units of day^{-1}) over the North Atlantic and Europe according to the SRES-A1B scenario based on the three run ensemble of MPI-ECHAM5.

over Northern and Eastern Europe can be related to the strong increases in the frequency of severe storm systems in these regions. Upper tropospheric Eady growth rate has been considered here, which has previously been found to be be related to changes in storm track activity (Lunkeit et al., 1996; Ulbrich and Christoph, 1999). Cyclonic systems forming over the North Atlantic and travelling towards Europe will, according to the results presented here, find more suitable growth conditions leading to enhanced frequencies of severe storm events as well as increased lifetimes and severity of events. The results are thus well aligned with diagnosed changes presented in Chapter 2.

3.4.3 Relation to the NAO

As shown by Pinto et al. (2008), the phase of the NAO influences the environmental factors contributing to cyclonic growth factors. In positive NAO phases a larger area with suitable growth conditions, including values for the Eady growth rate, can be found which is shown to be better aligned with the cyclone tracks related to increased cyclone life times and intensities. Dependence of σ_{BI} on the NAO phases as represented in the ECHAM5-MPIOM simulation ensemble are shown in Figure 3.6. Confirming results from Pinto et al. (2008), regions of high baroclinicity over the North Atlantic are found to extend further east in positive NAO phases, while in the negative phase the eastward extend is reduced. Furthermore, areas of high baroclinicity are distinctively shifted northward (southward) in the positive (negative) phases. In the positive NAO phases, this leads to enhanced EGR values in the regions of typical paths of extreme cyclones (compare Figure 4a of Pinto et al. (2008)), with decreased values in these regions in the negative NAO phases. Comparing Figure 3.6 to the changes in the mean Eady growth rate identified for changed climate conditions (Figure 3.5) reveals, that a shift towards more positive NAO phases can in fact account for some of these changes. However essential parts of EGR changes, including particularly the strong increases over Eastern Europe, can not

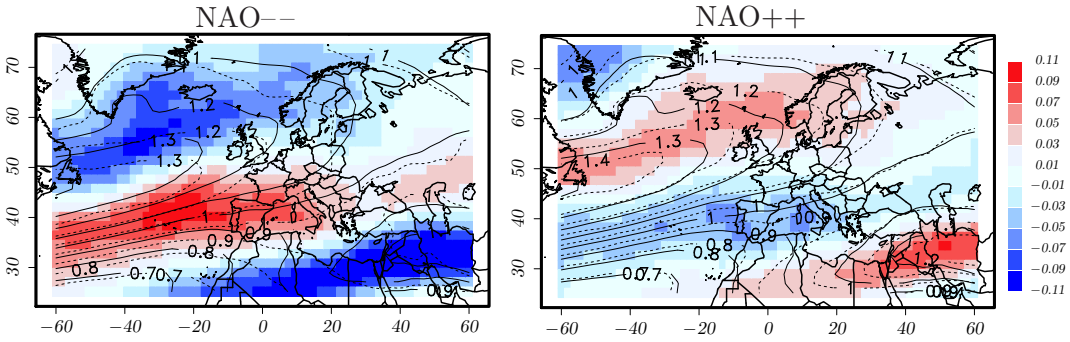

Figure 3.6: Composites of the upper tropospheric Eady growth rate (σ_{BI} in units of day^{-1}) for the strong negative (left) and the strong positive (right) NAO phase.

be explained by an increase of the NAO strength solely. However, as shown in Section 3.3, the NAO undergoes some major changes with respect to it's shape including a slight northward as well a distinct eastward shift of it's centers of action. It can be argued, that these changes in the shape of the NAO can at least partly account for the identified changes in the EGR over the North Atlantic and Europe.

3.5 NAO Influences on European Winter Storms and their Impacts

3.5.1 Dependence of Winter Storm Frequency on the NAO

The NAO index is calculated by means of principle component analysis as described in Section 3.2.3, deriving monthly NAO index values from the PC loadings. To gain a winter season NAO index, monthly values are averaged over the months December through February. Finally, the resulting indices are normalized on a mean of zero and a standard deviation of 1. As described in Pinto et al. (2008), the NAO can classified into it's different phases according to Table 3.2. Even though Pinto et al. (2008) consider daily NAO indices, it seems justified to adopt their classification here for monthly as well as yearly NAO values, since resulting NAO time series are appropriately normalized. To

Acronym	Phase	Index range		
NAO−−	strongly negative		NAO	< -1.5
NAO−	negative	-1.5 ≤	NAO	< -0.5
NAO 0	indifferent	-0.5 ≤	NAO	< 0.5
NAO+	positive	0.5 ≤	NAO	< 1.5
NAO++	strongly positive	1.5 ≤	NAO	

Table 3.2: Definition of the NAO phases (compare Pinto et al. (2008)).

study the influence of the NAO on winter storm frequencies, track density composites for the different NAO phases are calculated (for the details of track density calculation consider Section 2.3). The composites are calculated by considering the winter seasons (October through March) for which a seasonal NAO index according to the NAO phase definitions in Table 3.2 is identified. Based on ERA-Interim for the period 1979-2010, resulting track density composites for the different NAO phase are shown in Figure 3.7 (left). It should be noted that only one winter season occurred with NAO−− (season 2009/2010) and NAO++ (season 1988/1989) phase, which is why resulting track density composites for these phases are not representative. Comparing to the climatological mean track density as indicated by black contour lines, it can be found that in the positive phase (NAO+), the track density pattern is similar to the climatology with respectively higher values particularly in the areas of highest track density. In the negative phase (NAO–), distinctive differences are found in the track density pattern, with considerably lower values especially over the eastern Atlantic and Europe. In terms of absolute differences between composites and climatology as shown in Figure 3.8 (left), very similar patterns are found for NAO– and NAO+ phase, with an opposite sign. While in the negative phase, winter storm frequencies are found to be reduced by about 2-2.5 events per year over a large area covering the British isles, the Northern sea and the Baltic regions, frequencies are increased by the same amount in the positive phase. Similar analysis can be done on the basis of GCM model output as described in Section 3.2.2. For that, the 8 individual GCM simulations for recent climate conditions are evaluated, considering the period 1861-2000. NAO patterns are assessed as described above to derive the NAO index as the principle component loadings. Resulting track density composites with respect to the different NAO phases are then calculated as previously for the reanalysis data, however based on a much larger data base (140 years for each model simulation vs. 32 years for ERA-Interim). Track density composites can be considered for the ensemble mean, by averaging the composites of the single model simulations. The characteristic dependence of the track density on the NAO phase shown in Figure 3.7 (right column) is found to be rather similar to the dependence identified in historical reanalysis data. Besides composites being much smoother due to the larger sample sizes, the NAO dependence is clearly represented by a meridional shift in the location of maximum track densities. While in negative NAO phases track densities are increased at lower latitudes and reduced at higher latitudes, the inverse picture is found in positive NAO phases. Particularly in the NAO++ phase it becomes obvious that this northward shift is accompanied by strongly increased track densities over the British Isles and Scandinavia. In terms of absolute differences to climatological track densities, the patterns for the negative and positive NAO phase (as shown in Figure 3.8 (right) are again found to be similar with opposite signs with track densities being enhanced over northern Europe in the positive phase by

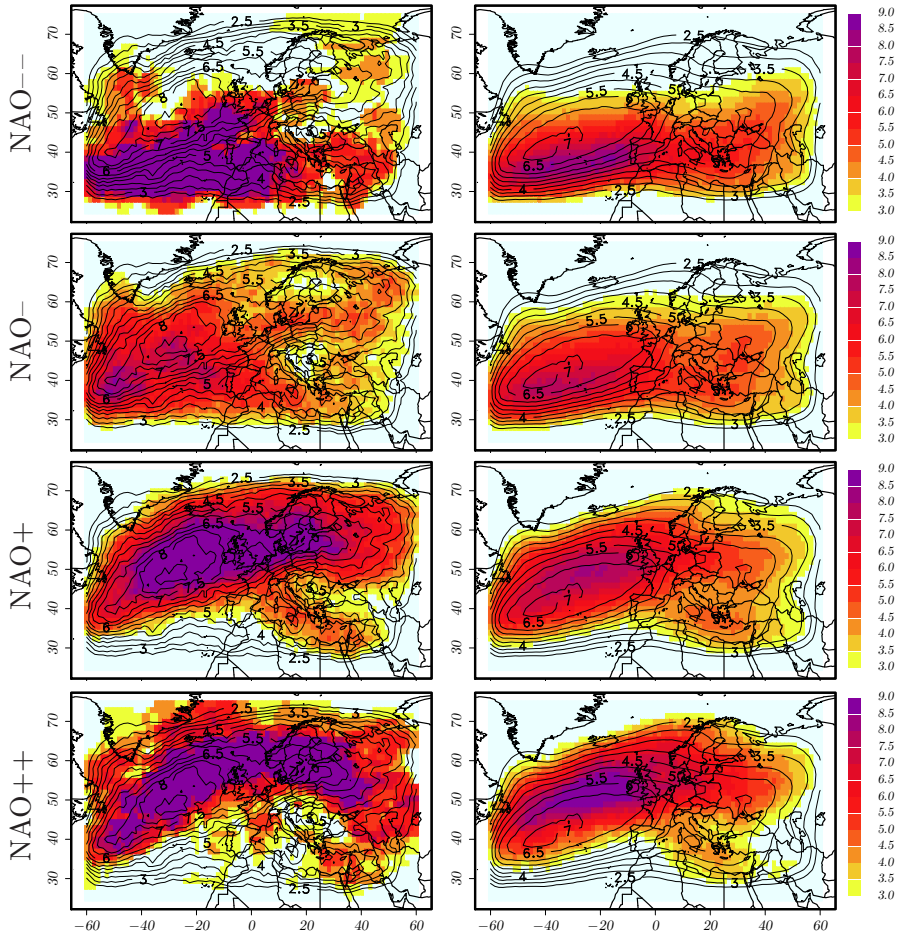

Figure 3.7: (a) Track density composites (in units of tracks per year) for the different NAO phases, with black isolines indicating the climatological track density. (left) ERA-Interim track density composites (1971-2010). (right) Ensemble averaged track density composites from the 8 GCM simulations (1860-2000).

about 0.5 to 1.5, while reduced by about 0.5 to 1.3 in the negative phase.

3.5.2 Dependence of Storm Damages on the NAO Phase

Similar to the analysis of track density dependence, the dependence of losses occurring in Germany on the NAO phase can be assessed. Stratified by the NAO index (calculated on a monthly basis) the distribution of daily germanwide loss ratios are shown in Figure 3.9. An interesting result is, that the top 5 winter storm events with respect to losses distribute over all 5 NAO phases. Kyrill, which caused the highest German wide loss ratio on the 18th of January 2007 for which a NAO index of 1.7 (NAO++) is diagnosed. In contrast, Xynthia in February 2010 caused the 5th highest daily loss and occurred in the strongly

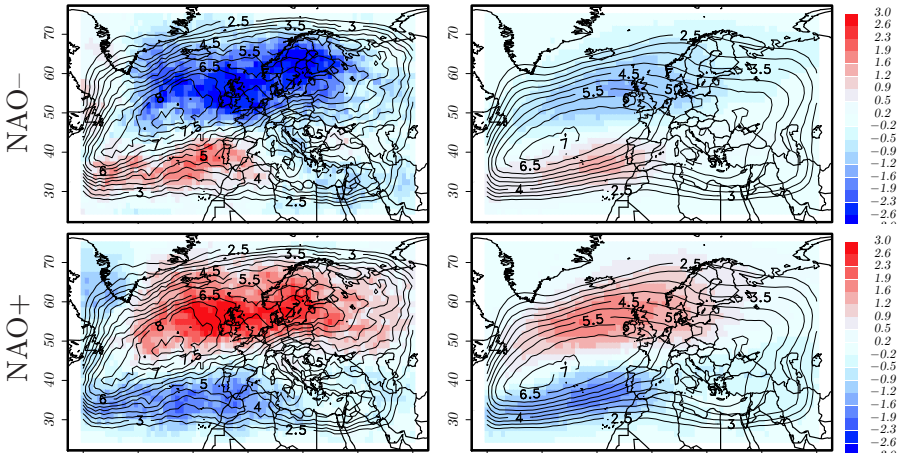

Figure 3.8: Differences of track density composites to the climatological track density. (left) Based on ERA-Interim (1979-2010). (right) Ensemble averaged composite differences from the 8 GCM simulations (1860-2000).

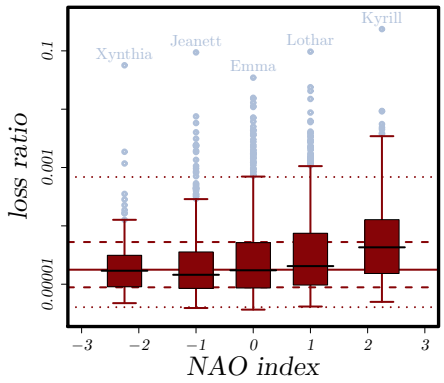

Figure 3.9: Distribution of daily German wide loss ratio (in ‰) stratified by the NAO phase. Box-whisker plots indicate 5%, 25%, 50%, 75% and 95% quantiles of daily loss ratio. Horizontal lines depict the corresponding quantiles based on the full distribution of daily loss ratio.

negative NAO phase (NAO−−) with a NAO index of -2.6. Except for the strongly negative NAO phase, Xynthia's genesis, development and it's southwest-northeast path across Iberia, France and central Europe were generally very uncommon (Liberato et al., 2013), including an explosive intensification supported by moisture located over an elongated region of the subtropical North Atlantic Ocean with anomalously high SST. However, considering the general characteristics of the loss distribution within the NAO phases by calculating different quantiles of loss (Figure 3.9), distinct differences in the distribution of daily losses can be identified depending on the NAO phase. While for the indifferent NAO phase the distribution compares well to the climatological distribution (as indicated

by horizontal lines) quantiles of losses are considerably reduced (increased) in the negative (positive) NAO phases. This holds particularly for the high quantiles (75% and 95%) with the dependence being stronger the higher the quantile considered. It can be followed that, compared to the negative or indifferent phases of the NAO, particularly the severe winter storm events (causing high losses) are favored in the positive NAO phases. Counting the

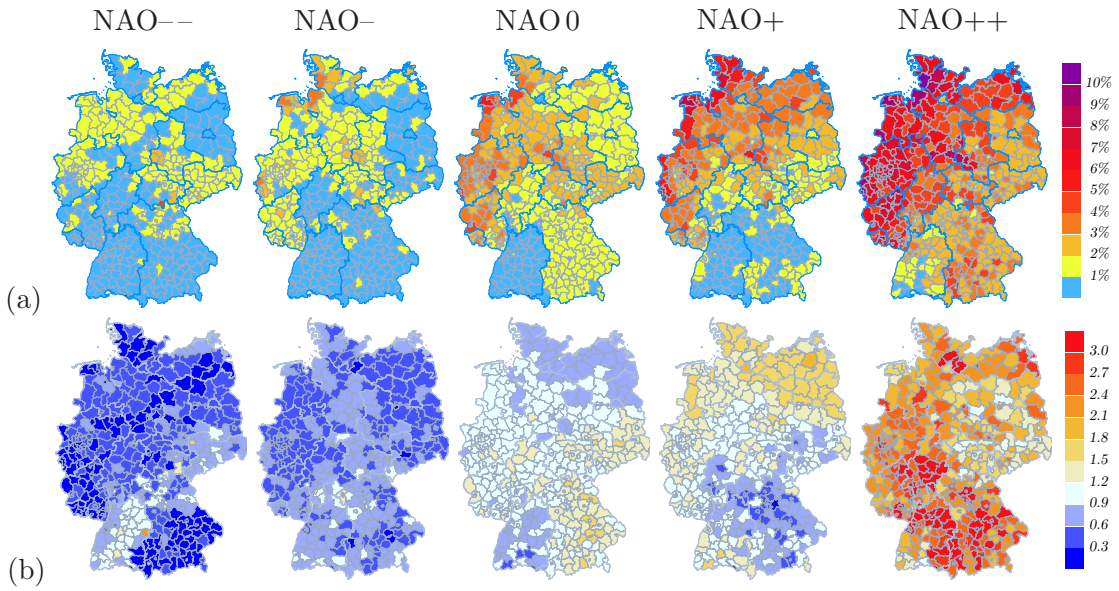

Figure 3.10: (top row) Occurrence probability of days with a loss ratio > 0.002‰ for the different NAO phases. (bottom row) Occurrence probabilities normalized on the climatological occurrence probability (p/p_{clim}).

number of days with an exceedance of the loss ratio above 0.002‰ (corresponding roughly to the 98th percentile of daily losses) the NAO dependence can be assessed for each individual district. For each NAO phase, the number of threshold exceedances is counted to calculate the probability of a loss day as shown in Figure 3.10 (top row). As for German wide loss ratios, a strong dependence on the NAO phase can be diagnosed. Probabilities for a day with a loss ratio above 0.002 are found to vary between 0% and 2% in the NAO– – phase with continuously increasing probabilities in NAO–, NAO 0, NAO+ and NAO++ phase. Under NAO++ conditions, exceedance probabilities are found to raise to about 5% to 6% in the majority of districts and probabilities even raising up to 10% in coastal regions as well as in the outermost west of Germany. Since exceedance probabilities are generally higher in the north-west of Germany, the factor by which the occurrence probability is increased/decreased (when comparing to the climatological occurrence probability) is shown in Figure 3.10 (bottom row). It is found, that probabilities are reduced by about a factor of 4 under strongly negative NAO conditions, while being increased by a factor up to 3 under strongly positive NAO conditions.

3.6 Tropical Origins of Changes in the North Atlantic Oscillation

3.6.1 Assessment of Hadley Circulation Changes

The large scale circulation of the atmosphere, forced by a surplus of net radiation in equatorial regions and a deficit in polar regions, can be described in simple 3 cell model illustrated in Figure 3.1. It features the Hadley Cell (HC) as a large scale circulation cell with warm air rising near the equator being transported poleward in high altitudes. Cooling down the air sinks at around 30°N leading to a very stable high pressure belt in these latitudes. Similarly but less intense, the polar cell (PC) includes rising air at around 60°N and sinking air in polar regions, which analogously leads to a stable low pressure system around 60 °N. The mid-latitudes (called Ferrel cell in the 3 cell model) are predominantly influenced by these 2 pressure belts at 30°N and 60°N. As proposed by Oort and Yienger (1996) and Mitas and Clement (2005), the structure of the HC can be assessed by the zonal mean of the stream function for the mean poleward flow as shown in Figure 3.11 (left). The stream function is calculated on the basis of the 3 run ensemble of ECHAM5-MPIOM for DJF for the period 1971-2000 (20C). The HC can be clearly identified extending from about 15°S to 30°N and vertically reaching up to a height corresponding to a pressure level of 100hPa. A maximum of about $19 \cdot 10^{10} kgs^{-1}$ is identified at about 5°N and in a height of 600hPa in good agreement to the the characteristics derived from observations and reanalyses Oort and Yienger (1996); Mitas and Clement (2005). Similarly, stream function is calculated for the period 2071-2100 of the scenario simulations with differences in the ensemble mean stream function between the SRES-A1B and the 20C period shown in 3.11 (right). Areas in which an increase in the stream function is found are shown as red isolines and can be identified mainly close to the Hadley cell's poleward and upward bounds with increases reaching about $19 \cdot 10^{10} kgs^{-1}$. Areas with decreasing values in the stream function as shown in blue contours are identified close to the southern bound of the (Northern Hemisphere) Hadley cell as well as in the vicinity of its center. These changes in the stream function can be interpreted as a poleward shift of the northern branch of the Hadley cell together with a slight decrease in it's intensity with similar results being identified for the southern branch of the HC considering southern hemisphere winter (not shown). These findings are in agreement with recent studies (Lu et al., 2007) finding a weakening as well as a poleward expansion of the Hadley circulation in climate change simulations which they attribute to an increase in the subtropical static stability, pushing poleward the baroclinic instability zone and the poleward boundary of the HC. This is consistent with the results with respect to changes in the zonal mean Eady growth rate (compare Figure 3.4), where an intensification and poleward shift as well as an upward expansion of the baroclinic instability zone has been

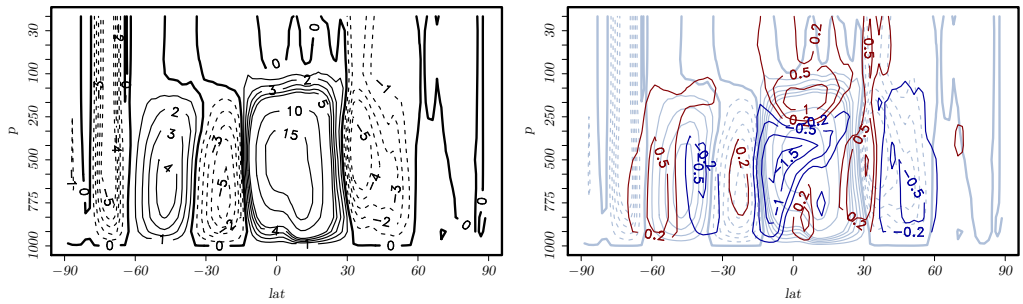

Figure 3.11: (left) Ensemble averaged zonal mean stream function (in $10^{10} kgs^{-1}$) for December-February of 1971-2000 under recent climate conditions, derived from the MPI-ECHAM5 ensemble. (right) Changes in the zonal mean stream function in 2071-2100 under SRES-A1B conditions, compared to 1971-2000. Red and blue contours indicate increases and decreases, respectively.

identified in the SRES-A1B scenario simulations. The assessment of the zonally averaged zonal winds reveal that the resulting changes in baroclinicity in the mid-latitude upper troposphere are accompanied by a consistent shift and an intensification of the jet streams. Figure 3.12 shows the long term mean of (zonally averaged) zonal winds for the period 1971-2000 (20C, green), featuring an area of strong westerlies of up to 40 m/s in a height of 200hPa and stretching over the mid-latitudes. These westerlies represent the jet streams, namely the polar front jet and the subtropical jet which - due to the rather large variations with respect to their location- are not distinguishable in the long term mean considered here. Changes in the mid-latitude westerlies are found to be strengthened, as indicated by the red contours in 3.12, representing the differences in mean zonal winds for SRES-A1B minus 20C. Furthermore, consistent to the poleward shift and upward expansion of the baroclinic instability zone the jet streams can be found to be pushed pole- and up- ward.

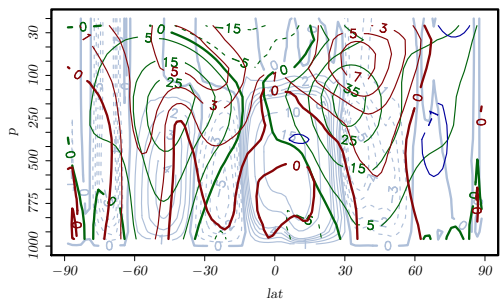

Figure 3.12: Long term averaged zonal wind speed in m/s under recent climate conditions as derived from MPI-ECHAM5 (green). Differences in zonal winds derived for 2071-2100 under SRES-A1B conditions are shown as red isolines.

3.6.2 The Influence of the Hadley Circulation on the NAO

The dynamic relation between the Hadley cell characteristics and the NAO shall be analyzed in the following. To do so, the Hadley cell is characterized by means of a Hadley cell strength index (Oort and Yienger, 1996) and in terms of it's poleward extend as proposed by Lu et al. (2007). Hadley cell strength index (HCI) is characterized using the zonal mean stream function $\psi(\phi, p)$ the HCI being the maximum value of $\psi(\phi, p)$, which can be calculated for each DJF season. As the northward bound of the HC, Lu et al. (2007) identify the first latitude in poleward direction at which the stream function in 500hPa height ($\psi_{500}(\phi)$) becomes zero. However, since the resolution of ECHAM5-MPIOM is rather low with a resolution of 1.875°, small displacements in the HC extend might be missed. Thus roots of $\psi_{500}(\phi)$ are estimated by linearly interpolating between the last latitude with $\psi_{500} > 0$ and the first latitude with $\psi_{500} < 0$ to gain ϕ_0 with $\psi_{500}(\phi_0) = 0$. As the Hadley cell strength index, ϕ_0 is estimated separately for each DJF season to gain yearly time series.

In a first step, the obtained time series, calculated from the ECHAM5-MPIOM simulations consisting of 3 model simulations, are related to the corresponding NAO index time series. For that, both HCI as well as ϕ_0 are standardized so that a mean of zero and standard deviation of 1 is obtained in the period 1971-2000. The scatterplot of resulting standardized HCI values and the NAO index (calculated for DJF, compare Sections 3.2.3 and 3.3.2) for the years 1861-2000 of the 20C simulations are shown in Figure 3.13, with a non significant correlation of 0.04 being found. For the future period 2071-2100 under the 3 considered emission gas scenarios, means of NAO index values were identified to strongly increase (compare Table 3.1), with insignificant decreases in the respective means of the HCI in these periods (as indicated in colored points in Figure 3.13). Thus no relation between Hadley cell strength and the NAO index can be identified providing an explanation of diagnosed NAO changes. However, considering the relation between ϕ_0 calculated for the DJF months and the DJF NAO index (Figure 3.13, right), a significant correlation of 0.43 is identified. As done for the HCI, the corresponding means diagnosed in the future climate periods 2071-2100 are shown in colored points in Figure 3.13 (right). The increases in the NAO strength in the scenario simulations can be found to be well described by the relationship identified on the basis of yearly values in the period 1861-2000, with a nearly linear relation between the identified long term shifts in ϕ_0 and the long term changes in the NAO index. Hence, a shift in ϕ_0 by 1 standard deviation with respect to it's recent climate variability, leads to a mean increase of the NAO index of about 0.4 which is well aligned with the diagnosed long term changes. Same analysis can be performed for ERA-Interim, however data basis being much smaller (compare Figure A.5 of the Supplementary Material). Even though associated with larger uncertainties, the dependence of NAO strength on the northward extent of the HC is found well comparable.

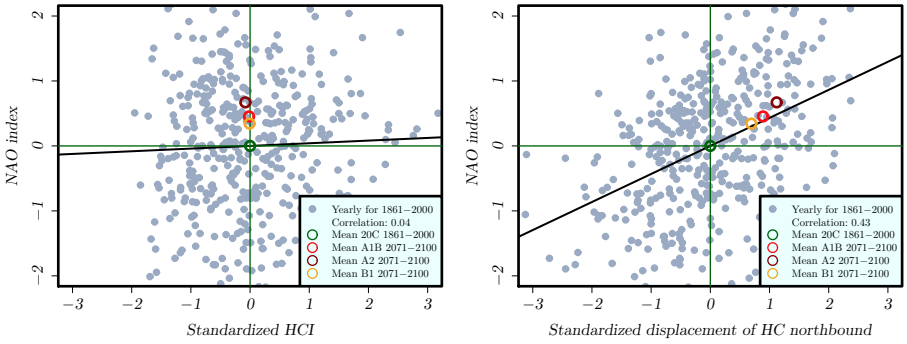

Figure 3.13: Dependence of the NAO index on the standardized Hadley cell strength index (left) and on the standardized displacement of the Hadley cell's northward boundary (right). Grey dots show the respective values calculated for each winter season (DJF) of the period 1861-2000, for each of the 3 MPI-ECHAM5 model simulations individually. Colored circles show 30 year ensemble means for the 20C period (green) as well as the future period 2071-2100 under SRES-B1 (yellow), SRES-A1B (red) and SRES-A2 (darkred).

In a second step, the changes in the shape of the NAO, as discussed in Section 3.3.3, shall be related to the diagnosed to the changes in the Hadley circulation characteristics. Since a strong influence of the displacement of the northbound of the HC on the NAO index was found, it stands to reason that these changes might also be related to the changes in the NAO's shape. To investigate on this relation different sets, consisting of 30 or more winter seasons each, are selected from the recent climate simulations of ECHAM5-MPIOM, available for 140 years (1861-2000) for each of the 3 model runs. Firstly the selection can be made by choosing those winter seasons (DJF) in which the location of HC bound ϕ_0 lies within the 1st, 2nd or 3rd tertile of the distribution of ϕ_0. For each set, consisting of 46 years, principle component analysis is performed to derive the NAO pattern as the leading EOF shown in Figure 3.14. NAO patterns are found to differ considerably for these three sets with action centers being modified distinctively with varying location of ϕ_0. In case of the Hadley cell extending far north, an eastward shift in the southern action center is found (red) compared to the case of "normal" extend of the HC (grey). The opposite is found under conditions featuring a retreat of HC northbound (blue). Similarly, however less clear, an influence of the Hadley cell extent on the northern action center can be identified, including an enlarged eastward extension in the case of a northward displacement of the HC northbound. To analyze, whether the magnitude of this eastward shift due to the dependence on the HC extent can account for the diagnosed changes in the climate projections, an alternative set of winter seasons (DJF) are sampled from the recent climate simulations (1861-2000) representing the distribution of HC extent within the future period 2071-2100. For each of the 30 values for ϕ_0 in the

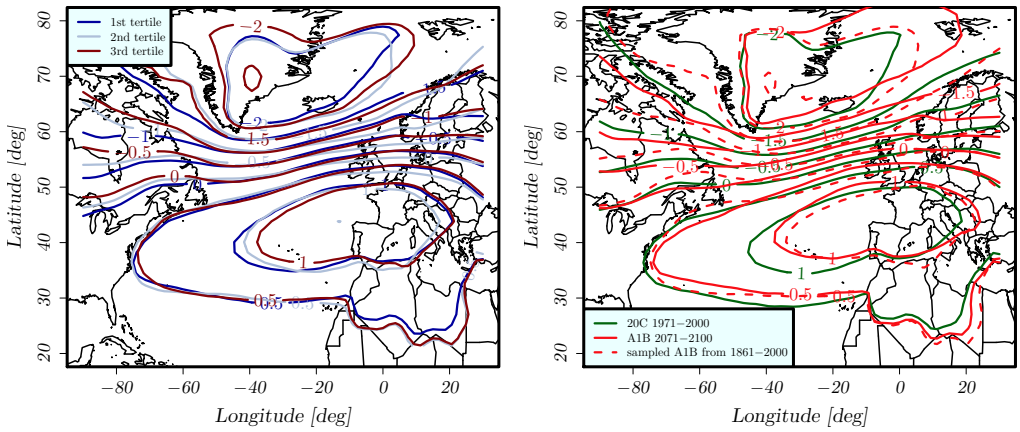

Figure 3.14: (left) NAO pattern derived from the years corresponding to the 1st (blue), 2nd (grey) and 3rd (red) tertile of the distribution for the northward extent of the Hadley cell. (right) NAO pattern as derived from a sample of years representing the future distribution for the northward extent of the Hadley cell (dashed lines) in comparison to the diagnosed NAO patterns as derived from the future climate period directly. All results are shown in terms of the ensemble average for the three MPI-ECHAM5 runs.

future climate period 2071-2100, the season from the 20C period is chosen having a value for ϕ_0 being closest to this value. Since variations in the HC extent are rather large in 20C, the future distribution of ϕ_0 can be well described by this sample. As before the NAO pattern is determined from principle component analysis for this set of 30 years. If can be found, that the NAO pattern diagnosed is similar to the diagnosed NAO pattern derived from the future climate simulation (Figure 3.14, right). In particular, the eastward shift of the southern action center is well represented in this way. The eastward expansion of the northern action center can be clearly identified, however not as strongly as identified within the climate projections. Considering additionally the climate projections following the SRES-A2 and the SRES-B1 scenario, the northern action center however is found to undergo less distinct changes including a less pronounced eastward expansion in comparison to the SRES-A1B projections. Similarly sampling the distribution of ϕ_0 according to the corresponding future climate distributions for SRES-A2 and SRES-B1, the "sampled NAO patterns" are again found in good agreement, particularly with respect to the shape and location of the southern action center (Figure A.6 of the Supplementary Material). The shape of the northern action center which is evidently subjected to larger variations thus seems to be described worse through the influence of the Hadley cell dynamics.

It can be concluded from the analysis presented in this section that a strong influence of the Hadley cell's northward extent exists on both NAO strength as well as the shape of the NAO pattern, which has been shown to be a dynamical effect describing much of the year to year variability of the NAO. A Hadley cell expansion towards the north has

been related to a shift towards more positive NAO phases. Furthermore, particularly the southern action center is found to be considerably shifted eastward under such conditions, the northern center being less affected however also showing an eastward expansion.

In the following, the dynamic mechanism underlying this relation shall be further highlighted. For that, composites of the zonal mean baroclinicity as well as the mean zonal winds are considered for (a) strongly retreated Hadley cell extend ϕ_0 $--\rightarrow$ with normalized $\phi_0 < -1.5$ and (b) strongly extended Hadley cell ϕ_0 $++\rightarrow$ with normalized $\phi_0 > 1.5$ (Figure 3.15). As expected, the Hadley cell can be found pushing forward the baroclinic instability zone, identified by a dipole like structure in the EGR composite for ϕ_0 $++$, with decreased baroclinicity in the subtropical troposphere and increased baroclinicity in the mid-latitudes at about 50°N (Figure 3.15, lower left). Consistently for ϕ_0 $--$, an inversed pattern is diagnosed (Figure 3.15, upper left). Related to these shifts in the baroclinic instability zone, jet streams are consistently modified with respect to their location (Figure 3.15, right), the westerlies in the upper troposphere being shifted northward (southward) related to ϕ_0 $++$ (ϕ_0 $--$) conditions. The dependence of the

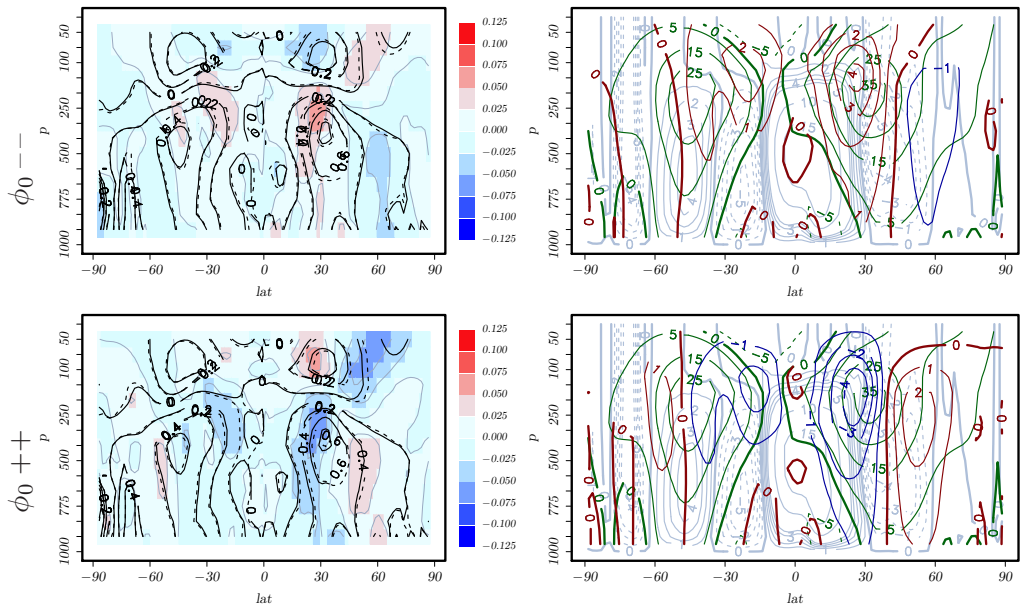

Figure 3.15: Zonal mean Eady growth rate anomalies (σ_{BI} in units of day^{-1}) (left panel) and mean zonal wind anomalies in m/s (right panel) for strongly retreated HC northbound (ϕ_0 $--$, top) and strongly advanced HC northbound (ϕ_0 $--$, bottom).

baroclinicity in the mid-latitudes on the HC extent resemble to a certain extent to the projected climate change signals analyzed in Section 3.4. This concerns the dipole structure representing a poleward shift of the baroclinic instability zone which compares to the change signal as shown in Figure 3.4 (right). However, projected EGR features additional

fundamental changes, namely a dipole structure of decreasing baroclinicity in the polar lower troposphere and increasing baroclinicity in the polar upper troposphere. As discussed in Section 3.4 this structure can be to a large part related to an enhanced warming of the polar lower troposphere, which in turn can be attributed to positive ice-albedo feedback (Johannessen et al., 2004), a feedback that has proven to be a robust feature of MPI-ECHAM5 (Bengtsson et al., 2004). Resulting changes in baroclinicity patterns can thus be attributed to a combined effect with dynamical parts related to the dynamics of the Hadley cell and an effect due to the warming of tropical lower troposphere which can be assumed to occur on much longer timescales. The identified dynamical influence of the Hadley cell dynamics and the resulting impacts of a modulated NAO on the climate over Europe, taking into account the influences of the tropical circulation may however be of great importance, particularly with respect to seasonal or decadal predictions.

3.6.3 A Rossby Wave Interpretation of the NAO

Due to the conservation of potential vorticity (PV), it can be shown that a flow over an orographic barrier induces a stationary Rossby wave in the lee of such barrier (compare e.g. Chapter 4.3 of Holton (2004)). It can be argued, that the southern action center forming the Azores high is in fact a manifestation of the ridge of such Rossby wave (as depicted schematically in Figure 3.16). It shall be investigated in the following, in how far such Rossby wave interpretation of the NAO can provide a theoretical interpretation to the diagnosed changes of the NAO shape, specifically the eastward shift of its action centers.

In an isothermal atmosphere, the curvature radius R_s of the lee through of such a stationary Rossby wave can be shown (Névir, 2014; pers. comm.) to depend on the height of the orographic barrier h_B and the over topping velocity v_h according to

$$R_s = \frac{v_h}{f \cdot \left(e^{-h_B/H_0} - 1\right)}, \tag{3.3}$$

with typical values for the Coriolis frequency f being $10^{-4} s^{-1}$ in the mid-latitudes and the scale height of the homogeneous atmosphere H_0 being approximately 8 km. The lee wave trough as depicted in Figure 3.16 is followed by a ridge which shall be associated with the Azores high in the following. Assuming a sine wave $f(x) = -A \cdot cos(\frac{20\pi}{\lambda} \cdot x)$ with amplitude A (in km) and wave length λ (in km) to describe the stationary Rossby wave with its trough being located at $x_0 = 0$ the determination of the curvature radius at x_0 leads to

$$R_s(x_0) = \frac{\lambda^2}{4\pi^2 \cdot A}. \tag{3.4}$$

Solving for the wave length λ, the dependence on v_h is described by

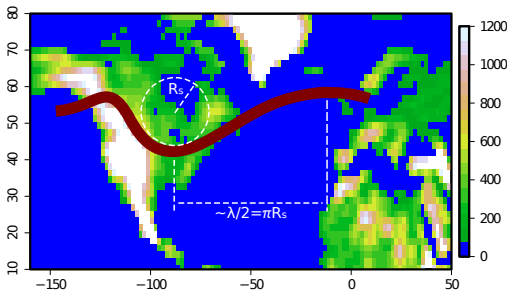

Figure 3.16: Sketch of an orography induced stationary Rossby wave (see text for explanations) with the underlying topography as represented in MPI-ECHAM5.

$$\lambda(v_h) = 2\pi \cdot \sqrt{A(v_h)}\sqrt{R_s(v_h)}. \tag{3.5}$$

To describe the displacement D of the southern NAO action center (corresponding to the location of the ridge) in case of a change in the wave length $\lambda(v_h)$ can be written as

$$D = c_0 \cdot \Delta\lambda = c_0 \cdot \frac{\delta\lambda}{\delta v_h} \cdot \Delta v_h, \tag{3.6}$$

with c_0 corresponding to 3/4 assuming that the distance of the rocky mountains to the location of the Azores high accounts for 3/4th of the wave length (compare Figure 3.16). Assuming further, that the amplitude A of the Rossby wave is independent of v_h leads to

$$D = \frac{c_0\pi\sqrt{A}}{\sqrt{v_h} \cdot \sqrt{f \cdot \left(e^{-h_B/H_0} - 1\right)}} \cdot \Delta v_h. \tag{3.7}$$

Re-substituting A using Equation 3.4 leads to

$$D = c_0\pi \frac{\sqrt{\frac{\lambda^2 \cdot f \cdot \left(e^{-h_B/H_0} - 1\right)}{4\pi^2 \cdot v_h}}}{\sqrt{v_h} \cdot \sqrt{f \cdot \left(e^{-h_B/H_0} - 1\right)}} \cdot \Delta v_h = \frac{c_0\lambda}{2 \cdot v_h} \cdot \Delta v_h = d \cdot \Delta v_h, \tag{3.8}$$

with d in units of km per m/s being the displacement coefficient to relate the anomaly in zonal winds (Δv_h) to the Displacement D of the Azores high. By construction $c_0\lambda$ corresponds to the distance between the location of the Rock mountains and the location of the Azores high which can be roughly estimated to about 7000 km. To include the uncertainty about this estimate, a range between 6000 and 8000 km is asssumed. Empirically, the dependence of the displacement of the Azores high from the westerly over topping flow of the Rocky Mountains is analyzed in the following. For that, principle component analysis is performed as described in Sections 3.2.3 and 3.3.3 on the basis of ECHAM5-MPIOM. For each of the 3 simulations and for a 30 year running window over

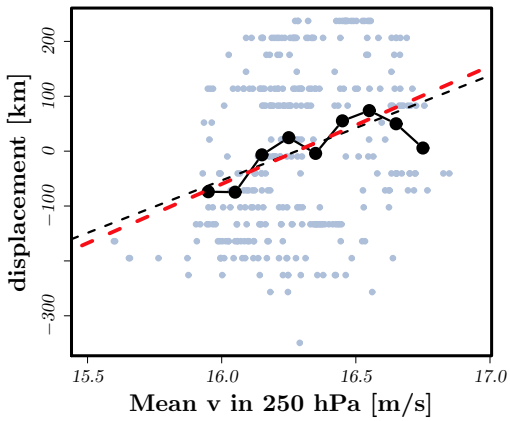

Figure 3.17: Empirical determination of the displacement coefficient d in units of km per m/s. The displacement coefficient is determined from a linear fit (shown in black) between the zonal wind speed in 250hPa height averaged from 40°N to 70°N and the longitudinal location of the Azores height determined from the NAO pattern. NAO patterns are calculated for 30 year running windows, and zonal winds are averaged over 30 years correspondingly. Theoretical dependence of D is depicted as a red line.

the period 1861-2000, NAO patterns are derived individually, resulting in a set of 330 representations of the NAO pattern. From each pattern, the longitude of the southern action center is located by searching for the maximum in the EOF field. This location is converted into a displacement D (in km) by calculating the longitudinal distance to the mean location of the southern action center. Similarly, the temporal and zonal mean of the westerly winds in different height layers are calculated for the respective 30 year running window periods, averaging furthermore from $40°N$ to $70°N$.

The mean zonal wind in different heights can finally be correlated to the displacement of the Azores high, determining the empirical coefficient d given in km per m/s. Results of this procedure are shown in Figure 3.18 in black with error bars on d determined from the linear fit procedure. The theoretical estimate as given by Equation 3.8 with $c_0\lambda = 7000$ km is shown as the red curve. Since v_h depends on the height, a functional dependence of the coefficient d is found with well agreement of theoretical and empirically determined coefficient d in a height of about $100hPa$ to $200hPa$, close to the height levels in which the jet streams are found (compare Figure 3.12). Same analysis can be performed analysing zonal wind velocity averaged over $10hPa$ and $800hPa$ height, with results being indicated as horizontal lines in Figure 3.18. Theoretical estimate of d in this case is found to be 247 km per m/s, with the empirically estimated value value of 278 km per m/s (with an uncertainty range between 233 and 322 km per m/s) being in good agreement. Thus, it has been shown that the displacement of the NAO action center is closely related to the over topping zonal winds above the Rocky Mountains and

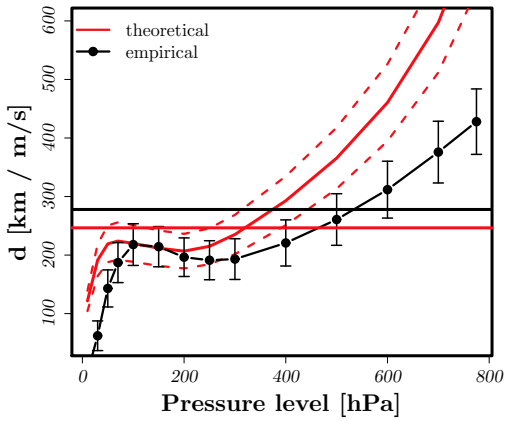

Figure 3.18: Comparison between the empirically determined displacement coefficient d in units of km per m/s to the theoretical estimate, considering zonal wind speeds on different pressure levels (see text). Uncertainties on empirical estimates (black bars) are determined from the fit procedure, while uncertainty on theoretical estimates (red dashed lines) are calculated using 6000 and 8000 km as the lower and upper bounds for $c_0\lambda$ in Formula 3.8.

furthermore that simplified theoretical considerations of the lee wave, induced by such orographic barrier, can describe this dependence quantitatively. This gives raise to the hypothesis, that to a large extend variability in the NAO may be induced by changes in the zonal flow of the mid-latitude upper troposphere, which has been shown to be related to variations in the northward extent of the Hadley circulation, accompanied by a poleward shift of the baroclinic instability zone.

3.7 Summary and Discussion

In the present chapter, possible mechanisms underlying the projected changes in the European winter storm climate (Chapter 2) and resulting impacts in Germany (Chapter 4) were investigated.

Governing much of European weather variability, the North-Atlantic-Oscillation (Walker and Bliss, 1932) has been addressed, analyzing in how far the NAO might change with respect to it's phase as well as it's shape under future climate conditions. The NAO was found to shift towards more positive phases, identified consistently amongst an ensemble of GCM model projections under SRES-A1B conditions. This tendency towards a more positive NAO phase, accounting for an increase of about 0.7 standard deviations of the distribution of recent winter mean NAO, is in good agreement with previous studies (Ulbrich and Christoph, 1999; Stephenson et al., 2006). Stephenson et al. (2006) analyze an ensemble of model projections assuming a 1% increase in CO_2 concentrations per year and identify a shift of about 0.18 standard deviations in the probability distribution of winter mean NAO. These increases are considerably smaller than the changes identified in the present study, however emission gas concentrations according to the SRES scenarios have been considered which are not directly comparable to assumed CO_2 changes in Stephenson et al. (2006). Furthermore, as also discussed by Stephenson et al. (2006), the magnitude of the NAO response to increased greenhouse gas concentrations can be found to be highly model-dependent leading to large uncertainty in multi-model estimates of diagnosed NAO trends. Additionally the pattern of the NAO was found to undergo distinct changes including a northeastward shift of its action centers, distinctively identified particularly for the southern action center. These shifts with respect to the NAO's action centers are consistently diagnosed for different GCM projections from the multi model ensemble and have been identified in future climate projections previously (Ulbrich and Christoph, 1999).

Investigation of baroclinicity in terms of the Eady Growth Rate showed that according to projections with ECHAM5-MPIOM a pronounced northward shift and upward expansion of the baroclinic instability zone occurs. This is indicated by a dipole like structure in the zonal mean EGR with decreasing EGR in the subtropical troposphere and strong increases throughout the upper troposphere of the mid-latitudes, which can be related to an enhanced warming which occurs in the tropical upper troposphere. The enhanced warming of the lower polar troposphere combined with slight temperature decreases in the upper polar troposphere, which can be related to positive arctic sea ice-albedo feedbacks (Johannessen et al., 2004; Bengtsson et al., 2004) are further enhancing tropospheric temperature gradients over the mid-latitudes. In low altitudes however, the strong warming of the north-polar region leads to a decrease in meridional temperature gradients which

manifests in decreases of zonal mean EGR. Assessing changes in the spatial patterns of North-Atlantic EGR of the upper troposphere revealed a distinct expansion of the baroclinic instability zone over the North Atlantic, including pronounced increases of EGR particularly over the Eastern Atlantic and Europe which is in line with previous findings (Lunkeit et al., 1996; Ulbrich and Christoph, 1999).

The NAO and it's substantial influence on European weather has been widely studied in the past (for an overview compare e.g. Wanner et al. (2001)). With respect to European winter storms related to extreme cyclones, a strong relation between the positive NAO phase and suitable environmental cyclone growth factors over the North Atlantic (Pinto et al., 2008) leading to an increased storminess in Northern and Central parts of Europe (Wang et al., 2009; Donat et al., 2010a) with an opposing dependency (namely decreased storminess) for the Mediterranean and Southern Europe (Nissen et al., 2010; Wang et al., 2011). The occurrence of large scale winter storm events identified using an objective tracking algorithm (Leckebusch et al., 2008) were investigated with respect their dependence on the NAO phase, identifying a northward (southward) shift in the typical storm paths under positive (negative) NAO phases well aligned with results by Wang et al. (2011). Furthermore, in the positive NAO phase, tracks of wind storm events are identified reaching further east, leading to particularly strong increases in winter storm frequencies over the British Isles and the Baltic regions. These findings are in good agreement with results by Pinto et al. (2008) identifying that in positive NAO phases, the enhancement of suitable growth conditions leads to enhanced frequencies (and increased intensities) of extreme cyclones on the typical paths of cyclone activity over the Northern Atlantic across the North of the British isles and reaching Scandinavia. The relevance of the phase of the NAO has been further demonstrated in terms of the occurrence of storm losses in Germany. Historical severe winter storm events causing widespread damages are found not to be restricted to the positive NAO phases, with storm Emma having occurred even in a strongly negative NAO phase. However, the distribution of loss events are found to be distinctively altered by the NAO phase, with particularly the high quantiles of the distribution of daily losses being increased under positive NAO conditions. This means, that the positive NAO phase can be related to an increased frequency of severe storm events causing widespread damages over Germany. Considering loss events (fixed threshold exceedances) on district level, frequencies of such events are found to vary between 0% and 2% in the NAO−− and between 5% and 10% under NAO++ conditions. Compared to the long term average frequencies, the probabilities for the occurrence of losses are reduced by about a factor of about 4 under strongly negative NAO conditions, while being increased by a factor up to 3 under strongly positive NAO conditions.

With respect to the origins of the low-frequency variations and long term changes in the NAO as projected for future climate conditions, the influence of the tropical circulation

has been investigated. It is found, that the dynamics of the Hadley cell play a major role for the diagnosed variability of the winter mean NAO. More precisely a northward expansion of the Hadley cell's poleward boundary is found being related to more positive NAO phases. At the same time, such expansion is found to influence the NAO pattern itself leading to northeastward shifts of the NAO action centers, particularly distinctively identified for the Azores high. Furthermore it was found, that the northward expansion of the HC bound is related to a northward shift of the baroclinic instability zone over the mid-latitudes which is in agreement with findings of Lu et al. (2007). These changes in mid-latitude baroclinicity were furthermore found to be accompanied by a northward shift in the location of the westerly jets, which are found to be increased over the mid-latitudes and decreased over the subtropics. Theoretical considerations on the lee wave trough of a stationary Rossby wave induced by the westerly flow over the Rocky Mountains were found to be in good agreement to a dependence found for the displacement of the southern action center on the westerly flow in the upper troposphere. This gives raise to the hypothesis that the NAO might be interpreted as a manifestation of such stationary Rossby wave induced through the orographic barrier posed by the Rocky Mountains, with direct influences on long-term variations in the NAO.

Climate projections using ECHAM5-MPIOM indicated, that the Hadley cell is expanding poleward with slight decreases in terms of it's intensity, well aligned with findings of Lu et al. (2007). The baroclinic instability zone is found to be pushed northwards consistently to the dynamic relation discussed above. Furthermore, the baroclinic instability zone is intensifying and expanding upward in agreement with results of Yin (2005) showing that this is related to a consistent pole- and up- ward shift including an intensification of the corresponding storm tracks. The dynamic relation between the Hadley cell and mid-latitude baroclinicity showed that the future changes diagnosed for the baroclinicity are consistent with the northward expansion of the Hadley cell in the scenario simulations. However, projected baroclinicity changes feature additional changes, namely a dipole like structure of decreasing baroclinicity in the polar lower troposphere and increasing baroclinicity in the polar upper troposphere. This can be related to an enhanced warming of the polar lower troposphere (related to a positive ice-albedo feedback (Johannessen et al., 2004)), leading to decreased baroclinicity in the mid-latitude lower troposphere, and a slight decrease in temperatures of the polar upper troposphere leading in turn to increased baroclinicity over the mid-latitudes upper troposphere.

It should be noted, that the identified relation between the Hadley cell extent and the NAO as well as it's relation to mid-latitude baroclinicity and diagnosed changes in the occurrence of European winter storms can not be clearly separated with respect to which is cause and which is consequence. However, the considerations presented in this chapter drew a consistent picture of the complex chain of mechanisms involved when considering

future projections of a warmer climate and the diagnosis of changes in European winter storm climate. As results by Hoerling et al. (2004) indicate, different climate models simulate tropical warming patterns quite different and green house gas induced changes in the tropical precipitation remains a source of uncertainty (Selten et al., 2004). However Selten et al. (2004) showed, that tropical influences on the extra-tropics can be consistently identified in an ensemble of model projections, concluding that extra-tropical climate change is potentially predictable. The results presented in the present chapter support this hypothesis by showing that distinctive relations between the tropical Hadley circulation and extra-tropical circulation can be identified. Therefore, taking into account influences of tropical circulation features may be of great importance, particularly with respect to seasonal or decadal predictability and understanding projected extra-tropical circulation changes.

Chapter 4

Estimation of Impacts for Future Winter Storms

4.1 Introduction

In Chapter 2 future changes in severe European winter storms were investigated. Findings indicate that under increased greenhouse gas concentrations, both an increase in frequency as well as intensity of severe winter storms is expected particularly over the British Isles and parts of Scandinavia. For Germany an increase in the frequency of severe storm systems of about 20% has been found. Also, systems recurring once a year were found to increase in intensity by about 18%. As discussed in Chapter 2 these results are of course subjected to large uncertainties, however indicating increased loss potentials for future winter storms in Germany. For both frequency as well as intensity changes, results indicate stronger signals over northern Germany compared to southern regions.

The results presented in Chapter 2 were based on the evaluation of the so called storm severity index (SSI), taking into account the intensity, spatial extend and duration of fields of severe winds related to extra tropical cyclones. However, the occurrence as well as the actual height of losses related to such events are highly depending on the exposure as well as the vulnerability to locally arising severe winds. To be able to assess changes in future winter storm losses it is thus necessary to base further investigations on wind gust estimates (and their respective local climatology) derived from high resolution regional climate models which feature an adequate representation of orographic elevation including e.g. lower mountain ranges within Germany. Secondly, the treatment of exposure as well as vulnerability is envisaged. Of course the modeling of individual loss events (e.g. a roof failure) would require a comprehensive knowledge of both meteorological conditions (on a scale far beyond state of the art climate models) as well as a complete knowledge about the conditions of individual building structures. Thus it is only feasible to model exposure and vulnerability in a statistical sense for larger entities comprising a large building stock, e.g. for all buildings in a specific district. In such a statistical framework, the exposure can be modeled by using information such as the population density or the sum of insured values within each district. The vulnerability can then be derived from the analysis of historical loss experiences occurring within a district and relating those to the prevailing

local meteorological conditions. Such analysis then provides a description of the relation between meteorological conditions (i.e. sustained wind speed) and the amount of losses which in terms of a *storm damage transfer function* or short *storm damage model*. Such *storm damage model* can subsequently be applied to regional climate projections (in the present Chapter forced with greenhouse gas concentrations according to the SRES-A1B scenario (Nakicenovic et al., 2000)) to infer estimates of future storm damages. It needs to be kept in mind that the derived estimates of future losses are based on the assumption, that vulnerabilities derived from historical loss experience stay unaltered. Also changes in exposure (i.e. changes in the distribution of values) are only partly taken into account. As will be described in Section 4.3.1, instead of absolute values the focus will be on relative measures of losses i.e. losses standardized by the total amount of insured values (loss ratio). A future increase in insured values will thus not alter resulting loss ratios. However, uneven changes in insured values which might occur within Germany of course influence estimates for German wide losses (or loss ratios). These changes in exposure and vulnerability would require detailed projections of socio-economic developments within Germany and resulting changes e.g. in local distribution of values which are not in the focus of this work. Results can thus be only interpreted as the possible effect of altered climate conditions on damages under the assumption of unchanged vulnerability towards winter storms.

One aim of the work presented in this chapter is to investigate on the frequency as well as intensity of high impact storm events in Germany and to deduce possible influences of changed climate conditions. In this context, return characteristics (such as return levels and return periods) of loss intense winter storms shall be derived for future climate conditions (presented in Section 4.7). The rare and highly loss intensive natural disasters pose a considerable risk for the business of insurance companies (especially if their business is focused on small or regional markets). For such insurance companies it is thus of great importance to estimate such risks to establish appropriate capital reserves or to transfer corresponding risks to re-insurance companies. This line of research is also motivated by the fact that as part of the *Solvency II* framework directive, approved by the European Parliament in 2009, new regulatory guidelines have been set up demanding from insurance companies to hold reserve funds depending on their actual business risks (GDV, 2007). More precisely the guideline requires capital reserves which shall be adapted to a 1 in 200 year event. The second focus of work presented in this chapter lies on the assessment of regional changes in winter storm risks. Besides the implications for regionally active insurance companies this is motivated by the fact that in Germany the emergency management (as part of the civil protection) is by law a matter of the federal states. In light of changing climate conditions it is thus a major issue to develop regional and local projections of climate change impacts to be able to develop appropriate

adaptation strategies.

Impacts imposed by winter storms are considered a risk since naturally uncertainties exist about their occurrence and intensity. It is thus the aim to assess and characterize such risk in terms of their probabilities or likelihoods as well as their intensities which may differ from recent to future climate conditions. However estimated likelihoods and resulting risks are of course subjected to uncertainties themselves which need to be assessed. It is thus a key objective of this work to estimate these uncertainties arising from different origins along the modeling chain. For that, an ensemble methodology is developed enabling the estimation of uncertainties on severe wind speeds and derived impacts from high impact storm episodes (Section 4.6). Furthermore, uncertainties from the storm loss modeling procedure are considered in Section 4.4.3, and different sources of uncertainties will be integrated to get comprehensive uncertainty estimates on e.g. derived return values (Section 4.7). It will be shown, that estimates of future winter storm losses are in fact subjected to very large uncertainties. Besides the quantification of the range of possible climate change signals, probabilistic conclusions to represent these uncertainties will be presented and discussed (see Section 4.5).

4.2 Current State of Research

Based on the evaluation of historical storm losses, several definitions of storm loss functions relating losses to prevailing wind conditions have been made in the past. Dorland et al. (1999) suggested an exponential increase of losses with the maximum wind speed occurring during a storm event, which has been derived from a small set of 5 severe storm events and related losses to roofs and households in the Netherlands. Evaluations made by MunichRe (1993) instead suggest power law dependencies of losses increasing by wind speeds to the power of about 3 based on loss experiences of the 1990 storm series (Daria, Herta, Judith, Vivian and Wiebke in January and February 1990). Similar power law dependencies with powers of 3 have been used also in other studies (e.g. Palutikof and Skellern (1991) and Lamb (1991)) based on the loss experiences of the early 1990s in Europe. Evaluations of the storm series of December 1999 (e.g. Anatol and Lothar) found that different exponents of 4 to 5 may apply suggesting that a unique power law dependence may be hard to identify due to the large uncertainties inherent to storm losses.

In a recent study by Prahl et al. (2012) stochastic power-law functions have been fitted to observed loss data on German district level, where much higher exponents ranging between 8 and 12 were found. The storm loss model used in the present work, as described in Sections 4.4.1 and 4.4.2 is based on the approach presented in Klawa and Ulbrich (2003), which assumes a dependency of losses with the cube of normalized wind speeds exceeding a threshold depending on the local wind climatology. Leckebusch et al. (2007) derived

property loss potentials using a storm loss model (based on the formulation of Klawa and Ulbrich (2003)) from an ensemble of global climate models. Under future climate conditions according to the SRES-A2 scenario (Nakicenovic et al., 2000) for the end of the 21st century they find increased loss potentials for Germany of 21% compared to levels for recent climate conditions in the case of no adaption to changed climate conditions. Climate change signals were however found to strongly depend on the investigated climate model, with derived changes ranging from a decrease in loss potentials of -15% up to an increase by 44%. Based on an ECHAM5/MPIOM ensemble with three model simulations, Pinto et al. (2007) find higher increases for loss potentials in Germany which account for 40% for the SRES-A1B scenario and 49% for the SRES-A2 scenario. Again it is found, that resulting increases strongly depend on the considered ensemble member, showing that a large variability on inter annual and decadal time scales can lead to large spread in derived signals. Both studies agree in the finding, that if an adaption to changed climate conditions is taken into account changes in loss potentials are much smaller. While Pinto et al. (2007) in this case find an increase of 6% in loss potentials for Germany, Leckebusch et al. (2007) even diagnose a decrease in losses in case of a climate adaption. Donat et al. (2011a) derive storm loss potentials from an ensemble of GCM's as well as an ensemble of RCM's with future climate projections following the SRES-A1B scenario. It is found, that derived signals from RCM projections are significantly lower compared to signals from the GCM ensemble. For the end of the 21st century loss potentials are found to be 38% higher compared to recent levels when considering an ensemble of 9 GCM's and 15% higher when considering an ensemble consisting of 11 RCM simulations. Furthermore it is found, that loss potentials steadily increase during the 21st century with levels being 18% (5%) higher in the midcentury compared to the reference period 1961-2000 for the GCM (RCM) ensemble respectively. Again, uncertainties deduced from the inter-model standard deviation are found to be large and are in the range of derived change signals or even higher.

Schwierz et al. (2010) applied an operational insurance loss model to 3 regional climate simulations following the SRES-A2 scenario to derive changes in the impact of severe storm events in Europe. For European-wide losses annual expected losses (AEL) are found to increase by 44% with a disproportionate increase in losses for rare high-impact events. Losses of a 10 year event are found to increase by 23%, 30 year events by 50% and 100 year events by 104%. Furthermore, considerable regional differences in climate change signals are found with strongest increases of annual expected losses for Germany and Denmark which amount to 114% and 116% respectively. Respective uncertainties estimated from the range spanned by the different considered models are found to be rather small, especially concerning the increases derived for Germany. Comparing to previous studies (Leckebusch et al., 2007; Donat et al., 2011a) this might indicate, that uncertainties

due to natural variability on different time scales are not properly captured by the analysis of only 3 climate projections. Schwierz et al. (2010) conclude (in agreement to the results presented in Chapter 2) that a combined effect of an increase in frequency as well as intensity of severe winter storm events leads to the diagnosed increase in impacts. Pinto et al. (2012) analyzed loss potentials associated with European windstorms under future climate conditions from an ECHAM5-MPIOM multi-scenario ensemble. They find an increase in both frequency and potential losses caused by winter storms in central Europe including Great Britain, Benelux, Germany and Denmark for all considered emission scenarios (SRES-B1, SRES-A1B and SRES-A2) with most pronounced climate change signals derived for SRES-A2. In agreement with Schwierz et al. (2010) changes in return periods are depending on the rareness of the considered event. While for events with short return periods (1-10 years) only small shortening (or even elongation) of return periods is found for potential loss events in Germany, rare events with return periods of 100 years in recent climate are found to occur once in 35 (23) years in future climate conditions according to SRES-A1B (SRES-A2) scenario conditions.

There are only few studies focusing on estimating climate change influences on storm impacts for specific regions within Germany. Pinto et al. (2010) demonstrate the feasibility to assess future changes in loss potentials in regional terms by applying a statistical-dynamical downscaling approach to ECHAM5-MPIOM global circulation model climate projections. They are able to discriminate between larger climate change impacts over north-eastern parts of North-Rhine-Westphalia compared to western parts. From simulations following the SRES-A1B (SRES-A2) scenario, storm losses are found to increase by 8% (19%) over North-Rhine-Westphalia, which is considerably lower compared to changes derived in previous studies for the whole of Germany (Pinto et al., 2007; Leckebusch et al., 2007; Donat et al., 2011a). However, since the methodology differs from these studies direct comparison is not possible. Etienne and Beniston (2012) set a storm loss model according to Klawa and Ulbrich (2003) for the Swiss Canton of Vaud and investigate the climate change impact by increasing wind speeds of historic storm events arbitrarily by 3%, 5% or 10%. Even though these results are of course not comparable to climate change impact studies using projections of regional (or global) climate models, Etienne and Beniston (2012) are able to at least qualitatively assess possible climate change effects for this region and comparing results to effects from demographic growth. While losses are being found to react in a linear way to population growth, high sensitivity to small shifts in wind velocities are identified related to the third-power dependency of damage on wind speed. It is highlighted however, that both factors contribute to potential increases of future economic losses.

4.3 Data and Methods

4.3.1 Insurance Data

Insurance data on losses to residential buildings were provided by the German insurance association (Gesamtverband der Deutschen Versicherungswirtschaft e.V., GDV). These comprise daily data on administrative district level, with areas ranging from about 40 km^2 for urban municipalities (*Kreisfreie Städte*) to about 3000 km^2 for rural districts (*Landkreise*). In contrast to point wise measurements from meteorological stations, the available insurance data represent measurements with an area-wide coverage of wind storm and thunderstorm losses making it most valuable for various weather impact studies. The data however contains some limitations and uncertainties which need to be kept in mind. Uncertainties in daily losses arise from the fact that the exact time of loss occurrence is indistinct in some cases, especially if an event has occurred at night. In such cases, losses may be misallocated leading to uncertainties in the daily heights of losses. Furthermore, the area representativeness implies a dependence of losses on the local building stocks which needs to be taken into account. To gain data comparable amongst districts it is thus necessary to consider relative values i.e. losses standardized by the total amount of insured values (insured sum) in the specific district. Commonly used by insurances is the term *loss ratio* which denotes the *loss* (in €) divided by the *insured sum* (in thousand €) which is thus specified in ‰ (=1€/1000€). Besides ensuring spatial homogenization, the consideration of relative losses removes temporal inhomogeneities resulting e.g. from the growth of values or inflation. On district level, the GDV recorded losses on residential buildings arising from storm and hail events (covered by the *Verbundene Wohngebäude Versicherung*, VGV) for the period 1997-2007. This data set will be referred to as *VGV* in the following. Furthermore, records of losses from private vehicle insurance (KASKO) are available on district level dating back till 1984. Since building and vehicle losses were found to be highly correlated, residential building losses dating back till 1984, modeled by using simple regression analysis were provided by the GDV (compare Donat et al. (2011b)). This modeled data on building losses will be referred to as VGV-Sim in the following. It has to be noted though, that for the former eastern part of Germany, values are available from 1990/1991 on (with rather low insurance coverage in the first years after the German reunification). Besides on district level, losses will be considered on larger spatial aggregations e.g. for federal states or on a German wide aggregation. Special attention needs to be paid when aggregating loss ratios, ensuring the correct standardization onto the *insured sum* for such aggregated area A containing a set of

districts d,

$$\begin{aligned} \text{loss ratio}_A &= 1000‰ \cdot \frac{\text{loss}_A}{\text{insured sum}_A} = 1000‰ \cdot \frac{\sum_{d\in A} \text{loss}_d}{\sum_{d\in A} \text{insured sum}_d} \\ &= 1000‰ \cdot \frac{\sum_{d\in A} \text{loss ratio}_d \cdot \text{insured sum}_d}{\sum_{d\in A} \text{insured sum}_d}. \end{aligned} \tag{4.1}$$

Aggregation of loss ratio is thus achieved by averaging of local loss ratios, however weighting with the local *insured sum*.

4.3.2 Reanalysis Data

To set up the storm loss model presented in the following sections, the ERA-Interim reanalysis data set (Dee et al., 2011) is used. The reanalysis is computed on a T255 grid with 60 vertical model layers, supplying data on a grid with spacing of about 0.70 °(≈ 79km). As a predictor for wind storm losses daily maxima of near surface winds shall be used. These daily maxima are calculated from 6 hourly instant scalar winds at 10 m height. Alternatively, 3 hourly forecasted gusts in 10 m height are available from ERA-Interim. The ERA-Interim reanalysis are available from 1979 till present, enabling the evaluation period 1984-2007 for which both reanalysis and loss data are available.

4.3.3 Regional Climate Model Data

To assess regional changes in winter storm losses, an ensemble of regional climate projections using different regional climate models (RCM's) is evaluated. The RCM projections were produced within the ENSEMBLES project (van der Linden et al., 2009) and are forced using different global circulation models (GCM's) which themselves were forced with greenhouse gas emissions according to the SRES-A1B scenario (Nakicenovic et al., 2000). All RCM projections analyzed here have a horizontal resolution of 25 km and daily maxima of sustained 10m wind speeds are used. Alternatively, for some of the models parameterized wind gust estimates are available. However, for consistency purpose the maxima of scalar winds which are available for all considered models are used in the following. In total a set of 12 projections are evaluated as described in Table 4.1. For all model simulations, a reference period 1971-2000 under recent climate conditions (20C) is available for evaluation. Under SRES-A1B conditions two future periods are evaluated, a near future period (2021-2050) and a far future period (2071-2100). For the HC-HadRM3-HCh simulation, no data is available for the near future period (2021-2050), and thus needs to be excluded for this period. Further description of the analyzed RCM projections are given in Donat et al. (2011a) as well as in the specified References in Table 4.1.

Acronym	RCM	Institution	Driving GCM	References
RCA-HCMQ16	RCA3	Community Climate Change Consortium for Ireland	HadCM-Q16	(Kjellström et al., 2005)
HIRHAM-CM	HIRHAM	Danish Meteorological Institute	CNRM-CM3	(Christensen et al., 1996)
HIRHAM-EH-3	HIRHAM	Danish Meteorological Institute	MPI-ECHAM5 (3)	(Christensen et al., 1996)
CLM-HCMQ0	CLM	Swiss Federal Institute for Technology	HadCM3Q0	(Steppeler et al., 2003; Jaeger et al., 2008)
HRM-HCMQ0	HadRM3	UK Met Office, Hadley Center	HadCM3Q0	(Jones et al., 1995)
HRM-HCMQ16	HadRM3	UK Met Office, Hadley Center	HadCM3Q16	(Jones et al., 1995)
RACMO-EH-3	RACMO2	Royal Netherlands Meteorological Institute	MPI-ECHAM5 (3)	(Lenderink et al., 2003)
REMO-EH-3	REMO	Max Planck Institute for Meteorology	MPI-ECHAM5 (3)	(Jacob and Podzun, 1997)
RCA-BCM	RCA3	Swedish Meteorological and Hydrological Institute	BCCR-BCM2	(Kjellström et al., 2005; Samuelsson et al., 2011)
RCA-EH-3	RCA3	Swedish Meteorological and Hydrological Institute	MPI-ECHAM5 (3)	(Kjellström et al., 2005; Samuelsson et al., 2011)
CLM-EH-1	CLM3.2	Climate Limited-area Modelling Community	MPI-ECHAM5 (1)	(Jaeger et al., 2008; Rockel et al., 2008)
CLM-EH-2	CLM3.2	Climate Limited-area Modelling Community	MPI-ECHAM5 (2)	(Jaeger et al., 2008; Rockel et al., 2008)

Table 4.1: Evaluated combinations of regional climate model (RCM) simulations and corresponding driving GCMs from the ENSEMBLES project (van der Linden et al., 2009).

4.3.4 Wind Field Tracking for High Resolution Model Output

In Section 4.6, storm events identified in global climate model simulations (MPI-ECHAM5) and dynamically downscaled simulations using the regional climate model COSMO-CLM at a resolution of 0.165° (18 km) shall be compared. For this, the storm severity measure as described in Section 2.2.4 shall be considered, requiring an adoption of the wind field tracking procedure to high resolution model output. The wind field tracking as described in Section 2.2.3 has been successfully used for the analysis of GCM model data (see e.g. Leckebusch et al. (2008)), however applying it for high resolved data is not trivial. In high resolved simulations as used here (18 km) spatial structures such as atmospheric fronts lead to strong spatial variations in the wind fields, which complicates the tracking procedure. The rather homogenous single time step clusters from ECHAM5-MPIOM (with a horizontal resolution of T63) are often decomposed into sub clusters in COSMO-CLM which leads to problems in the nearest neighbor matching and thus to a splitting of resulting wind field tracks. Of course this problem also exists in low resolved

GCM simulations, however this leads to a splitting of wind field tracks only in few cases. To overcome this problem, the wind field tracking procedure has been slightly modified when applied to COSMO-CLM data. Instead of identifying single time step clusters at each time step (in the 2 dimensional wind fields) as depicted in Figure 2.1, contiguous clusters of threshold exceedances are identified in the 3 dimensional longitude-latitude-time array of wind data directly (Figure 4.1).

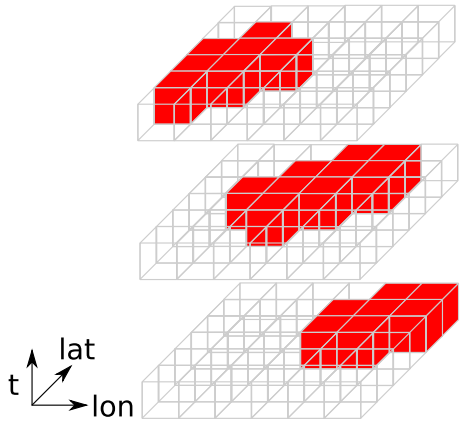

Figure 4.1: Modification of wind-field tracking. Instead of identifying clusters in the 2d wind fields for each time step, clusters are identified directly within the 3d longitude-latitude-time data array.

4.4 Modeling of Storm Damages

4.4.1 Basic Loss Model

In Klawa and Ulbrich (2003) a model for the estimation of storm losses based on maximum wind gust measurements was presented. Based on empirical evidence (MunichRe, 1993) losses are found to increase with the maximum gust to the power of close to 3, which has been supported by other studies (Palutikof and Skellern, 1991; Angermann, 1993; Lamb, 1991). Klawa and Ulbrich (2003) furthermore introduce the 98th percentile as a threshold for the occurrence of losses with the resulting storm damage function

$$loss \sim \left(\frac{v}{v_{98}} - 1\right)^3, \text{ if } v > v_{98}, \tag{4.2}$$

with v_{98} being the local 98th percentile and v being the maximum gust occurring. The introduction of such threshold is justified by the insurance's practice to cover losses in cases where gust wind speeds have been measured exceeding a threshold of 20 m/s at surrounding observation stations (coinciding roughly with the 98th percentile at the German

flatland stations). A relative rather than an absolute threshold is chosen since it can be assumed that both buildings as well as nature is adapted to local climatology of winds. This reasoning is justified e.g. when considering building regulations which are regionally specified within Germany depending on local wind climatology. One such example are the so called wind load zones according to the DIN-1055-4 regulation (DIN, 2005) shown in Figure 4.7 (right) which are based on the 98th percentile of 10m wind speeds averaged over a period of 10 minutes. Furthermore, an advantage of this approach is that the percentile exceedances are largely independent of the conditions at a location of the particular station. Thus it is possible to interpolate the scaled exceedances on the centers of administrative districts to generate a "footprint" of a storm field. The interpolated percentile exceedances are furthermore summed for the whole of Germany weighting each district with the local population density. This weighting is used since a proportionality to the local amount of insured values is assumed, which in turn is believed to stand in a linear relation to the height of losses to occur. Summing over all districts the cubic threshold exceedance weighted by the population density, the so called $LOSSINDEX$ is calculated

$$LOSSINDEX = \sum_{districts} pop(district) \cdot \left(\frac{v_{max}(district)}{v_{98}(district)} - 1 \right)^3, \tag{4.3}$$

which can finally be related to the German wide *loss*, assuming that a linear dependence on the $LOSSINDEX$. The resulting proportionality factor to describe how the amount of losses (in €) grows with increasing $LOSSINDEX$ is thus determined from linear regression analysis between calculated $LOSSINDEX$ time series and historic insurance loss records.

4.4.2 High-Resolution Refinement of the Storm Loss Model

To describe the prerequisites leading to natural disasters, concepts are usually based on the decomposition into the description of the *(natural) hazard* (i.e. the occurrence of a thunderstorm, winter storm or local extreme wind speeds) an *exposure* to such hazard and a *vulnerability* to the conditions imposed by the hazard. The loss model described in the previous section models these terms in a very simplified manner, where the *hazard (strength)* is described by Equation 4.2, the *exposure* via the population present in each district and the vulnerability as a single proportionality coefficient between $LOSSINDEX$ and actually occurring losses. Of course, besides the locally varying *exposure* within Germany, also the *vulnerability* is highly dependent on local conditions such as the building stock, building architectures and more complex factors such as coping capacities and infrastructure. However, the model described in the previous section does not include such differences. On the basis of insurance loss records on private housing broke down on district level,

which were provided by the Gesamtverband der Deutschen Versicherungswirtschaft e.V. (GDV), a refined loss model including such differences in vulnerability has been developed (Donat et al., 2011b). Using wind gust data from reanalysis data, the scaled percentile exceedances (according to 4.2) are interpolated on the district centers with a subsequent linear regression analysis relating it to occurred losses on district level

$$\text{loss ratio} = \frac{\text{loss}}{\text{insured sum}} = a + b \cdot \left(\frac{v_{max}}{v_{98}} - 1 \right)^3 . \tag{4.4}$$

In Donat et al. (2011b), resulting regression parameters are estimated using a set of 34 historic storm events listed in Table 1 of Donat et al. (2011b). For each storm event, the accumulated losses per district (over a period of at least 2 days up to 7 days) is calculated and related to the maximum wind gust from reanalysis data (e.g. from ERA-Interim) over this period according to Equation 4.4. Regression analysis then results in a set of coefficients $a(district)$ and $b(district)$ describing the local relationship (which can be interpreted as *vulnerability*) between the cubic percentile exceedances (*hazard strength*) and resulting impacts. Resulting spatial distribution of regression coefficients as presented in Donat et al. (2011b) are shown in Figure 4.2. Distinct differences in regression coefficients

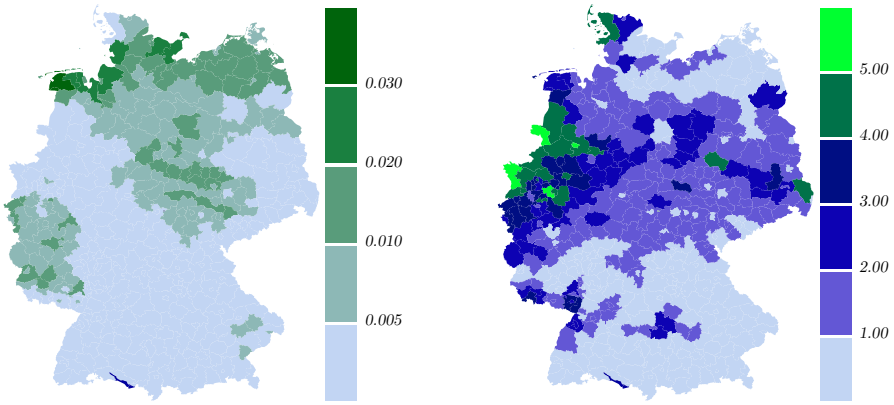

Figure 4.2: Linear regression coefficients of the refined loss model. Coefficients are based on a linear regression between the cubic exceedance of local 98th percentile and the loss-ratio, which is performed for each district (reproduced from Donat et al. (2011b)). (left) Intercept coefficient a in units of ‰. (right) Slope coefficient b in units of ‰.

are apparent especially for the slope (coefficient b), which may be interpreted as a measure for the local loss sensitivity to wind storms. Highest values of this slope coefficient are found in north-western parts of Germany, while low values are found in southern and eastern regions. The intercept coefficient a is generally found to be small. It has been noted in Donat et al. (2011b), that resulting regression coefficients may differ on the me-

teorological data set as well as on the loss data set (VGV/VGV-Sim) used. Although the general pattern is found to be robust this indicates rather large uncertainties in the estimates of the regression coefficients which shall be subject to further investigations in the following section.

4.4.3 Optimization of Storm Damage Model

It was found, that the refined loss model as described in Section 4.4.2 is subjected to rather large uncertainties expressed by uncertainties on the resulting local regression coefficients. In this section it shall be questioned whether local differences in such coefficients can be interpreted as actually existing differences in local vulnerabilities or if these differences are merely an expression of the rather uncertain relation between the cubic percentile exceedance (Equation 4.2) and actual losses. To tackle this question, a cross validation approach is used to assess and verify the predictive skill of the resulting loss model. Furthermore the influence of grouping districts into larger spatial clusters on resulting uncertainties is systematically investigated. The basic set up of the storm loss model is as presented in Section 4.4.2, however regression is performed on values on a daily basis. As meteorological input data, daily maximum of 10 m winds from ERA-Interim reanalysis (see Section 4.3.2 for description) are used. Analysis period are the years 1984-2007, for which losses from the data set VGV-Sim (see Section 4.3.1) are available. Starting point of

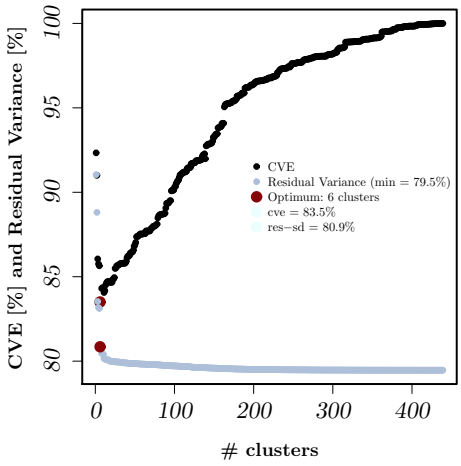

Figure 4.3: Cross validation error (CVE) relative to the CVE for the refined loss model (black). Residual variance relative to the total variance depending on the number of clusters is shown in grey.

the analysis is the refined loss model with estimated regression parameters for each of the 439 districts, constituting 878 free parameters. Within the cross validation framework, these coefficients are independently determined for 3 sub periods consisting of 16 of the

24 years of data availability. The remaining 8 years are used for validation, which is done by assessing the Mean Squared Error (MSE) between daily modeled and observed losses. MSE calculated for each district and each of the 3 cross validation periods are finally averaged to obtain the Cross Validation Error (CVE). Separately, the regression coefficients can be determined on the basis of the full 24 years of data availability to assess the Residual Variance (RV) being the complement of the model's Explained Variation (EV). Expressing the large uncertainties involved in the storm-loss transfer functions, the RV for the refined loss model accounts for about 79.5% of the total variance, implying that only about 20% of the daily variations in losses on district level are explained by the near-surface wind gusts used as a predictor for losses. After having set up the refined

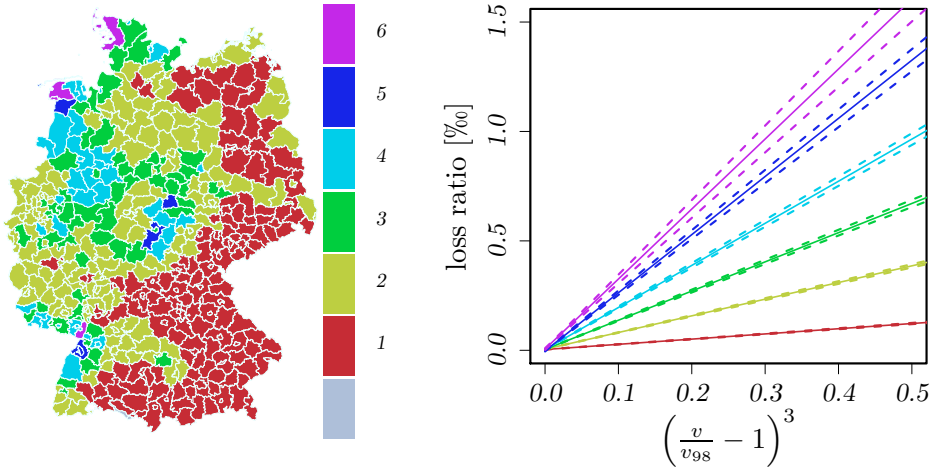

Figure 4.4: (left) Spatial map of the resulting clusters for the optimal partitioning. (right) Storm-damage transfer functions for the individual clusters.

loss model, the pair of districts exhibiting the smallest difference in regression coefficients is identified. Since generally the intercept parameter a, as well as its spatial variation is found to be small, this can be done simply by assessing the difference in the slope coefficient b. The two districts with smallest difference in b are then merged into one cluster, for which a unique regression line can be determined, which is then based on an enlarged data base. Thus, for these two districts 2 parameters instead of 4 suffice to describe the wind-loss dependence. Alternatively, the decision on the pair to be grouped together can be done in a more elaborated way testing out each possible pair of districts to find out the one to yield the largest reduction of the cross validation error. Iteratively, this merging of clusters is continued and after each iteration, the cross validation error is calculated. The algorithm terminates, when finally all districts are grouped together into one single cluster. Figure 4.3 shows the resulting cross validation error in dependence of the number of groups. Starting from 439 groups (on the right end of the plot), a reduction

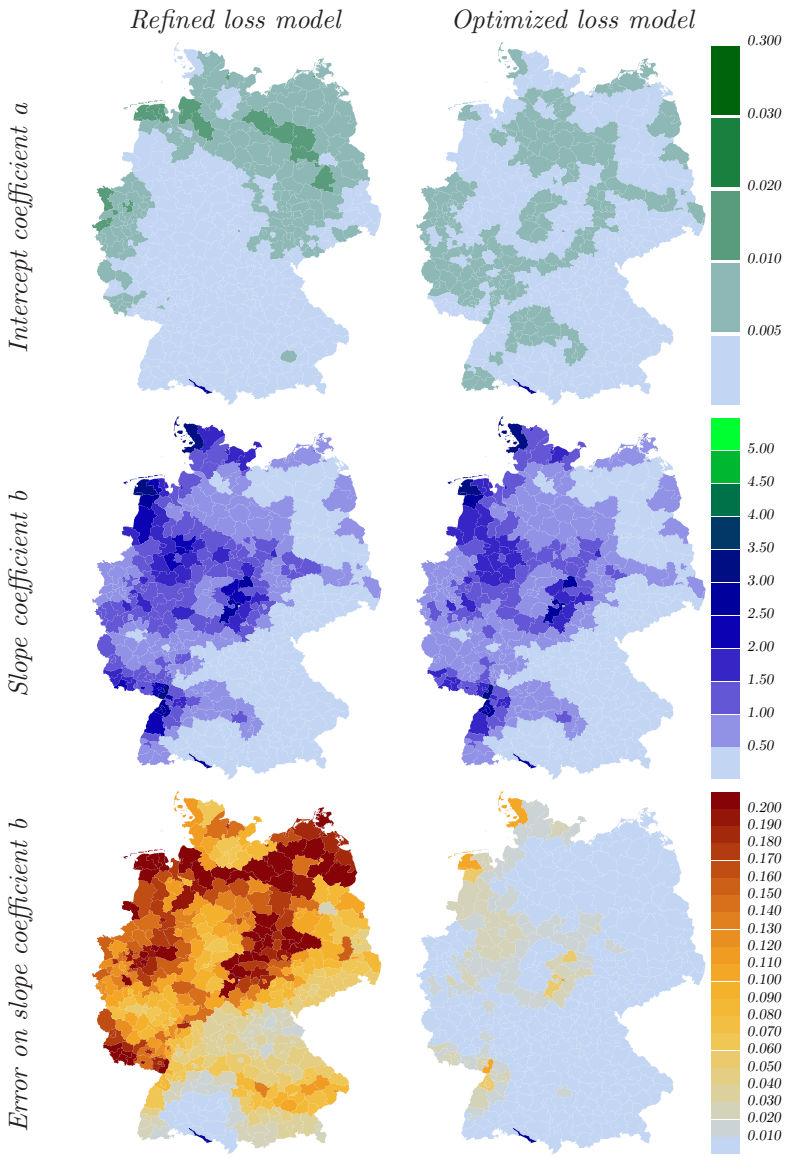

Figure 4.5: Comparison of resulting coefficients for the refined loss model (left panel) and the optimized model with 6 clusters (right panel). Intercept coefficients (in ‰) are shown in the top row, slope coefficients (in ‰) in the middle row. Resulting errors (standard deviation) on the estimated slope coefficient b are shown in the bottom row.

in cross validation is found when grouping the districts. Eventually, the minimum CVE is found for 6 clusters, with rising CVE for smaller number of groups. Compared to the initial CVE (for the refined loss model) the minimal value is found to be 83% indicating the reduction of modeling errors of about 20%. At the same time, the residual variance for the model which is now described by only $6 \cdot 2 = 12$ free parameters is 81% of the total variance in losses. This is only slightly worse compared to the refined loss model based on

$439 \cdot 2 = 878$ parameters. Continuing the clustering results in a strong decrease in residual variance, meaning the predictive skill of the model is decreasing. Figure 4.4 shows a map of the resulting spatial clusters of districts (left) and their corresponding storm-damage transfer functions (right). Large parts in eastern and southern Germany are grouped into a single cluster exhibiting a very low increase of losses with increasing wind speeds. Three clusters with medium slopes in the storm loss function are found which distribute over central and western areas of Germany. Two clusters with high slopes in the storm-damage functions are found, which include only a few districts mostly in coastal regions. However both cluster include also single districts which are found far off the coastal regions, but which are found in regions with high orographic variations. It can be assumed that the certain orographic surrounding leads to channeling effects in these districts leading to high storm sensitivity if certain wind directions are present.

Finally, spatial maps of resulting coefficients are presented in Figure 4.5 for the refined loss model on district basis (top row) and for the optimized model with 6 clusters (bottom row). Considering the values of the intercept coefficients (left) which are generally found to be small, slight differences are found. Intercepts tend to be lower and become more homogeneously over Germany in the clustered model. The slope parameter b (right) is generally found to be in good agreement, meaning that the clustered model is able to reproduce the distribution of coefficient b, with however only 12 free parameters to be estimated. At the same time, uncertainties on estimated coefficients are significantly reduced. Estimated errors on the slope coefficients (σ_b) resulting from the maximum likelihood fit procedure are shown in Figure 4.5 (bottom row) for the refined loss model (left) and the optimized version using 6 clusters (right). In the first case σ_b ranges up to values above 0.2 which indicated an uncertainty of about 10% of the slope coefficient for large parts of Germany, with relative uncertainties exceeding even 50% for north-eastern regions. In comparison, uncertainties derived for the optimized version using 6 clusters are significantly reduced since linear regression is performed on a much higher data basis. σ_b in this case ranges up to 0.13 in only few districts (belonging to cluster 6 with only 4 member districts), in average being lower than 0.01.

4.5 Uncertainties in Regional Loss Projections

In Chapter 2 changes in both frequency and intensity of winter storms were investigated on a European scale. An increase in frequency and an increased severity of rare storm events has been diagnosed for central and northern Europe, which however is not uniform. Over northern Germany more distinct increases are found compared to the southern regions. In Section 4.4.3, it was shown that the modeling of locally occurring losses is affected by large uncertainties, with losses depending on multiple factors such as the surrounding

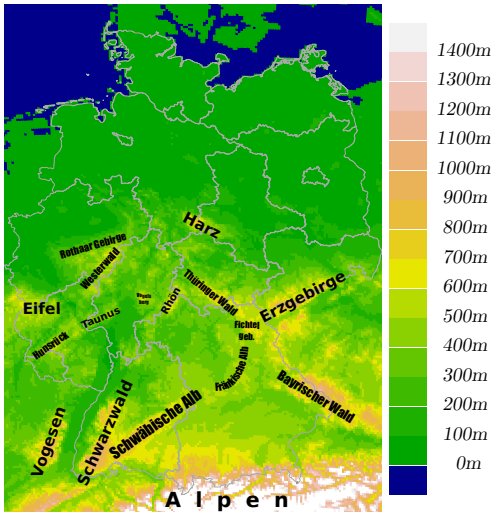

Figure 4.6: Map of the topographic height for Germany.

topography as well as locally varying vulnerabilities given e.g. by architecture and coping capacities. Using the high resolution loss model presented in Section 4.4.3, it shall be investigated if regional differences in future changes of losses can be derived and how such differences might look like. In this Section, the focus is on mean yearly losses and their respective changes under SRES-A1B scenario condition. 12 regional climate projections using different regional climate models (as described in Section 4.3.3) are analyzed. Losses are modeled on a daily basis for 30 year periods from which mean yearly losses are derived. For each model, losses are calculated for the recent climate period 1971-2000 (20C) and two future climate periods 2021-2050 and 2071-2100 (SRES-A1B) to assess potential changes in mean losses. Changes shall be investigated on three spatial aggregation scales: German wide, district based (*Landkreise* and *kreisfreie Städte*) and an intermediate aggregation level based on the 16 *Bundesländer*. On this aggregation level, the 3 city states (*Berlin*, *Hamburg* and *Bremen*) are treated as parts of their surrounding (or neighboring) states (respectively *Brandenburg*, *Niedersachsen* and *Schleswig-Holstein*).

4.5.1 Historical Losses

Mean yearly loss ratios on district basis, observed in the period 1984-2007 (new *Bundesländer* 1990-2007), are shown in Figure 4.7 (left). Higher loss ratios are found in northern half of Germany and in western regions, while southern regions generally feature lower values. Highest loss ratios are diagnosed in districts along the North Sea coast but also in specific regions such as the *Ruhrgebiet* or the *Saarland*. It can be found that orography, and especially the secondary mountain ranges labeled in Figure 4.6, have a rather strong influence on this pattern. The high loss ratios in the *Ruhrgebiet* can thus be

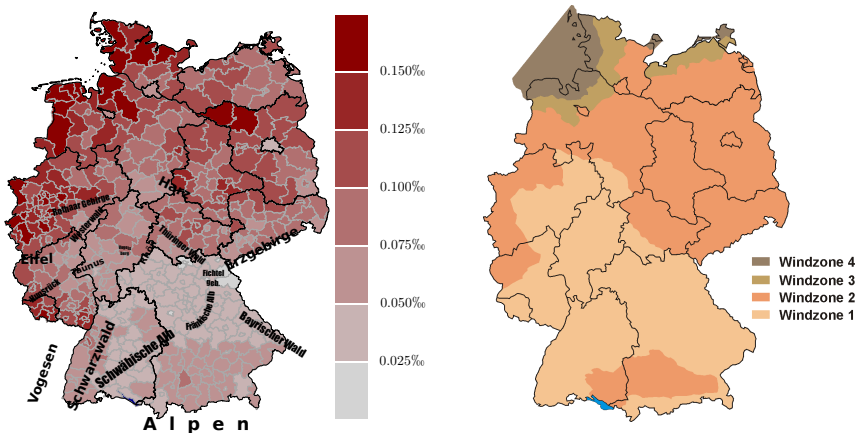

Figure 4.7: (left) Mean yearly loss ratio in units of ‰per district observed for the period 1984-2007. (right) Wind load zones according to DIN 1055-4 (DIN, 2005). (Source: Wikipedia - Windzonen nach DIN 1055-4:2005-03).

attributed to the location north-west of the mountain ranges *Eifel*, *Rothaar Gebirge* and *Westerwald*. Under northern and westerly flow conditions this location windward of the mountain range might lead to an enhanced exposure to severe winds, which can furthermore be enhanced since the constellation of *Rothaar Gebirge* and *Eifel* might generate a "jet effect" in some of these regions. Similarly "jet effects" formed by the *Hunsrück*, the *Vogesen* and the *Schwarzwald* (in south westerly flow conditions) might lead to the high loss ratios observed in the *Saarland*. "Lee" effects can be found for example east from the *Schwarzwald*, southeast of the *Rhön* and in the districts east of the *Fichtelgebirge*. The horseshoe-like shape of the *Fichtelgebirge* contributes to the fact, that the two districts *Tirschenreuth* and *Wunsiedel* east of this mountain range feature the lowest loss ratios amongst Germany. Only for the district of *Coburg* a lower loss ratio of 0.0198‰ is found, which is partly due to the fact that for the (*Kreisfreie Städte*) generally lower loss ratios are found compared to their surrounding districts. Compared to the maximum of 0.234‰ found for *Aurich* this is less than one-tenth, showing the huge differences amongst Germany. Aggregating losses for the *Bundesländer* (as shown in Figure 4.8, bottom-left) it is found that *Bayern* features the minimum, accounting for 0.045‰ while in *Schleswig-Holstein & Hamburg* with a mean loss ratio of 0.135‰ the threefold can be found. Qualitatively, the comparison of the spatial pattern of occurred mean losses to the wind load zones according to the DIN-1055-4 (DIN, 2005) norm shown in Figure 4.7 (right) shows remarkably good agreement to these findings. However, differences are found e.g. in areas such as the *Saarland* and the southern *Rhine valley* where rather high losses can be diagnosed, the regions however being declared as part of the lowest wind load zone.

4.5.2 Modeling Losses under Recent Climate Conditions

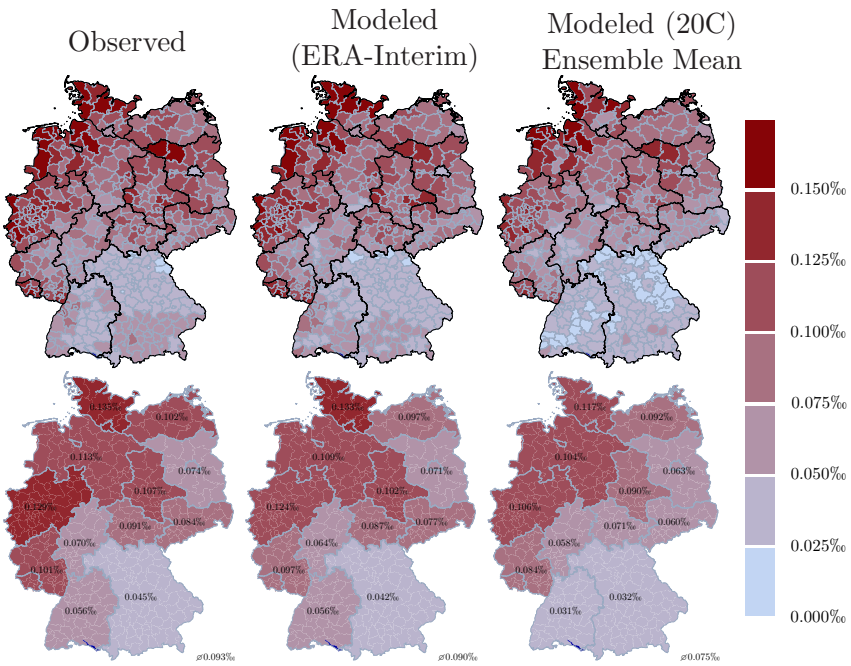

Figure 4.8: (top-row) Mean yearly loss ratio per district in ‰. (left) As diagnosed from observed losses in the period 1984-2007. (middle) As modeled from ERA-Interim for 1984-2007. (right) Ensemble mean modeled loss ratio from the 12 member RCM ensemble under recent climate conditions in the period 1971-2000. (bottom-row) Aggregated loss ratio in ‰for the 12 regions based on the German Bundesländer.

Figure 4.8 shows the comparison of mean yearly losses observed (left) to modeled losses from ERA-Interim (middle). The loss model used here is the optimized version with 6 clusters (so in total 12 coefficients were determined to describe the full model). Analyzing modeled losses from ERA-Interim (which has been used for training of the loss model), it is found that the spatial distribution of observed losses is very well reproduced. If using the refined loss model in which regression coefficients are determined on district basis, long term means are actually by definition equal. Here, the optimized loss model is used leading to small local differences, as described in more detail in Section 4.4.3. Also when considering the ensemble mean of mean yearly losses as modeled from the 12 member RCM ensemble under recent climate conditions as shown in Figure 4.8 (right), a good agreement to observed losses is found. Modeled losses tend to be underestimated, with a German wide mean yearly loss ratio of 0.075‰ compared to observed 0.093‰. There is however considerable ensemble spread in German wide mean yearly losses ranging between 0.066‰ (RACMO-EH-3) and 0.112‰ (HIRHAM-CM). Aggregating for the *Bundesländer* (see Figure 4.8 bottom-left for observations and bottom-right for the 20C ensemble mean)

it is found, that the the underestimation is found in each of the considered regions with no distinct spatial dependence. In terms of relative deviation for *Baden-Würtemberg* the largest underestimation by roughly 50% is found. In this context, the role of storm Lothar in 1999 should be highlighted, which affected mainly the south-west of Germany with immense loss (loss ratios exceeding 0.5‰ in large areas of *Baden-Würtemberg*). With it's extremely high wind speeds (especially considering the climatically lower wind speeds in southern Germany), Lothar generated more than 40% of all losses in the 24 year observation period 1984-2007 in large parts of *Baden-Würtemberg*. In areas of low storm affectedness such as *Baden-Würtemberg*, the occurrence of an event similar to *Lothar* can thus make up an immense difference in mean losses.

4.5.3 Future Changes in Losses

To assess future changes in losses, the climate projections under SRES-A1B scenario conditions are evaluated and compared to 20C levels. Relative changes in mean yearly loss ratio (MYLR) are calculated as $100\% \cdot [MYLR_{A1B} - MYLR_{20C}] / MYLR_{20C}$, where the reference $MYLR_{20C}$ is calculated for the individual model simulations under recent climate conditions. The ensemble mean of relative changes calculated from the 12 RCM projections are shown in Figure 4.9 for the near future period 2021-2050 (left). Increases between 5% and 15% are found for most of the central and northern regions of Germany. One exception are some regions in the far north where larger increases of 20% and more are found. In the south-western regions (and especially in the southern Rhine valley) regions can be found for which rather strong decreases (of up to 30%) in losses are found. Aggregated for the *Bundesländer* as shown in Figure 4.9 (bottom left), the results imply an increase of losses in *Schleswig-Holstein* of about 19% while losses are found to decrease by 14% in *Baden-Würtemberg*, while the German wide loss ratio is found to be increasing by 8%. Figure 4.9 (right) shows results for the second future period (2071-2100), for which generally a continuing increase in losses is found. Largest increases are found in northern and western regions of Germany, where relative increase are higher than 50% compared to 20C levels locally. With only few exceptions most districts feature clearly positive increases in mean losses. For each of the regions based on the *Bundesländer*, increases of losses are found in a range from 5% (*Bayern*) and 28% (*Schleswig-Holstein*) (compare Figure 4.9, bottom right). Besides the north/south differences in changes, which has also been found in the near future period, a west/east difference becomes evident. While the eastern *Bundesländer* feature moderate increases of about 7%, much stronger signals of about 17% are found in western regions. An exception is found for *Niedersachsen*. While for the coastal regions of *Niedersachsen* also strong increases of about 17-20% are found, inland regions feature only small changes in losses which averages to an intermediate increase of 12%. Generally, a continuous increase in losses is diagnosed for most of the

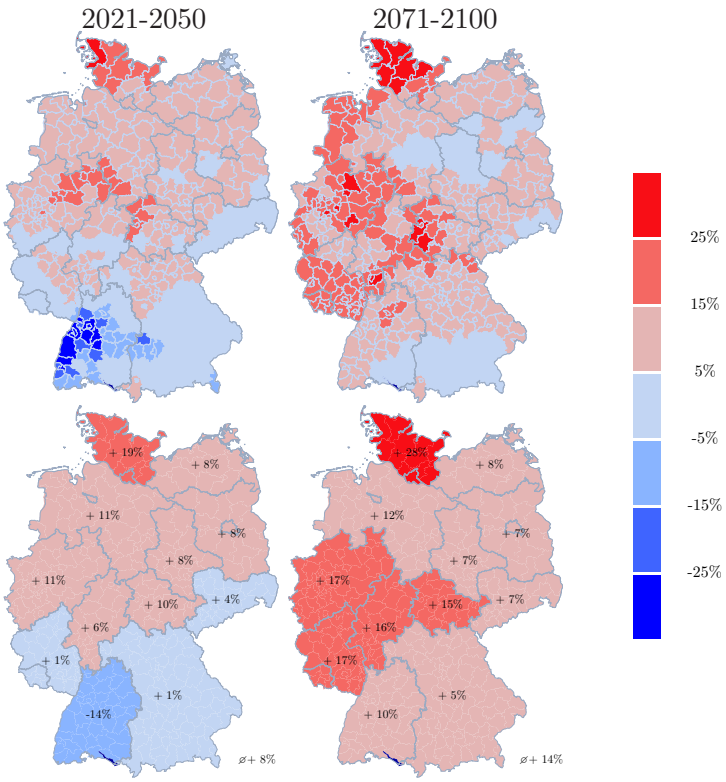

Figure 4.9: (top-row) Ensemble mean of the relative differences in mean yearly losses for (left) 2021-2050 and (right) 2071-2100 compared to 1971-2000 on the basis of individual districts. (bottom-row) Ensemble mean of relative differences aggregated on Bundesländer for the same periods.

districts and for aggregated losses on *Bundesländer* level. This is however not true in all cases, most prominently in the case of *Baden-Würtemberg*, where a decrease towards the middle of the 21st century is diagnosed followed by an increase towards the end of the century. This demonstrates that even though based on an ensemble consisting of 12 (or 11 for the mid-century period) regional climate model projections, large variability may be present which is related to the fact that few severe storm events can significantly affect the long term averages in derived losses, especially on regional scales.

4.5.4 Uncertainties on Derived Changes

4.5.4.1 Uncertainties from Damage Model

As noted in Section 4.4.3, the estimation of coefficients entering the storm loss model is subjected to rather large uncertainties (compare e.g. Figure 4.4). To estimate the effect of this coefficient uncertainty on the derived climate change signal, losses are assessed from the regional climate model projections using on the one hand the best estimates of coefficients a and b, but also replacing b by it's lower and upper bound, $b \pm \sigma_b$, respectively.

In general, higher slope coefficients b can be expected to lead to stronger change signals in derived losses, since they imply higher sensitivity to severe wind conditions. Possible changes in the intensity of severe wind gusts thus translate into larger changes in derived losses. Uncertainties on derived changes in long term means of losses, resulting from the storm-damage model uncertainties, can thus be estimated by calculating losses by means of a "low-sensitivity" assumed in the storm-loss model (with slope coefficients $b - \sigma_b$) and a "high-sensitivity" (with slope coefficients $b + \sigma_b$). Coefficient uncertainties in case of the refined loss model (determining regression coefficients on district basis) were found to be rather large (compare Figure 4.5, bottom left), correspondingly leading to large uncertainties on derived changes in long-term losses (Figure 4.10, left). E.g. for the CLM-EH-2 simulation, German wide losses are found to increase by about 0.013‰ with an uncertainty related to the "storm-sensitivity" ranging between about 0.006‰ and 0.02‰. Especially for models projecting strong increases (e.g. CLM-EH-1, RACMO-EH-3 and HIRHAM-EH-3) these uncertainty ranges become particularly large. As demonstrated

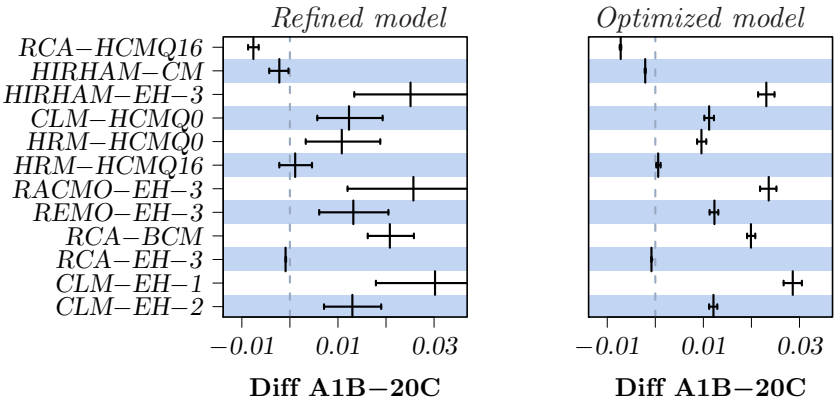

Figure 4.10: Diagnosed changes in the German wide mean yearly loss ratio (in ‰) for the individual model simulations using the refined loss model (left) and the optimized model with 6 clusters (right). Storm damage uncertainty is shown in horizontal bars, assessed by calculating losses and respective changes based on "low-sensitivity" and "high-sensitivity" (see text).

in Section 4.4.3, the uncertainty on the estimated regression parameters is considerably reduced by grouping regions with similar storm-loss transfer functions. This reduction in coefficient uncertainty correspondingly reduces the uncertainty in projected changes in long term losses (Figure 4.10, right). With uncertainties in case of the refined loss model being in the order of the ensemble spread, the uncertainties for the optimized loss model are found to be reduced (for CLM-EH-2 uncertainty ranges from 0.011‰ to 0.013‰) to be considerably lower compared to the ensemble uncertainty which shall be considered in the following section.

4.5.4.2 Ensemble Uncertainty

The discussed mean losses as presented in Section 4.5.2 as well as the change signals presented in Section 4.5.3 referred to the ensemble mean of 12 (11) RCM projections. For the individual model simulations however, a large spread in mean losses calculated under both 20C conditions (1971-2000) as well as SRES-A1B (2021-2050 and 2071-2100) are diagnosed (compare Figure A.7 of the Supplementary Material), consequently leading to large differences in the individual models projected changes (compare Figure A.8 of the Supplementary Material). The resulting ensemble spread in terms of projected relative changes in long-term mean losses for the future period 2071-2100 are depicted in Figure 4.11, showing the ensemble minimum of relative changes for each *Bundesland* (left) and the corresponding ensemble maximum (right). For nearly all regions, the ensemble

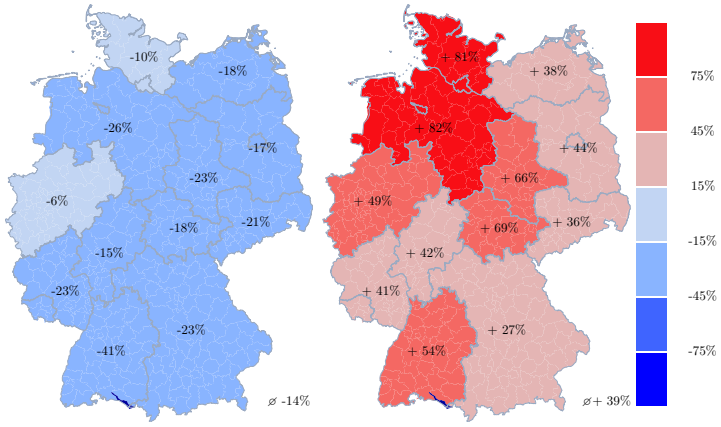

Figure 4.11: Ensemble minimum (left) and ensemble maximum (right) of relative change (in %) in mean yearly losses for the future period 2071-2100, compared to the reference period 1971-2000.

range indicates the possibility of a decrease in losses ranging between -6% (for *Nordrhein-Westfalen*) and -41% (for *Baden-Würtemberg*). The upper limit ranges from an increase of +27% (*Bayern*) to an increase of more than 80% (*Niedersachsen* and *Schleswig-Holstein*). Changes of German wide losses are found to range between -14% and +39%. This large range of possible climate change signals indicates that it might be of use to interpret these results in a probabilistic manner. A first guess of the certainty that an increase of storm losses will happen is to simply count the number of models for which an increase in losses is found. For the near future period (2021-2050) it is found, that for most of the northern regions 8 or 9 of the 11 model simulations exhibit an increase. In contrast for the southern regions (*Bayern* and *Baden-Würtemberg*) only 4 of the model simulations exhibit an increase, implying that a majority of models exhibit a decrease in storm losses. In the second future period in all regions of Germany the majority of models (at least 7 out of

12) show an increase in losses. However the model agreement ranges from a very weak majority (7 of 12 models) in some eastern regions such as *Brandenburg* to a rather strong agreement with 10 of 12 models showing an increase in northern and western regions.

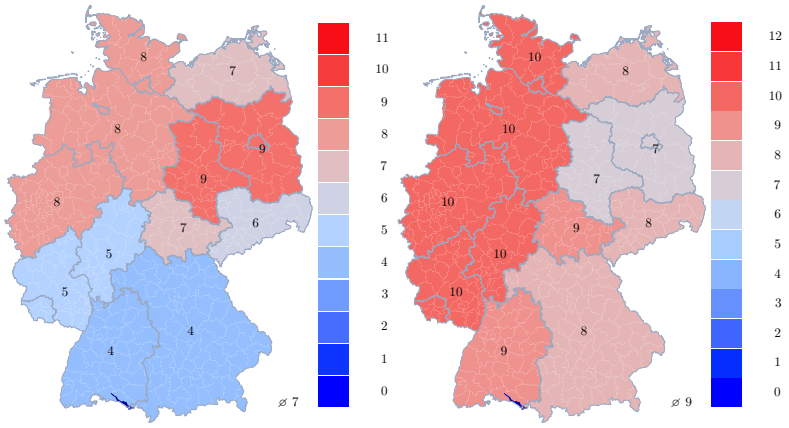

Figure 4.12: Number of RCM simulations projecting an increase in mean losses under SRES-A1B conditions in the future periods 2021-2050 (left) and 2071-2100 (right) compared to the reference period 1971-2000.

4.6 Assessment of Dynamical Downscaling Uncertainties[1]

The impact of severe winter storms strongly depends on the precise local meteorological conditions, which makes it essential to identify and quantify uncertainties associated to local wind extremes related to severe winter storm events and investigate how these uncertainties propagate into derived quantities such as winter storm losses. Estimations of the severity of extreme events are used on time scales ranging from nowcasting to climate change considerations, with different goals (like warnings or long term planning) assigned to the specific time scale. At all scales, however, uncertainties of the forecasts must be taken into account. Besides systematic errors due to insufficient knowledge about the relevant processes, boundary conditions or an insufficient representation in the numerical models used for conducting the forecasts, a main issue is the uncertainty arising from the chaotic characteristics of the atmosphere. In deterministic weather forecasts, small deviations in the initial conditions or in the processes during its development can lead to different intensities, locations and temporal characteristics of a severe weather event. This is commonly addressed by creating ensembles of forecasts, in particular by introducing specific (but small) changes to the initial conditions of a forecast, using different boundary

[1]submitted for publication to *Meteorologische Zeitschrift*
Pardowitz, T.; Befort, D. J.; Leckebusch, G. C. and Ulbrich, U. (2014) Estimating uncertainties from high resolution simulations of extreme wind storms and consequences for impacts.

data sets (e.g. the COSMO-LEPS system run by the German weather service (Montani et al., 2003)), singular vector methods (see e.g. Palmer et al. (2007)) or allowing for a variation of the parameterized representation of physical processes in the model (see e.g. Forest et al. (2002)). The creation of ensembles using such approaches is valuable, but quite complex if not implemented into a modeling system. Recently, Sasse and Schädler (2013) suggested an easy-to apply method to generate an ensemble of RCM simulations by applying a so called Atmospheric Forcing Shifting (AFS) method. In this method, the forcing GCM fields are shifted by 25 (or 50 km) with respect to the model orography. The authors find that for long term simulations the uncertainties generated by the AFS technique do not exceed uncertainties resulting from the use of different forcing data sets, however considerable differences are introduced by the AFS technique, especially with regard to extremes. In this paper, a technique is used which is similar to that mentioned previously in terms of taking exactly the same RCM and exactly the same data source for the ensemble. In contrast, the relationship to the underlying orography and land-sea mask are not changed and will thus still lead to physical consistent realizations of the storm event. Instead, the nest of the RCM into the driving model is shifted, resulting in a few more (or less) grid points at the individual boundaries. As the choice of the location of the nesting domain for a simulation of events far enough from the boundaries is arbitrary, such a shift can be regarded as a simple and consistent approach, as long as it is assured that lateral boundaries are distant enough from the area of interest to allow for a proper relaxation. The method is applied to the intensity of extreme windstorms, eventually analyzing European wind storm risk in present day and in a scenario climate. Based on a list of identified storm events from a 3-member GCM simulation, two RCM based approaches for estimating storm risk under different greenhouse gas (GHG) forcing are conducted and compared. The intention is thus not to compare the simulated storm intensities to local observations (e.g. Born et al. (2012)), but to get a better knowledge of the range and probabilities of possible extremes. Firstly, the total intensity of a storm system is quantified using the so called storm severity index (SSI), integrating a damage-related measure of extreme surface wind speeds over the area and the duration of a storm, irrespective of the exact location of the simulated extreme winds. The results using this quantification of storm severities is compared to those based on estimate of the impacts using a calibrated storm damage model which takes the spatial distribution of exposure and vulnerabilities into account. Thus, it is intended to show how large the ensemble variations are in terms of meteorology and in terms of impact, and what the consequences are in terms of return periods of extremes.

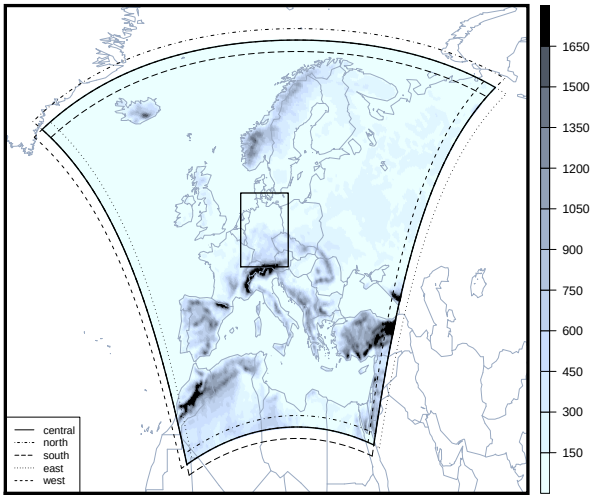

Figure 4.13: COSMO-CLM topography (shaded), domain location of the five ensemble members (lines) and Germany box (rectangular).

4.6.1 Ensemble Generation Technique

In this study data from the MPI-ECHAM5 model runs conducted for the IPCC-AR4 (Roeckner et al., 2006) are used as driving data for the regional model simulations. Each of the three transient climate simulations was forced with observed greenhouse gas (GHG) concentrations for the period 1860-2000 and with SRES-A1B scenario concentrations thereafter. Four 30-year time slices were considered: 1970-2000, 2011-2040, 2041- 2070 and 2071-2100. MPI-ECHAM5 has been chosen for downscaling, since previous studies suggested a good agreement of this single model ensemble with a multi-model ensemble in terms of the climate change signals of winter storm impacts (Donat et al., 2011a) and the mid-latitude synoptic scale variability (Ulbrich et al., 2009). The COSMO model in Climate Mode (COSMO-CLM, see Doms (2011)) is the community model of the German regional climate research. This model is based on the COSMO numerical weather prediction version used by several weather prediction centers across Europe. Here, the COSMO-CLM version 4.0 (Böhm et al., 2008) is used. The model is run on a rotated pole grid with a horizontal resolution of 0.165°x0.165°(≈ 18 km) with 32 vertical levels, and the temporal discretization is performed using a leap-frog scheme with a internal time step of 150 seconds. The total extend of the entire domain is 257x271 grid cells. The relaxation of forcing data at the models lateral boundaries is performed using a scheme similar to Davies (1976) and Davies (1983). Wind gusts in 10m height are calculated from wind speeds at levels above the boundary layer and static stability according to Schulz and Heise (2003) and Schulz (2008). Maxima of wind gusts in 6 hourly intervals are used for the Wind storm identification and quantification procedure as presented in Section 4.3.4

and daily maxima are used for the modeling of storm damages as described in Section 4.4. The nesting of the COSMO-CLM into the MPI-ECHAM5 data for a certain domain covering all of Europe and parts of northern Africa (Figure 4.13) is repeated with four additional nesting domains which are shifted by 8 COSMO-CLM grid boxes to the north (dot-dashed), south (long dashed), east (dotted) or west (dashed). The shift by eight grid boxes is motivated by the fact that this is the zone which is usually significantly affected by relaxation at the boundary Doms (2011). Instead of performing continuous downscaling simulations using the COSMO-CLM, which would lead to large computing resources necessary, the strongest 30 events affecting the German region were selected from each of the four time slices. Thus, in total 120 storm systems are selected and dynamically downscaled using COSMO-CLM. Six hourly maxima of wind gusts in 10m height, which are parameterized are analyzed.

4.6.2 Comparison of GCM and RCM

Comparing the SSI footprints from GCM and RCM, orographic effects and additional features such as land-sea contrasts at the coastlines which result from the higher resolution become visible. SSI footprints for an example storm system identified in MPI-ECHAM5 run 1 (start: 1997-11-11 18:00 UTC, end: 1997-11-18 12:00 UTC) are shown in Figure 4.14, with (a) showing the storm's footprint as represented in MPI-ECHAM5 and (b) the representation in COSMO-CLM. Besides the effects due to the higher resolution, spatial intensity characteristics of the RCM are in good agreement to the driving model. Resulting wind field tracks, which represent the centers of the SSI footprint at a specific time step, compare well as shown in Figure 4.14, the track however being slightly shifted northward in COSMO-CLM. Also, the resulting SSI value from MPI-ECHAM5 within the COSMO-CLM domain (0.46), compares well to the SSI calculated for the central realization of the COSMO-CLM simulations (0.54). To check for systematic differences in SSI values between the forcing GCM and the downscaling, Figure 4.15 (a) shows the scatter-plot between SSI's from MPI-ECHAM5 to the ones calculated from COSMO-CLM. Black dots indicate the ensemble mean of the 5 COSMO-CLM ensemble realizations of a specific storm event, for which a high correlation of 0.87 is diagnosed compared to the values from MPI-ECHAM5. Considering the mean of all 120 storm systems chosen for downscaling, a bias of COSMO-CLM ($\overline{SSI}$=0.38) towards lower values is diagnosed compared to MPI-ECHAM5 ($\overline{SSI}$=0.47). This might be surprising at first sight, since it is generally believed that the extremes in wind speeds are better represented in high-resolution simulations. When comparing RCM simulation to the forcing GCM a bias towards higher intensities of storm systems could thus be expected. The approach chosen here for the calculation of SSI is based on relative threshold exceedances, relating the wind extremes to the model's local climatology using the 98th percentile (Equation 2.2).

It is obvious, that this climatology (the distribution of gusts) itself can differ depending on the investigated model and its resolution. The local 98th percentile which is used as the threshold in Equation 2.2 can thus be considerably higher in the high resolved simulations leading to lower threshold exceedances in turn.

4.6.3 Deriving Uncertainties in Modeled Storm Impacts

The uncertainty in storm impacts is investigated by considering the ensemble spread spanned by the 5 realizations of the COSMO-CLM ensemble. For the example shown in Figure 4.14, this spread in the SSI is found to be 0.032 corresponding to a relative spread of 6%. Considering the temporal evolution of the storm system (Figure 4.14, c), it becomes obvious that the absolute spread is dominated by the spread in peak intensity. Additionally in the SSI footprint the largest spread is found in the regions of highest intensity (not shown). This is easily understood considering the cubic dependence of wind speed exceedances in Equation 2.2. Small deviations in the high threshold exceedances are amplified and thus contribute most to the generated spread in SSI. Considering the relative spread of the SSI footprint (Figure 4.14, d) values of up to 100% can be found along the path of highest intensity of the storm system. The relative spread however is particularly high at the edges of the storms footprint. This points out the uncertainties of the exact area which is affected by the storm system, which differs slightly in all five COSMO-CLM members. There is a tendency towards higher spread for more intense storms as shown in Figure 4.15, which can be explained by the non linear amplification of uncertainties in gusts for the case of large threshold exceedances. However, this tendency is subjected to large variations showing that the uncertainties involved are obviously highly dependent on the particular storm situation. Figure 4.17 (a) shows the distribution of relative spread, when considering all 120 storm simulations. It is found that for about half of all events a spread larger than 25% is diagnosed, for about 25% of the events a spread larger than 50% and for only a few events the spread raises above 100%.

To assess the impact of those winter storm events (depending on the distribution of values and locally varying vulnerabilities as described in Section 4.4), modeled loss ratios for all COSMO-CLM simulations are calculated (see Figure 4.16 for the example storm system in Figure 4.14). The spatial distribution of modeled impacts (Figure 4.16a) is well comparable to the SSI footprint shown in Figure 4.14b. However, due to differences in local vulnerabilities (modeled through the coefficients a and b) local differences become apparent. These of course strongly amplify if modeled losses instead of loss ratios were shown, since insured values exhibit large variations. Similar to the relative spread in the SSI footprint (Figure 4.14d), relative spread of modeled loss ratios are calculated (Figure 4.16b). As discussed above, large uncertainties (large ensemble spread) ranging up to 100% are found in regions of highest impacts (coastal areas in this example). However,

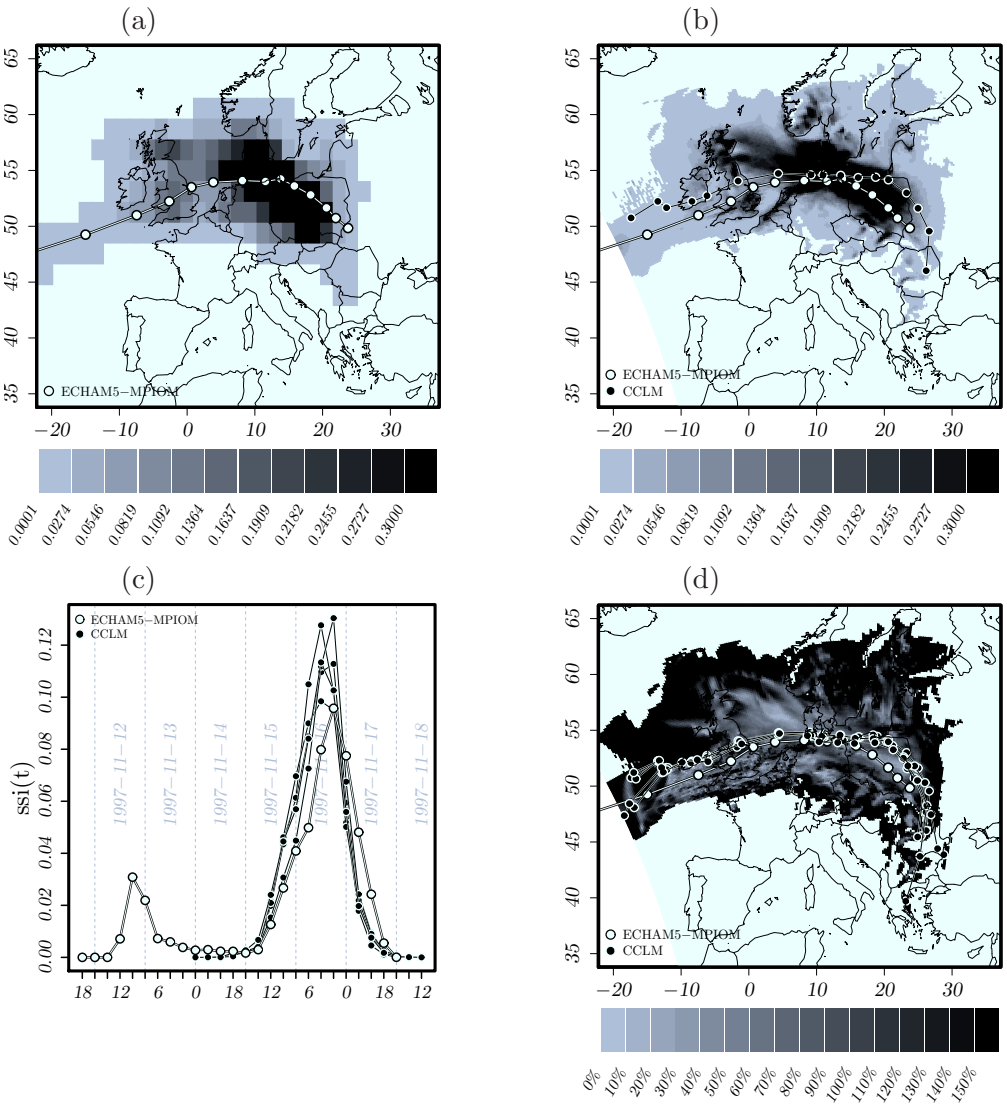

Figure 4.14: (a) Example storm system from MPI-ECHAM5 (run 1). Identified wind field track is lasting from 1997-11-11 18:00 till 1997-11-18 12:00. Total SSI value is 0.55, the SSI within the COSMO-CLM domain is 0.46. Shading represents the local storm severity as described by Equation 2.2. The wind field track (corresponding to the consecutive wind field centers) is shown as connected white points. (b) Local storm severity for the central realization of COSMO-CLM. The wind field track from MPI-ECHAM5 is shown in white connected points, comparing to the track from COSMO-CLM in grey. (c) Time decomposition of SSI. Shown in black circles are results from MPI-ECHAM5, and single members from COSMO-CLM are shown in grey. (d) Relative spread of the local storm severity (in %), spanned by the 5 member COSMO-CLM ensemble. Besides the wind field track from MPI-ECHAM5 (white connected points), resulting wind field tracks from the 5 simulations are shown in grey.

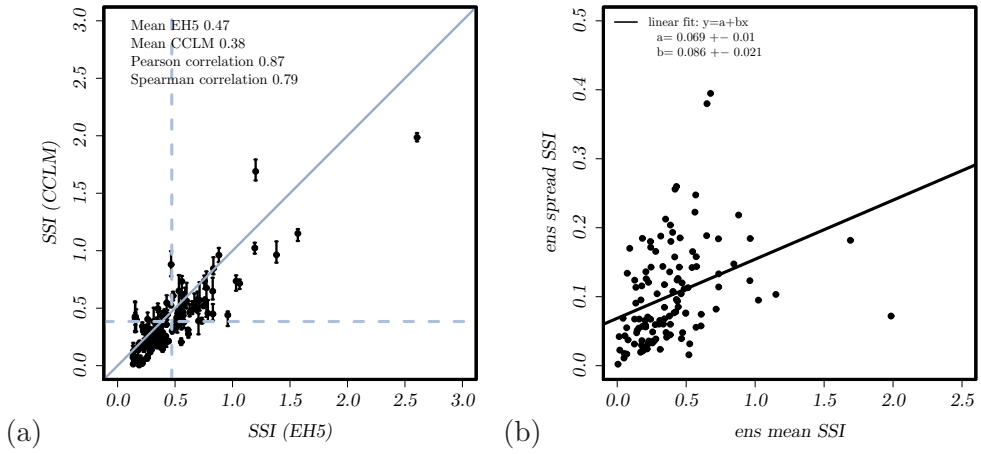

Figure 4.15: (a) SSI calculated from MPI-ECHAM5 versus COSMO-CLM. Points show COSMO-CLM ensemble mean and error bars indicate the spread spanned by the 5 member ensemble. (b) Ensemble mean SSI versus SSI spread spanned by COSMO-CLM ensemble.

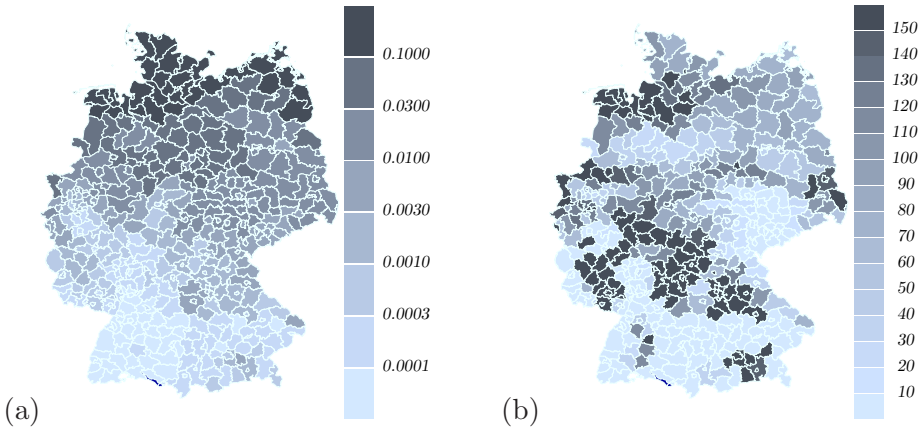

Figure 4.16: (a) Ensemble mean of modeled losses for the example in Figure 4.14. Shown is the sum of daily losses for the days 15th - 17th of November 1997. (b) Relative ensemble spread $100 \cdot (max - min)/mean$ *% of modeled losses on the days 15th - 17th of November 1997 for the example in Figure 4.14.*

relative spread is again largest for those regions in which uncertainty about their affectedness is present. Even though small in absolute terms, relative spread in these regions can raise well above 100%. The German wide loss ratio (ensemble mean) for the example in Figure 4.16a is 0.036‰, while the spread is 0.029‰ corresponding to a relative spread of 82%. In comparison, the relative spread in SSI (and thus in the meteorological hazard) calculated for the Germany region is only 23%. This shows, that the inhomogeneous distribution of insured values as well as locally varying vulnerabilities lead to an amplification of uncertainties in the meteorological hazard strength, which is affirmed when considering the relative spread for all 120 storm events shown in Figure 4.17a (gray histogram). Relative spread is found to be larger than 20% in most cases, with more than half of all simulations showing a spread larger than 50% and for nearly 25% of the events it raises above 100%.

4.6.4 Implications for Climate Change Assessment

To demonstrate the use of the presented technique in climate change impact studies, losses for the most severe winter storm events in future climate conditions (according to the SRES-A1B scenario (Nakicenovic et al., 2000)) are assessed. From historical loss records it can be found, that a large fraction of total wintertime losses is caused by few extreme winter storm events, the total loss ratio for the 30 most severe historical winter storm events accounting for a total loss ratio of 1.58‰ (compare Table 2 in Donat et al. (2011b)). Thus focus is put on the 30 most severe wind storm events in the period 1971-2000 (recent climate conditions) as well as the 3 scenario periods 2011-2040, 2041-2070 and 2071-2100. Regarding the single member COSMO-CLM simulations (central realization), total loss ratios for these periods are calculated to be 1.38‰, 1.91‰, 1.86‰and 2.29‰, respectively. As constructed, each of the 5 realizations of a storm events are physically consistent with no one being preferred over the other. Thus, to estimate the sum of losses any one of the 5 realizations for each of the 30 storm events can be randomly chosen. To estimate the downscaling uncertainty this random sampling is repeated 10000 times, from which the distribution of total losses can be derived. Resulting distributions for the 4 periods are shown in Figure 4.17. By this procedure, instead of specifying single estimates for each period, a range can be given using e.g. the quantiles including 90% of all sampled total losses. This can be calculated to be 1.21-1.61‰ in 1971-2000, 1.73-1.99‰ in 2011-2040, 1.74-1.95‰ in 2041-2070 and 2.12-2.34‰ in 2071-2100. Within the derived uncertainty range (1.21-1.61‰), the results for recent climate compare well with observed losses (1.58‰). For future climate conditions, total loss ratios are found significantly higher in all future scenario periods, with relative increases of +18% to +48% in 2011-2040, +18% to +43% in 2041-2070 and +45% to +70% in 2071-2100 compared to recent climate conditions.

	1971 – 2000	2011 – 2040	2041 – 2070	2071 – 2100
observed	1.58*	-	-	-
central	1.38	1.91 (+39%)	1.86 (+35%)	2.29 (+66%)
north	1.71	1.88 (+ 9%)	1.69 (-1%)	2.26 (+32%)
south	1.42	1.97 (+39%)	1.85 (+30%)	2.26 (+59%)
east	1.22	1.75 (+43%)	1.94 (+58%)	2.04 (+66%)
west	1.32	1.77 (+34%)	1.88 (+43%)	2.31 (+75%)
mean	1.41	1.86 (+32%)	1.84 (+31%)	2.23 (+58%)

*Table 4.2: Accumulated loss ratio (in ‰) for the 30 most severe winter storm episodes per each 30 year period calculated on the basis of the different COSMO-CLM realizations, each being shifted by 8 grid cells towards north, south, east and west compared to the central realization. * For observed losses, the 30 most severe winter storms in the 25 year period 1984-2008 are considered (data source: GDV, compare Donat et al. (2011b)).*

4.7 Estimates of Return Values for Loss Intensive Winter Storms

4.7.1 Return Values of Historical Winter Storms[2]

Extreme value analysis is applied to the loss data to determine the statistical characteristics of severe storm losses and to calculate statistical properties often used in insurance applications, e.g., the return periods of the storm events. Fitting the GPD to the VGV loss data involves large statistical uncertainties due to the small sample size. To permit a more accurate estimation of the extreme value statistics of storm losses, the loss dataset has been expanded to include times when storm losses to residential buildings were not yet recorded systematically. This is done on the basis of both VGV-Sim insurance records (see Section 4.3.1) and reanalysis wind data, and provides loss information back to 1948 when applying the refined loss model to NCEP reanalysis. The loss events are identified based on five day running sums of daily loss data.

Extraordinarily severe loss events occurred in early 1990, for example, storms “Daria“, “Vivian“ and “Wiebke“, and also in earlier decades in the second half of the 20th century. The most loss-intensive events in Germany during the recent 60 years identified here occurred in Jan 1976 (“Capella“), Nov 1972 (cyclone “Quimburga“, the “Lower Saxony Gale“) and Feb 1962 (a severe storm, causing a storm surge and leading to severe flooding in the city of Hamburg). Note that different reanalyses consistently suggest upward

[2]previously published in
Donat, M. G.; Pardowitz, T.; Leckebusch, G. C.; Ulbrich, U. und Burghoff, O. (2011b) High-resolution refinement of a storm loss model and estimation of return periods of loss-intensive storms over Germany. *Natural Hazards and Earth System Sciences*, 11, 2821-2833. The final publication is available at http://dx.doi.org/10.5194/nhess-11-2821-2011

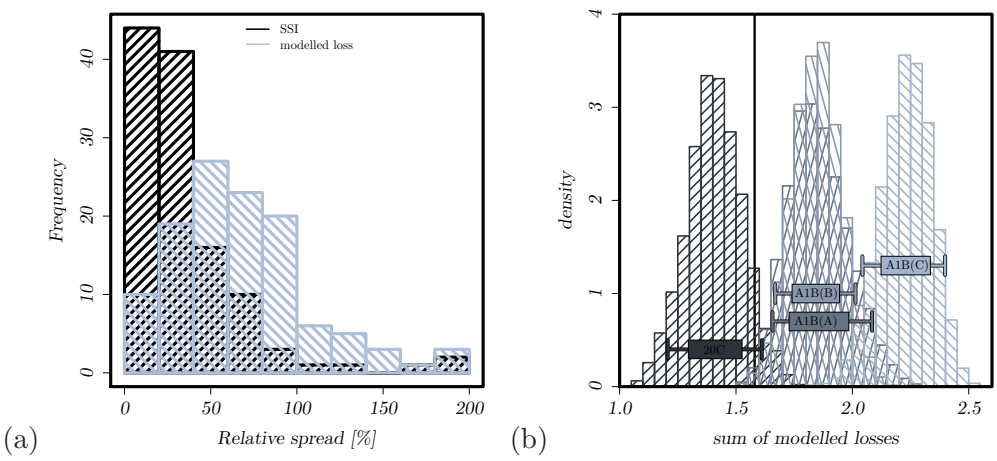

Figure 4.17: (a) Histograms of relative spread for the SSI values (black) as well as for the modeled German wide losses (grey). (b) Uncertainties in derived climate change signals. Histograms show density of sampled total sum of modeled losses of the 30 storms of each period. Each sampling is selecting 1 out of 5 realizations of each of the 30 storm systems. Sampling is repeated 10000 times. Box plots indicate the 66.7% and the 90% ranges for each of the periods 1971-2000, 2011-2040, 2041-2070 and 2071-2100. The vertical line indicates the accumulated loss ratio for the 30 most severe historical winter storms in the 25 year period 1984-2008.

trends in the occurrence of winter storms in Central Europe for the second half of the 20th century, and also since the late 19th century (Donat et al., 2011c).

A considerable socio-economic uncertainty, related to different spatial distributions of insured values, is apparent from the loss calculations based on NCEP. This effect is particularly strong for losses in earlier years. Cumulated losses for Germany were calculated using the spatial distribution of insured values (available for the years 1981 to 2007) of the specific year, or using the most recent available value distribution (year 2007). The distribution of insured values is used for weighting the local losses when calculating cumulated losses for Germany. For years prior to approximately 2000, however, these data are affected by a number of uncertainties related to lower insurance density or less detailed reporting of losses. The distribution of values may, therefore, not be representative for the earlier insurance data. For the eastern parts of Germany - the area of the former German Democratic Republic - insurance data are only available for years after 1990, and hence local losses are not accounted for when calculating cumulated losses for Germany. Furthermore, even for the other regions, information on insured values is only available back to 1981, and the value distribution of this year is, thus, also used when calculating cumulated losses in earlier years. Owing to the wide range of difficulties with the early insurance portfolio data, we decided to consider the cumulated losses using the most recent value distribution of the year 2007 for the extreme value analysis in this section. This

means that the insured values in the Landkreise remained constant for the NCEP-based return period estimation, which potentially distorts the cumulated losses in their historical context. These loss estimates indicate the losses that the historical storms would cause if they occurred under today's socio-economic conditions rather than the losses in their historical context, and describe a possibility to normalize the losses to a homogeneous portfolio. Also note the partly large differences between the NCEP and ERA-Interim based loss estimates for some individual events. These disparities reflect the differences in the realizations of these storms in the different reanalysis models and may partly also be related to the relatively coarse resolution of the NCEP model. On average, losses calculated from ERA-Interim showed a better agreement with insurance records for the period 1997-2007 compared to losses calculated from NCEP.

The extreme value analysis results in a return level plot combining the GPD fits for the different loss datasets 4.18. Although the sample sizes differ considerably and, in particular, the VGV insurance data are rather sparse with respect to a sound estimation of return periods, the curves for the different loss datasets agree remarkably well. The return levels are highest (lowest) for the insurance-data-based fits for VGV-Sim (VGV), flanking the curves for losses calculated from the two reanalysis datasets. The confidence intervals are narrowest for fits based on the long loss dataset calculated from NCEP reanalysis from 1948 to 2009. The good agreement between the different datasets suggests a high level of robustness of the return period estimates presented here.

The extreme value analysis of the different loss datasets reveals that the return period of storm "Kyrill" (the most severe event in the VGV data 1997-2007, Germany-wide accumulated loss ratio approximately 0.24‰) is 15 years (based on the GPD fit for the VGV-Sim data), 17 to 18 years (for losses calculated from both ERA-Interim and NCEP), and 21 years (VGV). The statistical uncertainty, expressed by the 95%confidence interval (Profile Log-Likelihood Method recommended by Coles, 2001) related to the GPD-fit of the NCEP based storm losses between 1948 and 2009, ranges between 9 and 43 years. The estimated return periods of the most loss-intensive storms since 1948 - "Capella" in 1976 (loss ratio calculated from NCEP using the most recent distribution of values: 0.476‰) and "Quimburga" in 1972 (NCEP loss ratio: 0.386‰) - range between 29 and 45 years in the different datasets (95% confidence interval between 15 and 145 years) for the first and 24 to 35 (95% confidence interval between 13 and 100 years) years for the second. Conversely, the expected Germany-wide loss ratio for a 10-year event ranges between 0.12‰ and 0.16‰ based on the fits for the different loss datasets (95% statistical confidence between 0.10‰ and 0.29‰), and for a 25-year loss event between 0.28‰ and 0.41‰ (95% confidence between 0.17‰ and 0.85‰). For losses related to a 50-year storm event, the different fits already display a considerable spread, the expected loss ratios range between 0.52‰ (VGV) and 0.85‰ (VGV Sim), and the statistical uncertainty

ranges from 0.26‰ to 1.93‰.

The shape parameter ξ is between approximately 0.8 and 1.0 for the different fits, indicating an unbounded distribution. In other words, this implies that, in theory, infinitely high losses may occur when using this statistical model. This scenario is, however, unrealistic because even when assuming total destruction of all buildings in the area considered, the total sum of values is finite. In the case of total destruction, a loss ratio equal to 1 would be expected. Note that the cumulated losses for the most destructive storm events in the past decades are in a co-domain of below approximately 0.5‰, i.e., only a small fraction of the total insured values. For losses in this dimension, the GPD fits for the different datasets display reasonable and stable results, thus, giving a certain amount of confidence in the return period estimation presented above.

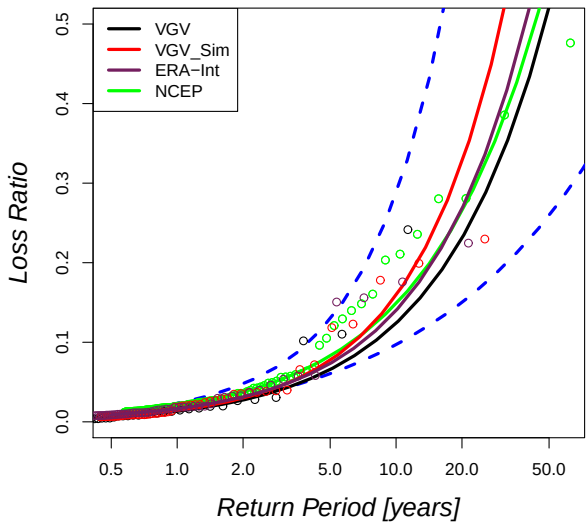

Figure 4.18: Return level plot (Return period in years against return levels in units of ‰) based on the different loss datasets. Historical VGV losses in black, VGV-Sim in red, modeled losses calculated on the basis of ERA-Interim gusts in purple and on the basis of NCEP in green. Points indicate the empirical distribution, the solid lines the GPD best fits and the blue dashed lines the 95% confidence interval based on the Profile-Log-Likelihood Method, as resulting from the fit based on modeled losses from NCEP.

4.7.2 Quantification of Uncertainties[3]

To assess the changes in return levels and return periods of high impact storm events under changed climate conditions, potentially damaging storm episodes are identified in the 3 run ensemble of MPI-ECHAM5 under recent (20C) and future climate conditions (SRES-A1B). These storm episodes are selected using the Storm Severity Index (SSI) as described in Section 2.2.4, calculated only for the grid boxes in MPI-ECHAM5 covering Germany. For each of the 4 periods 1971-2000 (20C) and 2011-2040, 2041-2070, 2071-2100 (A1B), the strongest 30 events, according to their SSI value, are chosen for downscaling. To assess the uncertainties involved in the modeling chain and resulting uncertainty ranges on estimates of return characteristics, the ensemble technique as presented in Section 4.6 is used to generate 5 member ensemble simulations for each of the selected storm episode. For each storm simulation, losses are modeled using the storm loss model as described in Section 4.4.2 and resulting German wide losses are calculated. These German wide losses are then analyzed using extreme value statistics (EVA) as outlined in Section 2.2.5 and uncertainties on resulting return values estimated. Three sources of uncertainty shall be quantitatively assessed, namely the dynamical downscaling uncertainty, the damage model uncertainty and the statistical uncertainty. Besides assessing these single uncertainties, their accumulation to cumulative uncertainty ranges shall be estimated. This is done in a Bootstrap framework as depicted in Figure 4.19. For a set of N storm episodes, multiple realizations are generated (a) through variations in the meteorology as well as (b) through variations in the storm-damage function. From these M realizations, one is selected for each storm episode within a single Bootstrap step. For each of such sampled set of realizations extreme value analysis is performed to derive return periods and return levels. Resulting distributions of return values can finally be used to derive uncertainty ranges by assessing the respective quantiles.

To quantify the uncertainties of the dynamical downscaling, the method described in Section 4.6 has been developed to modify in a simple manner the initial and boundary conditions of the high-resolved simulations. Through the slight shifts of the simulation domain, the 5 individual episode simulations are physically consistent and thus equally valid. By means of these dynamically downscaled ensemble simulations, the range resulting only from different simulation setup can be estimated. As discussed in Section 4.6, this range of course does not represent the total uncertainties which might origin also from other sources, such as parameterization and modeling uncertainties. The modeled Ger-

[3] previously published in
Held, H.; Gerstengarbe, F.-W.; Pardowitz, T.; Pinto, J. G.; Ulbrich, U.; Born, K.; Donat, M. G.; Karremann, M. K.; Leckebusch, G. C.; Ludwig, P.; Nissen, K. M.; Oesterle, H.; Prahl, B. F.; Werner, P. C.; Befort, D. J. und Burghoff, O. (2013) Projections of global warming-induced impacts on winter storm losses in the German private household sector. *Climatic Change*, 121, 195-207. The final publication is available at Springer via http://dx.doi.org/10.1007/s10584-013-0872-7

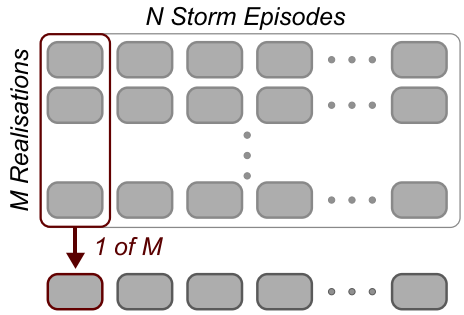

Figure 4.19: Schematic representation of the Bootstrap approach to assess uncertainties on return levels and return periods.

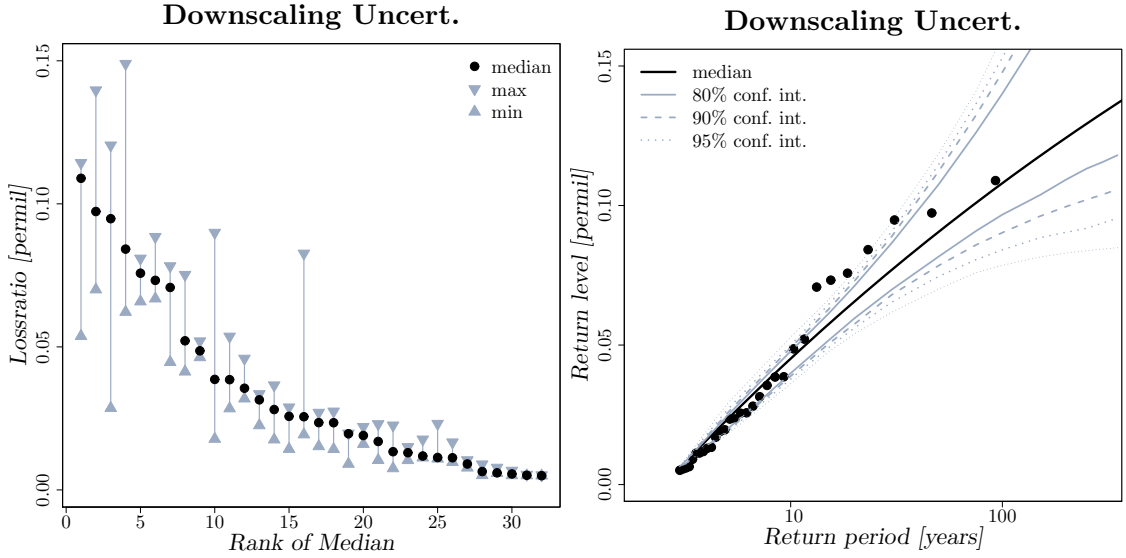

Figure 4.20: (left) Uncertainty range on modeled losses for the individual storm episodes spanned by the 5 member ensemble. The median of 5 realizations is shown in black dots, the minimum and maximum in grey triangles. (right) Derived uncertainty ranges on estimates of return levels. Uncertainty ranges are estimated using the Bootstrap methods (see text) with resulting 80%, 90% and 95% confidence intervals indicated in solid, dashed and dotted lines respectively.

man wide loss ratio for the 30 storm episodes re-simulated using COSMO-CLM from the 20C period are shown in Figure 4.20 (left). Black dots represent the median of modeled losses for each of the episodes, while min/max are indicated in grey. As was already shown in Section 4.6, the use of the ensemble approach generates different realizations of single storm episodes which (dependent on the individual episode) differ strongly in resulting losses. In the following it shall be investigated in how far these results can be used to infer uncertainties on derived return levels of high impact storms. If simulated in a single realization, the resulting loss ratio's were analyzed using a maximum likelihood fitting of

a Generalized Pareto Distribution (GPD, see Section 2.2.5 for details). To assess (and later on treat integratively) uncertainties from different sources on estimates of return levels, a Bootstrap scheme (Efron and Tibshirani, 1986) has been adopted. The basic setup of the Bootstrap scheme is depicted in Figure 4.19. The idea is, that for a single storm event, the resulting losses can be assigned with a range of values, e.g. depending on the individual simulation of the generated ensemble. Since the ensemble approach presented in Section 4.6 generates equally valid realizations, a random sample containing one realization of each of the simulated storm episodes (as depicted in the schematic Figure 4.19 with $M = 5$ and $N = 30$) is an equally valid set of loss ratios for which the extreme value analysis (EVA) can be performed. Thus 10000 such random sets are sampled, for which EVA is performed and resulting return levels obtained. For a specific return period the corresponding return level and its uncertainties can be assessed by calculating the respective median as well as the confidence intervals from the sampled distribution. Figure 4.20 (right) shows the resulting return level plot, where the black solid line indicates the median of the sampled return levels while different confidence intervals are shown in grey lines. Having estimated the uncertainties resulting from downscaling uncertainties in the

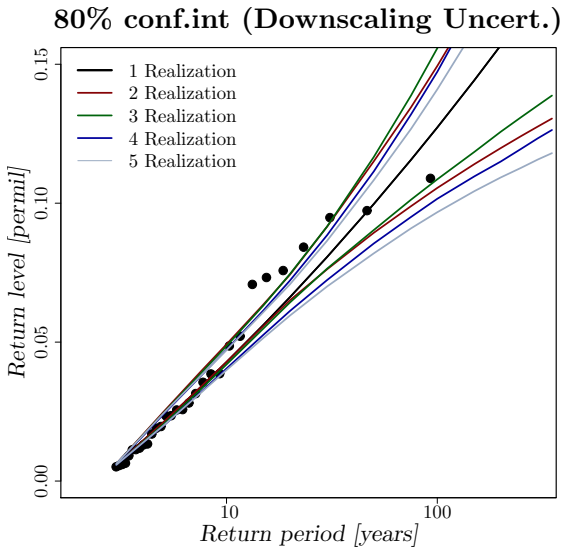

Figure 4.21: Dependence of the estimated uncertainty range on the size of the ensemble. Shown are the 80% confidence intervals when using 2, 3, 4 or 5 members (red, green, blue, grey lines respectively).

above described manner, the question remains, in how far results depend on the ensemble size. I.e. would the uncertainty range be larger if instead of 5 realizations a larger number had been simulated? To address this question, the uncertainty range is estimated using only $1 - 5$ of the simulated realizations and compared. Figure 4.21 shows resulting

80% confidence intervals, where the same bootstrap method as described above and as depicted in Figure 4.19 has been used. The black solid line shows the result if only the central realization is used (and no different samples can be generated). 80% confidence intervals, when using $M = 2, 3, 4, 5$ realizations are shown in red, green, blue and grey respectively. Interestingly it can be found, that the derived uncertainty ranges do not systematically grow with increasing ensemble size used. Already with 2 realizations of each storm episode, the uncertainty range on resulting return levels is well captured (which might not hold for individual storm episodes of course!). Thus it can be assumed, that with increasing ensemble sizes with more than the used 5 members, uncertainty ranges will not further increase. Thus it can be followed, that by the approach presented here, the downscaling uncertainty and resulting uncertainties on return levels is sufficiently captured.

Similarly to the quantification of uncertainties resulting from the dynamical downscaling, the uncertainties from the storm-damage function shall be quantified. The loss model as described in Section 4.4.2 has been trained using reanalysis data and observed losses for a set of 29 historical storms. To infer the uncertainty of the derived storm-damage function, the training of loss model is repeated each time leaving out one individual historical storm episode ("Leave one out approach"). In this fashion, 29 (slightly differing) sets of transfer functions per district are generated. Each of those loss models can be in turn used to infer modeled losses for the 20C simulations with loss ratios varying respectively. As before, Figure 4.22 shows the resulting range of modeled loss ratios for each of the simulated storm episodes of the 20C period. Resulting ranges of modeled losses are considerably, however smaller compared to the derived from the ensemble COSMO-CLM simulations. The same Monte Carlo Technique as described in the previous section is applied, sampling 10000 times (compare Figure 4.19, in this case with $M = 29$ and $N = 30$). For each randomly generated set of loss ratios again EVA is performed and return levels derived. Resulting confidence intervals (generated as described in the previous section) are shown in Figure 4.22. Comparing to uncertainties from dynamical downscaling, the uncertainties on derived return levels are found to be much smaller in this case. It needs to be noted however, that uncertainties from the storm damage model might be strongly underestimated. The "Leave one out" approach presented above might for example be altered to leave out 2 (or more) historical storm events each time to train the storm loss model. Resulting uncertainties might of course be larger in this case. The approach presented here can thus be interpreted as a sensitivity study (how might results alter if for example Kyrill had not occurred?) rather than resulting in estimates of "standard-errors". A correct approach to overcome this problem would be to perform a different Bootstrap approach, in which random set's of historical storms are chosen for training of the storm damage model. For each of these random trainings, storm losses were modeled for the

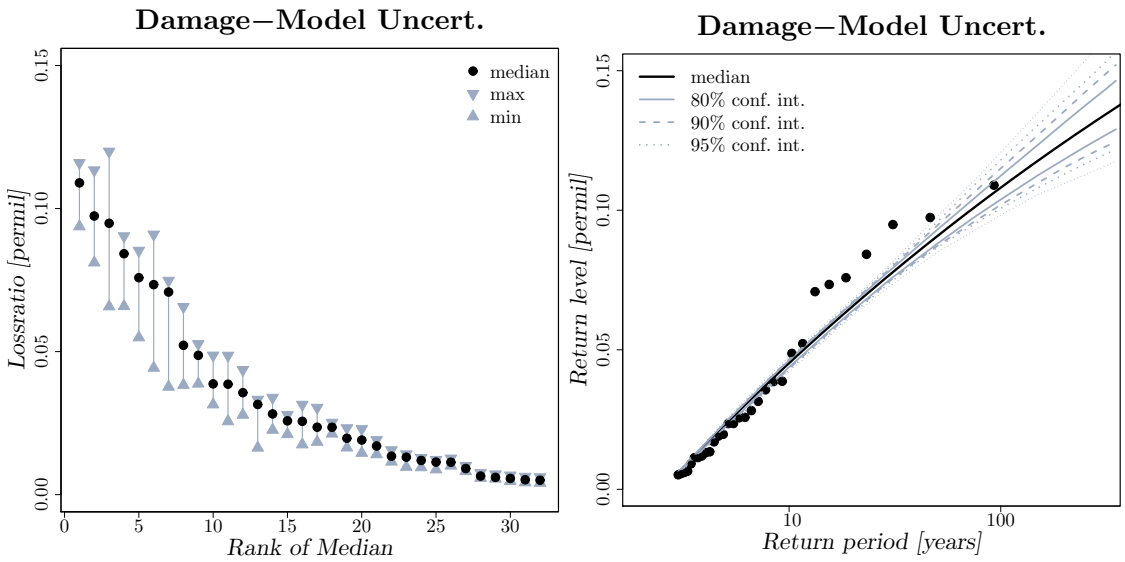

Figure 4.22: (left) Range of modeled losses for the individual storm episodes due to the uncertainties in the storm damage model. The median as shown in Figure 4.20 is shown in black dots, the minimum and maximum in grey triangles. (right) Derived uncertainty ranges on estimates of return levels. Uncertainty ranges are estimated using the Bootstrap methods (see text) with resulting 80%, 90% and 95% confidence intervals indicated in solid, dashed and dotted lines respectively.

episode simulations and than return level uncertainties estimated in the above described fashion. Since however in a Bootstrap approach, typical iteration steps should be 1000 or better 10000, this approach could not been conducted due to limited computing resources. In Held et al. (2013), an alternative approach has been presented additionally to assess the uncertainties resulting from the uncertainty in the storm damage function. It is based on the assumption, that the errors of the storm damage model that can be derived for individual historical storm events randomly occur when assessing losses from the simulated storm episodes under recent and future climate conditions. A suitable Bootstrap approach can thus be constructed based on sampling these random errors. This method was found to generate biases in estimates of return levels but furthermore shows, that uncertainties from storm damage modeling might considerably larger compared to the results presented above.

In the framework of the extreme value statistics (EVA) presented in Section 2.2.5, statistical uncertainties on estimates of return levels (and return periods) can be assessed. In the literature (compare e.g. Coles (2001)) two methods of assessing these uncertainties are discussed, the so called Delta-Method (based on the variance-covariance matrix resulting from the maximum likelihood fitting procedure) and the profile likelihood method (semi-analytical method which is able to asses also unsymmetrical uncertainty ranges). Especially in case of high return periods or high return levels, the later is recommended

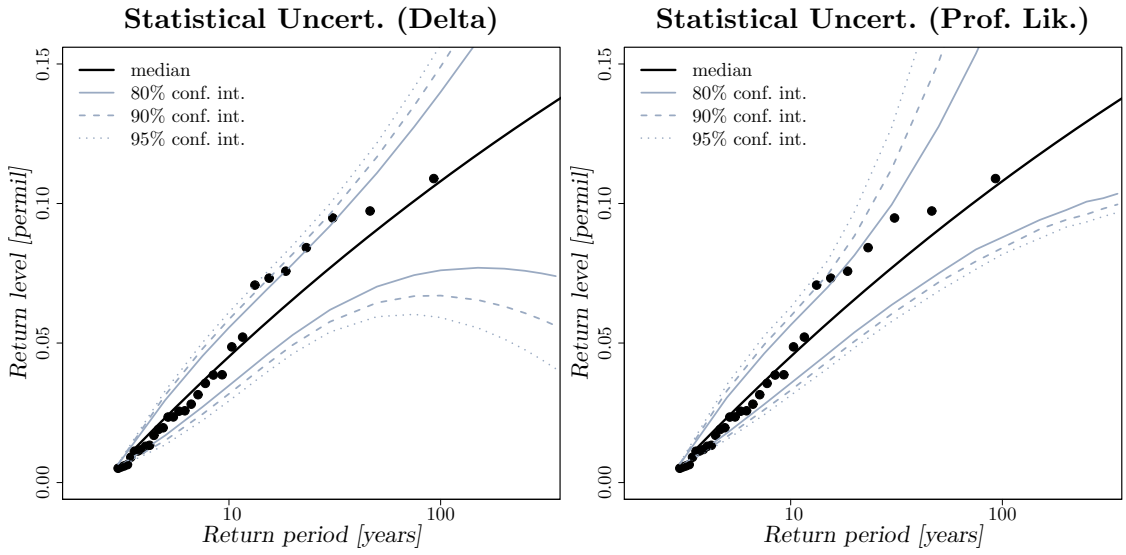

Figure 4.23: (left) Estimated statistical uncertainties using the delta method. 80%, 90% and 95% confidence intervals are indicated in solid, dashed and dotted lines respectively. (right) Same using the profile likelihood method.

since confidence intervals are usually found to be strongly asymmetric. For the German wide loss ratio calculated from the 20C storm episodes, Figure 4.23 shows derived confidence intervals (80%, 90% and 95%) for the Delta-Method (left) as well as the Profile Likelihood Method (right). In comparison estimated confidence intervals are in good agreement for smaller return periods ($< 25 years$), while for increasing return periods increasing disagreement is found. The symmetric confidence intervals derived using the delta-method tend to underestimate the lower bounds with unreasonable behavior for very large return periods (decreasing lower bounds for return periods $> 100 years$, which even extend to non-meaningful negative values for very high return periods). Also upper bounds are underestimated with the delta-method for high return periods ($> 25 years$).

The comparison of resulting 80% confidence intervals for the estimated return levels is shown in Figure 4.24 (left). It is found, that uncertainties from the storm-damage model are lowest amongst the three, while statistical uncertainties are largest. As noted above, uncertainties from storm-damage model might however be considerably larger. It might be of interest, to estimate resulting cumulative uncertainties, which is feasible within the presented Bootstrap method presented above (and depicted in Figure 4.19). The treatment of both downscaling and storm-damage model uncertainty is straightforward, now sampling 1 realization out of $M = 29 \cdot 5$ realizations of an individual storm event. These $29 \cdot 5$ realizations are generated, by applying one of the 29 different trainings of the storm-damage model from the "Leave-one-out" approach to one of the 5 members of the downscaling ensemble. To furthermore include the statistical uncertainties, the

range comprising 80% (90%,95% or 99%) of resulting 80% (90%,95% or 99%) confidence intervals for all of the generated Bootstrap samples are calculated.

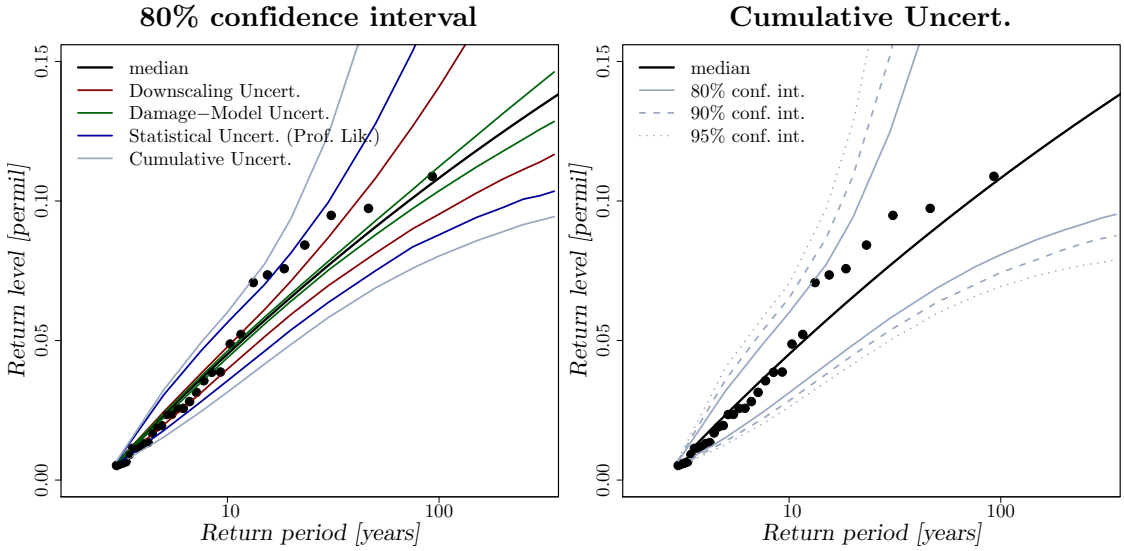

Figure 4.24: (left) Comparison of the estimated uncertainty ranges (80% confidence intervals) for the individual sources of uncertainty and the resulting cumulative uncertainty. (right) Resulting cumulative uncertainties for the 80%, 90% and 95% confidence intervals (solid, dashed and dotted respectively).

		Return Period		
		5 years	10 years	100 years
	Best estimate	**0.023‰**	**0.045‰**	**0.108‰**
80% conf. int.	Downscaling Uncert.	0.020‰|0.024‰	0.040‰|0.047‰	0.096‰|0.141‰
	Damage-Model Uncert.	0.022‰|0.024‰	0.044‰|0.046‰	0.104‰|0.112‰
	Statistical Uncert. (Prof. Lik.)	0.018‰|0.031‰	0.036‰|0.056‰	0.088‰|0.175‰
	Cumulative Uncert.	0.015‰|0.032‰	0.031‰|0.060‰	0.081‰|0.272‰
95% conf. int.	Downscaling Uncert.	0.019‰|0.026‰	0.038‰|0.050‰	0.084‰|0.152‰
	Damage-Model Uncert.	0.022‰|0.024‰	0.043‰|0.047‰	0.101‰|0.118‰
	Statistical Uncert. (Prof. Lik.)	0.016‰|0.035‰	0.031‰|0.063‰	0.082‰|0.280‰
	Cumulative Uncert.	0.013‰|0.040‰	0.026‰|0.070‰	0.069‰|0.658‰

Table 4.3: Estimated uncertainty ranges on return levels (in ‰) for different return periods.

4.7.3 Derived Climate Change Signal and its Uncertainties

For the periods 1971-2000 under recent climate conditions (20C) as well as for each of the 3 future periods (2011-2040, 2041-2070 and 2071-2100) under SRES-A1B scenario conditions (Nakicenovic et al., 2000) 30 storm episodes have been selected using the Storm Severity Index (SSI) calculated from MPI-ECHAM5 and downscaled using COSMO-CLM generating a 5 member ensemble for each episode. For each of the episodes, losses are modeled and for each periods the extreme value analysis including the estimation of cumulative uncertainty is performed in the manner described previously. Resulting return level plots indicating 80% confidence intervals are shown in Figure 4.25. Comparing the

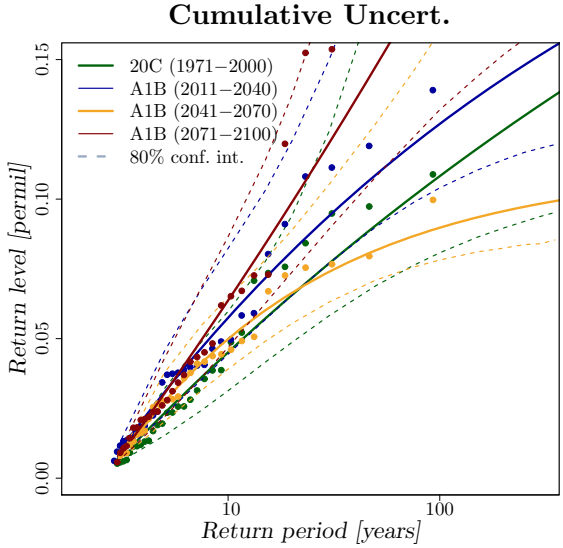

Figure 4.25: Return level plots including the cumulative uncertainty (80% confidence interval) for the recent climate period (green) as well as the future climate periods 2011-2040, 2041-2070 and 2071-2100 und SRES-A1B conditions (blue, yellow and red).

period 2011-2040 to the recent climate period, an increase in return levels associated with return periods between 5 and 100 years can be diagnosed. Considering the uncertainty ranges as listed in Table 4.4 it is found, that in this period the lower 80% confidence interval is roughly equal to the best estimates derived for the recent climate period. The following period 2041-2070 shows slightly decreasing return values associated with return periods shorter than 25 years, while a stronger decrease is found for high return periods. For these extremes (where naturally variability is high - expressed by large statistical uncertainties) for this period thus a decrease in return levels is found, even when comparing to recent climate conditions. For the end of the 21st century, again an increase in return levels is found throughout the investigated range of return periods. The increase when comparing to recent climate accounts for roughly 30% for moderate

return periods (5 years), raising to an increase of roughly 75% for events occurring once in 100 years. It is found that for return periods smaller than 25 years all future climate periods show increased return levels, with lower 80% confidence intervals exceeding (or being close to) the values derived for recent climate. Having estimated the cumulative uncertainty including the downscaling uncertainty, the uncertainty arising in the storm damage modeling as well as the statistical uncertainties this provides confidence in the result that the amount of losses due to severe winter storms might strongly increase under future climate conditions. For higher return periods, the large uncertainties indicate that derived increases are less confident. Natural climate variability hinders the robust detection of climate change signals for such rare events especially when considering a base period of 90 (3x30) years length as it was done here. These natural variability manifests e.g. in a strong decrease of 100 year return level in the period 2041-2070 followed by an steep increase afterwards. This variability is present of course also for smaller return periods (where sample sizes are naturally larger), however less distinct. Similar

	Return Period		
	5 years	10 years	100 years
20C (1971-2000)	0.015‰|**0.023**‰|0.032‰	0.031‰|**0.045**‰|0.060‰	0.081‰|**0.108**‰|0.272‰
A1B (2011-2040)	0.023‰|**0.031**‰|0.046‰	0.044‰|**0.058**‰|0.082‰	0.104‰|**0.127**‰|0.270‰
A1B (2041-2070)	0.020‰|**0.027**‰|0.038‰	0.039‰|**0.050**‰|0.065‰	0.079‰|**0.090**‰|0.159‰
A1B (2071-2100)	0.022‰|**0.030**‰|0.043‰	0.047‰|**0.064**‰|0.087‰	0.132‰|**0.187**‰|0.361‰

Table 4.4: Estimated return levels in ‰and cumulative uncertainties according to the 80% confidence intervals for recent and future climate periods under SRES-A1B conditions.

to return levels for fixed return periods, the changes in return periods themselves can be assessed in the framework of the extreme value analysis. The cumulative uncertainties are assessed similarly to the approach presented above and results are presented in table 4.5. Consistent to the increases in return levels, results indicate a shortening of return periods of loss intensive storm events. For an initially 5 year event, return periods decrease to about 4.3 years with 80% confidence intervals ranging from 3.7 to 5.2 years at the end of the 21st century. Similarly shortening of longer return periods is found; a 10 year event is found to occur once in 6.8 (5.2-9.5) years, a 100 year event with a return period of 24 (14-50) years. Such events occurring once a century might thus occur about 4 times a century. The natural variability, which affects especially the statistics of the rarest events however indicate the large uncertainties inherent with these estimates. E.g. in the period from 2041-2070, such extreme events were not sampled which result in immensely high return periods of more than 1000 years for an initially 100 year event. Expressed by the even larger uncertainty ranges for this estimate it can be followed however, that these

estimates are not reliable since even a decrease of the return period to about 30 years is indicated to lay within the 80% confidence range.

	Return Period		
	5 years	10 years	100 years
A1B (2011-2040)	3.5|**4.2**|5.1	5.0|**7.2**|10.2	16| **49**| 129
A1B (2041-2070)	3.9|**4.5**|5.6	5.9|**8.5**|12.7	31|**1230**|2634
A1B (2071-2100)	3.7|**4.3**|5.2	5.2|**6.8**| 9.5	14| **24**| 50

Table 4.5: Estimated return periods in units of years and corresponding cumulative uncertainties according to the 80% confidence intervals for recent and future climate periods under SRES-A1B conditions.

4.8 Summary and Discussion

Compared to the changes in the European storm climate on large scales discussed in Chapter 2, the assessment of trends in storm related losses is associated with much larger uncertainty, which beside the large statistical uncertainty result from multiple uncertainty sources along the modeling chain, including particularly the uncertainties inherent in the modeling of wind storm damages based on gust estimates. A high resolution storm damage model has been presented (see 4.4.2 and Donat et al. (2011b)). The framework presented allows the modeling of local differences in vulnerabilities by deriving storm damage functions based on historical loss experiences on district basis. It has been shown, that estimation of linear regression coefficients are subjected to large uncertainties due to a limited data basis. A method has been proposed to reduce these uncertainties by groping together districts exhibiting similar storm-damage relationships. The method has been shown to conserve spatial differences in resulting regression parameters, however using a much smaller set of free parameters which need to be estimated. As a results of this procedure, highly reduced uncertainties on estimated regression coefficients are found.

Using this high resolution storm loss model, in Section 4.5 regional patterns of changes in future winter storm losses have been investigated. Considering the ensemble mean of 12 analyzed regional climate projections, German wide losses are found to increase by +14% (+8%) in 2071-2100 (2021-2050) under SRES-A1B scenario conditions compared to recent climate conditions. These findings compare well to results presented by Donat et al. (2011a) finding loss potentials for Germany to increase by +15% (+5%). respectively. Furthermore, losses are found to increase disproportionately in western and northern Germany, where an increase of up to 30% in yearly storm losses is found, whereas results indicate only moderate changes for southern and eastern regions of Germany. Uncertainties inherent to these estimates which result from the loss modeling uncertainties

are found to be considerably. For German wide losses, an uncertainty range for the derived changes between +7% and +20% is found. The uncertainty range is found to be considerably smaller, when considering the optimized loss model as presented in Section 4.4.3. By grouping districts featuring similar storm-loss relationships, uncertainties on estimated coefficients are significantly reduced, leading to much smaller uncertainties on estimated losses. Using the optimized version of the loss model, derived change signals for German wide losses can be confined to range between +11% and +14%. Compared to these uncertainties the resulting ensemble uncertainties are found to be large. For German wide losses, changes for mean losses in 2071-2100 compared to 1971-2000 range between a decrease of -14% (ensemble minimum) and an increase by +39% (ensemble maximum). Regional changes are subjected to even larger uncertainty ranges as indicated by Figure 4.11.

Results by Schwierz et al. (2010) and Pinto et al. (2012) indicate, that impacts imposed by rare winter storm events in Europe and Germany might increase disproportionately in a future climate compared to mean annual losses. However, the statistical data basis to derive changes in the impacts of such extreme winter storm events are often weak. To improve the statistics of rare extremes it is thus favorable to incorporate ensemble techniques to enlarge the data base Sasse and Schädler (2013). In Section 4.6 a method has been presented to assess uncertainty information from high resolution downscaling simulations for high impact weather. For a set of severe winter storms identified in the global climate model ECHAM5-MPIOM, an ensemble technique has been applied to generate physically equivalent realizations of high resolution RCM simulations. The approach is justified by the fact that the model domain is to a certain degree a random choice. Thus different simulation domains are chosen, each shifted with respect to a reference domain by a small number of 8 grid cells in each direction. The proposed ensemble method is particularly appealing, since it is easy implementable and since it is generating physically consistent ensemble members. The setup should thus be distinguished from ensemble forecast generation methods, which aim to estimate the effects of variations in physics and in modifying the initial conditions with specific anomalies (compare e.g. Palmer et al. (2007)). Sasse and Schädler (2013) presented a similar yet different approach, called the Atmospheric Forcing Shifting (AFS) method, where the atmospheric forcing fields are shifted with respect to the model orography by an amount of 25 (50) km. Even though Sasse and Schädler (2013) do not find systematic differences which may result from systematically shifted weather patterns, the physical consistency of ensemble members is not strictly given for the AFS method over orography. However, similar to the method presented in this study, the AFS method presents a way to assess the high sensitivity to slight modifications in the boundary conditions. For a set of winter storm episodes it was shown, that the small changes in the lateral boundary conditions introduced by shifting

of the simulation domain lead to changes in the areas affected by high wind speeds as well as changes in the intensity of individual storm systems simulated by the regional model. It was demonstrated that this can lead to considerable ensemble spread in a storms potential impact due to the high sensitivity of impacts with extreme wind speeds. In more than half of the conducted winter storm episode simulations the relative spread exceeds 25% compared to the ensemble mean. These changes in the synoptic development of the storm systems amplify to large ensemble spread when deriving losses by applying a winter storm loss model to the regional model output. The relative spread of derived losses raises above 50% compared to the ensemble mean for half of the simulated wind storm systems. A large part of this increase in ensemble spread can be attributed to high spatial variations in the distribution of values as well as local variations in vulnerabilities to high winds. The method was shown to be useful to estimate downscaling uncertainties in climate change impact studies when using a fixed GCM/RCM model combination (in this study MPI-ECHAM5 and COSMO-CLM), since enabling the specification of uncertainty ranges for derived values as well as derived climate change signals. As noted before, such uncertainty information will certainly enhance the usefulness of high resolution model simulations (Wu et al., 2005), especially for improving the statistics of (rare) extreme values (Sasse and Schädler, 2013). Findings indicate the usefulness of such an approach especially for extreme weather impact studies involving high sensitivities to the precise local meteorological conditions. The method can thus easily be applied to other impact studies where small changes in the location and intensity of low pressure systems might strongly influence conditions leading to flooding (e.g. coastal flooding investigations). Also it might be applicable for river flooding studies, where slight changes e.g. in the location of meteorological systems might strongly alter possible impacts.

For recent climate conditions (20C), the total loss ratio of the 30 most severe storm systems is estimated to range between 1.2‰ and 1.6‰ (90% confidence interval, compare Table 4.2), which compares well to the total loss of 1.58‰ realized through the 30 most severe historical winter storms (compare Table 2 in Donat et al. (2011b)). For future scenario periods, increases are found to range between +18% to +48%, +18% to +43% and +45% to +70% for the periods 2011-2040, 2041-2070 and 2071-2100, respectively compared to recent climate conditions (1971-2000). It needs to be noted, that these result are derived using a fixed GCM/RCM model combination and a fixed set of 30 winter storm episodes identified in MPI-ECHAM5 output within the four investigated 30 year periods. This fixed set of episodes predetermine the climate change signal derived in this study. Comparing to changes in mean annual losses, which were found to increase by about +14% (with an ensemble range of -14% to +39%) towards the end of the 21st Century, it is thus confirmed by these results, that high impact storm events might disproportionately increase in strength (Schwierz et al., 2010).

Based on the high resolution ensemble simulations of the identified storm episodes, changes in return levels and return periods of future severe winter storms have been assessed in Section 4.7. Here, a special focus has been put on the estimation of associated uncertainties. To assess uncertainties a framework has been developed in which uncertainties resulting from multiple sources can be treated integratively to derive cumulative uncertainty ranges. Explicitly treated sources of uncertainty are dynamical downscaling uncertainties (assessed using the ensemble technique described in Section 4.6), the storm-damage function uncertainties as well as the statistical uncertainties (treated within the extreme value analysis framework). For the end of the 21st century, return levels of a 5 year loss event are found to change by about +30% with a cumulative uncertainty range of -5% to 87%. For loss events with higher return periods even larger increase rates are found. A 10 (100) year event is found to increase in strength by 42% (73%) with uncertainty ranges of +5 to 93% (+22% to 243%) respectively. The results are in agreement with findings by Schwierz et al. (2010) which derived changes in the impact of severe storm events in Europe by analyzing 3 regional climate projections following the SRES-A2 scenario. For European-wide loss events, they estimated losses of a 10 year event to increase by 23%, and a 100 year event by 104%. Consistently it has been found that changes in return periods are depending on the rareness of the considered event (Pinto et al., 2012). While for events with short return periods (1-10 years) only small shortening (or even elongation) of return periods is found for potential loss events in Germany, rare events with return periods of 100 years in recent climate are found to occur once in 35 years in future climate conditions according to SRES-A1B scenario conditions. The results presented in Section 4.7 confirm these findings, with return periods of a 5 year event decreasing to 4.3 years with a cumulative uncertainty range estimated to 3.7 to 5.2 years. For a 100 year event, return periods are found to shorten to 24 years with an uncertainty range between 14 and 50 years towards the end of the 21st century respectively.

The approaches presented in this Chapter are subjected to a range of limitations, including several sources of uncertainties being neglected or being only partly addressed. Firstly, the loss model is based on the assumption that losses are depending on the cubic exceedance of the 98th percentile of local wind speeds, supported by several empirical studies (Klawa and Ulbrich, 2003; MunichRe, 1993; Palutikof and Skellern, 1991; Lamb, 1991). However, loss evaluations performed by MunichRe (2002) after the storm series of 1999 suggested higher exponents (v^4 to v^5) in the storm loss function, showing that serious objections to this assumption can be made and that such coefficients may be rather different if based on other sources of loss data. Long term changes in local wind conditions might thus translate into changes of losses systematically deviating from the results presented here. It can be assumed, that if higher exponents than v^3 were used to model storm damages, changes in future losses may be even more severe since an increase

in extreme winds should be expected to scale with a higher order respectively. Secondly a major limitation of the approach chosen is that parameters describing vulnerability towards severe winds are assumed to be constant and equal to present state conditions. Even though future changes in values in a specific district (by changes in population densities or growth) might not affect results since relative measures for losses such as the loss ratio were considered, socio-economic developments such as autonomous or regulatory adaptation measures may fundamentally alter the underlying vulnerabilities. Simple assumptions on the influence of adaptive measures to changed climate conditions (basically modeled through a changed loss occurrence threshold according to the 98th percentile in the future climate) show considerable benefits with respect to storm loss potentials (Leckebusch et al., 2007; Pinto et al., 2007), however vulnerability changes will certainly be much more complex than modeled in these studies.

Chapter 5

Synthesis

Based on global climate model output, possible changes in potentially hazardous winter storm events over Europe and associated uncertainties have been investigated. It is found, that fundamental changes in frequency as well as intensity of European winter storms are projected towards the end of the 21st century in agreement with previous studies. It is found, that a general decrease in the frequency of severe storms is found particularly over northern parts of the North-Atlantic and southern parts spanning the Azores and the Mediterranean. For a band across the North Atlantic -the typical path of storm systems under present climate conditions- increases in the occurrence frequencies are diagnosed combined with increased severity of systems particularly over northern, central and eastern parts of Europe.

Three future emission scenarios, proposed in the special report on emission scenarios (SRES, (IPCC, 2000)), with differing assumptions on the development of economy, technology and population have been evaluated. From the A1 storyline, the SRES-A1B scenario has been evaluated which assumes a future world of strong economic growth, a global population peaking in mid-century and a fast introduction of new and efficient technologies with a balanced use of fossil and non-fossil energy sources. The SRES-A2 storyline describes a very heterogeneous world with a strongly increasing global population and economic development which is regionally oriented and in which technological change is slower. The SRES-B1 scenario family describes a convergent world with global population as in the A1 storyline, but with rapid changes in economic structures towards reduced material intensity, the introduction of clean and resource-efficient technologies and an emphasis on global solutions to economic, social and environmental sustainability. In terms of global carbon dioxide (CO_2), the SRES-B1 scenarios assumes moderate increases of emissions to about 11 GtC/yr in the middle of the 21st century declining thereafter. Within A1B, stronger increases in emissions to about 16 GtC/yr are assumed to be reached in mid-century, decreasing within the second half of the 21st century as in SRES-B1. Within the A2 scenario, similar emission increases are assumed in the first half of the 21st century, while emissions are assumed to further increase during the second half to about 30 GtC/yr. Evaluation of emissions within the recent past indicated that global CO_2 emissions exceeded most of even the more pessimistic scenarios within the early 21st century (Le Quere et al., 2009). Recent observed trends in CO_2 concentrations tend to

be in the middle of the scenarios used for the projections (IPCC, 2013), which is however only partly the case for concentrations of other climate sensitive greenhouse gases. While reliable measures of CO_2 concentrations exist, large uncertainties are attached even to the estimates of past emissions, which are related to unknowns in the uptake by land and ocean CO_2 sinks (Le Quere et al., 2009). Even though the range of future greenhouse gas emissions as represented by the SRES story lines has been considered undisputed (van der Linden et al., 2009) particularly with respect to which are most likely scenarios, objections can be made to whether the analyzed scenarios span the full range of possible emission pathways.

With respect to frequency and intensity of future winter storms in Europe, robust change patterns are found amongst those scenarios, with strongest changes towards the end of the 21st century identified for the SRES-A2 scenario, intermediate changes in SRES-A1B and less pronounced changes in SRES-B1. For central Europe and Germany, frequencies are found to increase from about 5 severe storm systems per year in recent climate to about 6 per year in SRES-A1B, to about 6.1 per year in SRES-A2 and to 5.8 per year in SRES-B1. Intensities of storm events affecting central Europe and Germany having a return period of 1 year are found to increase in strength by about +10% to +18% in SRES-A1B, +8% to +25% in SRES-B1 and −1% to +19% in SRES-A2 (compare Table 2.4), with large uncertainties attached to these estimates. While large scale features of diagnosed changes of severe storm climatology show distinct dependence of the underlying scenario, e.g. the strength of decrease in track density around the Azores and increase in track density over central and eastern Europe being strongest in SRES-A2 and weakest in SRES-B1 (compare Figure 2.9), on local or regional scales considerable variations occur due to internal climate variability. This holds particularly for the estimated changes in rare storm events, where statistical uncertainties are obviously much larger. Different global climate models from the ENSEMBLES project (van der Linden et al., 2009) were found to differ with respect to their representation of European winter storm climate. All considered models are able to reproduce the general patterns of track density from reanalysis data under recent climate conditions. However, considerable variations with respect to the location of main storm paths, the spatial coherence of storm paths as well as their absolute frequencies are found, leading to rather large differences in diagnosed change patterns. In all 8 model simulations analyzed under SRES-A1B conditions, the general pattern of decreasing track densities over the Azores, Iceland and Greenland and increasing track densities over central and eastern Europe is identified, with however strong modifications with respect to the strength of individual parts of this pattern. For central Europe and Germany, this leads to a rather large spread in projected changes of winter storm occurrence frequency ranging from a decrease by −11% (IPSL-CM4) to an increase of +44% (FUB-EGMAM) with 7 out of 8 models projecting an increased winter storm

frequency. While statistical uncertainties can be significantly reduced when considering multiple GCM projections, with internal variabilities of individual model simulations being at least partly canceled out in the respective ensemble mean, inter model differences due to differing model formulations, model resolutions and differing model response to prescribed GHG concentration changes can be identified as being one of the major uncertainty involved in the assessment of future wind storm climate. However it needs to be noted that it is not at all trivial, attributing inter model differences to be caused by either model differences, differing model response to changed GHG concentrations or internal variability.

To understand the underlying mechanisms of the diagnosed changes in European winter storm climate and to discriminate them from random internal variability, factors influencing the genesis of intense cyclones and related wind storms have been investigated. The close relation of intense winter storms over Europe and the North Atlantic Oscillation (NAO) has been investigated, finding that considerable changes in the NAO are projected consistent amongst the multi model ensemble. These changes are not restricted to simple shifts of the NAO towards more positive phases, but include crucial changes in the oscillation pattern with both northern and southern action centers being shifted in north-eastward direction in the future projections. The model response in terms of increased storm frequencies over Europe are found to be related and consistent to both changes in the NAO phase and it's shape. While a shift towards more positive phases of the NAO would generally lead to increased storm frequencies over northern parts of Europe and decreased frequencies over the Mediterranean, the eastward shift of the action centers can be related to the distinct increases in storm activity over the eastern parts of Europe. Furthermore the baroclinicity of the atmosphere under future climate conditions has been assessed and is found to be strongly related to the changes in European storm activity. The baroclinic instability zone over the Northern Atlantic is found to extend in eastward direction leading to particularly large increases in upper tropospheric baroclinicity over central and eastern Europe. These changes can explain the fact, that cyclones forming over the North Atlantic travelling towards Europe can further intensify and reach further east before dissipating their energy, leading to more intense storm systems especially over eastern Europe. Considering zonally averaged baroclinicity, it is found that the mid latitude baroclinic instability zone is generally intensifying and shifting poleward and extending upwards related to increased and northward shifted jet streams. Cyclonic systems embedded in this enhanced westerly background flow might thus take up additional energy converting it into rotational energy, but also surface wind speeds might be enhanced by the increased background flow due to the superposition of geostrophic wind components with increased system velocities. Considering the NAO as a manifestation of a stationary Rossby wave forming through the overtopping flow of the Rocky Moun-

tains gave further insight to the diagnosed changes of the NAO and it's relationship to large scale circulation dynamics in the tropics. It was found, that the northward shift and intensification of the jet streams and baroclinic instability zone are closely related to the extent of the tropical Hadley cell, which is expanding under future climate conditions pushing poleward jet streams and baroclinic instability zone. Increased overtopping velocities over the Rocky Mountains in turn causes substantial changes in the characteristics of the orography induced stationary Rossby wave. Theoretical considerations on the characteristics of the lee wave trough of such Rossby waves were able to explain the diagnosed eastward shifts of the NAO action centers, indicating that long-term variations in the NAO might be explained by variations in the upper tropospheric westerly background flow, which have been related to the Hadley cell dynamics. This gives further weight to recent findings that long term changes of the NAO might be indirectly forced by the tropics (Selten et al., 2004; Hurrell et al., 2004; Hoerling et al., 2004) giving further insight about the dynamical mechanisms involved in this teleconnection. Particularly in light of decadal predictability, the identified dynamical mechanisms and the tropical influence on the NAO and European storm climate can be of great relevance. Advances in the model's capabilities and predictive skill with respect to the tropical circulation might thus lead to significant gain in skill regarding predictions of low-frequency variations in European storm climate.

While changes in European storm climate can be quantified by means of large global climate model ensemble projections with robust results regarding large scale features which can furthermore be related to fundamental changes in the atmospheric circulation, trends in regional or local storm climatologies are associated with much larger uncertainties. To resolve the physical processes relevant for wind climatologies on small scales, including small-scale orographic effects and physical processes related e.g. to convective motion, requires model simulations on much higher resolution than represented by state of the art GCMs. Even though great advance in computing power has lead to the availability of highly resolved regional climate model projections, sample sizes especially for rare severe events are still limited. Estimates of future storm impacts, which critically depend on local wind conditions, are thus largely subjected to uncertainties arising from the lack of availability of large high-resolution ensembles. In this work, an approach has been developed to make use of an ensemble generation technique (Section 4.6) to enhance the benefit of regional climate models in downscaling applications, particularly focusing on the usage for estimating severe weather impacts. Identifying periods of severe weather conditions from projections with coarse resolution and generating ensemble simulations using COSMO-CLM has been demonstrated to supply enlarged statistical sample sizes offering the possibility to quantify uncertainties involved in the projections of future winter storm losses in Germany with strongly reduced computing capacities. Furthermore

an approach has been developed combining these uncertainties with uncertainties resulting from the modeling of wind induced losses and the statistical uncertainties resulting from extreme value analysis. Return levels and return periods as well as the associated uncertainty ranges for future loss intense winter storms have been quantified using this approach. Results indicated, that the return level of an event occurring once in 5 years increase by about +30% in terms of losses, with a cumulative uncertainty range of -5% to 87%. For loss events with higher return periods even larger increase rates can be identified, of course with correspondingly larger uncertainty ranges.

Long term averages of winter storm losses in Germany under changed climate conditions according to an ensemble of RCM projections following the SRES-A1B scenario are found to increase by about +14% towards the end of the 21st century. Uncertainties inherent to these estimates which result from loss modeling uncertainties related to limited availability of data on historical losses are found to be considerable. Making optimal use of historical loss data, an optimized version 4.4.3 of a high resolution loss model (Donat et al., 2011b) has been developed being able to represent local characteristics in vulnerability and exposure, however minimizing modeling uncertainties by grouping districts featuring similar relations between wind and loss. For changes in German wide losses, the uncertainty range can be found to be reduced from [+7%,+20%] for the original model to [+11%,+14%] using the optimized model. Individual model simulations from an ensemble of regional climate projections however show, that large uncertainties remain with respect to changes in regional wind climatologies. Inter model spread indicates that changes in German wide losses might even decrease by about -14% (indicated by the ensemble minimum) and increase by up to +39% (ensemble maximum), since results even if based on 30 year periods might depend crucially on a small set of extremely loss intense storm systems. Losses are found to increase disproportionately in western and northern Germany, where an ensemble mean increase of up to 30% is found, whereas results indicate only moderate changes for southern and eastern regions of Germany. With increased spatial discrimination, the associated uncertainties are found to strongly increase, hindering robust estimates e.g. for trends on district level. However on regional scales (e.g. using an aggregation on Bundesländer level), projected changes in losses can be distinctively discriminated with higher confidence for losses to increase in northern and western parts of Germany.

There is high confidence that the impacts of severe weather events have already been increasing over the past decades (IPCC, 2012) with evidences for an increased storminess over the past decades (Donat et al., 2011c). Even though projections of the impacts of future winter storms have been shown to be associated with large uncertainties, results presented in this work imply that impacts of severe winter storms in Germany are likely to further increase during the 21st century due to an increase in both their number as

well as their intensity. However, the main driver of changes in economic losses from weather- and climate- related disasters has not been considered in this work, namely changes with respect to the exposure of people and economic assets, which has been identified as the major driver for recent increases in severe weather impacts (IPCC, 2012). Results presented in this work might thus be strongly underestimating the consequences of an enhanced storm activity over Europe. It will certainly be of great interest for future research to be able to quantify the complex interplay of changed climatic conditions and societal changes affecting the exposure and vulnerability towards natural hazards.

Bibliography

Angermann, A. (1993) Sturmszenarien und Schadenhäufigkeit von Stürmen über Deutschland. Master thesis. Institut für Geophysik und Meteorologie der Universität zu Köln. (Cited on page 85.)

Baehr, C.; Pouponneau, B.; Ayrault, F.; and Joly, A. (1999) Dynamical characterization of the FASTEX cyclogenesis cases. *Quarterly Journal of the Royal Meteorological Society* 125(561), 3469–3494. (Cited on page 45.)

Barnston, A. G. and Livezey, R. E. (1987) Classification, Seasonality and Persistence of Low-frequency Atmospheric Circulation Patterns. *Monthly Weather Review* 115(6), 1083–1126. (Cited on page 48.)

Bengtsson, L.; Semenov, V. A.; and Johannessen, O. M. (2004) The early twentieth-century warming in the Arctic - A possible mechanism. *Journal of Climate* 17(20), 4045–4057. (Cited on pages 68 and 72.)

Bengtsson, L.; Hodges, K. I.; and Roeckner, E. (2006) Storm tracks and climate change. *Journal of Climate* 19(15), 3518–3543. (Cited on pages 2, 9 and 43.)

Born, K.; Ludwig, P.; and Pinto, J. G. (2012) Wind gust estimation for Mid-European winter storms: towards a probabilistic view. *Tellus A* 64(17471). (Cited on page 100.)

Bott, A. (2012) *Synoptische Meteorologie: Methoden der Wetteranalyse und -prognose.* (Cited on page 46.)

Böhm, U.; Keuler, K.; Österle, H.; Kücken, M.; and Hauffe, D. (2008) Quality of a climate reconstruction for the CADSES regions. *Meteorologische Zeitschrift* 17(4), 477–485. (Cited on page 101.)

Chang, C. B.; Perkey, D. J.; and Kreitzberg, C. W. (1984) Latent-heat Induced Energy Transformations During Cyclogenesis. *Monthly Weather Review* 112(2), 357–367. (Cited on page 45.)

Christensen, J. H.; Christensen, O. B.; Lopez, P.; van Meijgaard, E.; and Botzet, M. (1996) The HIRHAM4: Regional atmospheric climate model. DMI Scientific Report 96–4. (Cited on page 84.)

Coles, S.G. (2001) *An Introduction to Statistical Modeling of Extreme Values.* Springer, London. (Cited on pages 15, 18 and 115.)

Davies, H. C. (1976) A lateral boundary formulation for multi-level prediction models. *Quarterly Journal of the Royal Meteorological Society* 102, 405–418. (Cited on page 101.)

Davies, H. C. (1983) Limitations of Some Common Lateral Boundary Schemes used in Regional NWP Models. *Monthly Weather Review* 111, 1002. (Cited on page 101.)

Dee, D. P.; Uppala, S. M.; Simmons, A. J.; Berrisford, P.; Poli, P.; Kobayashi, S.; Andrae, U.; Balmaseda, M. A.; Balsamo, G.; Bauer, P.; Bechtold, P.; Beljaars, A. C. M.; van de Berg, L.; Bidlot, J.; Bormann, N.; Delsol, C.; Dragani, R.; Fuentes, M.; Geer, A. J.; Haimberger, L.; Healy, S. B.; Hersbach, H.; Holm, E. V.; Isaksen, L.; Kallberg, P.; Koehler, M.; Matricardi, M.; McNally, A. P.; Monge-Sanz, B. M.; Morcrette, J. . J.; Park, B. . K.; Peubey, C.; de Rosnay, P.; Tavolato, C.; Thepaut, J. . N.; and Vitart, F. (2011) The ERA-Interim reanalysis: configuration and performance of the data assimilation system. *Quarterly Journal of the Royal Meteorological Society* 137(656), 553–597. (Cited on pages 11, 47 and 83.)

Della-Marta, P. M. and Pinto, J. G. (2009) Statistical uncertainty of changes in winter storms over the North Atlantic and Europe in an ensemble of transient climate simulations. *Geophysical Research Letters* 36, L14703. (Cited on pages 9, 10 and 43.)

Della-Marta, P. M.; Mathis, H.; Frei, C.; Liniger, M. A.; Kleinn, J.; and Appenzeller, C. (2008) The return period of wind storms over Europe. *International Journal Of Climatology* 29(3, Sp. Iss. SI), 437–459. (Cited on pages 10, 18, 41 and 42.)

DIN (2005) DIN 1055-4:2005-03, Windbelastung von Bauwerken. (Cited on pages 86 and 93.)

Doblas-Reyes, F. J.; Deque, M.; Valero, F.; and Stephenson, D. B. (1998) North Atlantic wintertime intraseasonal variability and its sensitivity to GCM horizontal resolution. *Tellus A* 50(5), 573–595. (Cited on page 42.)

Doms, G. (2011) A Description of the Nonhydrostatic Regional COSMO-Model - Part I: Dynamics and Numerics. Technical report. Consortium for Small-Scale Modelling. (Cited on pages 101 and 102.)

Donat, M. G.; Leckebusch, G. C.; Pinto, J. G.; and Ulbrich, U. (2010a) Examination of wind storms over Central Europe with respect to circulation weather types and NAO phases. *International Journal of Climatology* 30(9), 1289–1300. (Cited on pages 9, 46 and 73.)

Donat, M. G.; Leckebusch, G. C.; Pinto, J. G.; and Ulbrich, U. (2010b) European storminess and associated circulation weather types: future changes deduced from a

multi-model ensemble of GCM simulations. *Climate Research* 42(1), 27–43. (Cited on pages 2 and 43.)

Donat, M. G.; Leckebusch, G. C.; Wild, S.; and Ulbrich, U. (2011a) Future changes in European winter storm losses and extreme wind speeds inferred from GCM and RCM multi-model simulations. *Natural Hazards and Earth System Science* 11(5), 1351–1370. (Cited on pages 44, 80, 81, 83, 101 and 120.)

Donat, M. G.; Pardowitz, T.; Leckebusch, G. C.; Ulbrich, U.; and Burghoff, O. (2011b) High-resolution refinement of a storm loss model and estimation of return periods of loss-intensive storms over Germany. *Natural Hazards and Earth System Sciences* 11 (10), 2821–2833. (Cited on pages 4, 31, 82, 87, 106, 107, 120, 122 and 129.)

Donat, M. G.; Renggli, D.; Wild, S.; Alexander, L. V.; Leckebusch, G. C.; and Ulbrich, U. (2011c) Reanalysis suggests long-term upward trends in European storminess since 1871. *Geophysical Research Letters* 38, L14703. (Cited on pages 2, 108 and 129.)

Dorland, C.; Tol, R. S. J.; and Palutikof, J. P. (1999) Vulnerability of the Netherlands and Northwest Europe to storm damage under climate change - A model approach based on storm damage in the Netherlands. *Climatic Change* 43(3), 513–535. (Cited on page 79.)

Efron, B. and Tibshirani, R. (1986) Bootstrap Methods for Standard Errors, Confidence Intervals, and Other Measures of Statistical Accuracy. *Statistical Science* 1(1), pp. 54–75. (Cited on page 113.)

Etienne, C. and Beniston, M. (2012) Wind storm loss estimations in the Canton of Vaud (Western Switzerland). *Natural Hazards and Earth System Sciences* 12(12), 3789–3798. (Cited on page 81.)

Fink, A. H.; Bruecher, T.; Ermert, V.; Krueger, A.; and Pinto, J. G. (2009) The European storm Kyrill in January 2007: synoptic evolution, meteorological impacts and some considerations with respect to climate change. *Natural Hazards and Earth System Sciences* 9(2), 405–423. (Cited on page 1.)

Forest, C. E.; Stone, P. H.; Sokolov, A. P.; Allen, M. R.; and Webster, M. D. (2002) Quantifying uncertainties in climate system properties with the use of recent climate observations. *Science* 295(5552), 113–117. (Cited on page 100.)

Furevik, T.; Bentsen, M.; Drange, H.; Kindem, I. K. T.; Kvamsto, N. G.; and Sorteberg, A. (2003) Description and evaluation of the bergen climate model: ARPEGE coupled with MICOM. *Climate Dynamics* 21(1), 27–51. (Cited on page 11.)

GDV (2007) Solvency II und Rückversicherung. Gesamtverband der Deutschen Versicherungswirtschaft e.V. URL http://www.gdv.de/wp-content/uploads/2007/05/sII_reinsurance.pdf. (Cited on page 78.)

Gillett, N. P.; Zwiers, F. W.; Weaver, A. J.; and Stott, P. A. (2003) Detection of human influence on sea-level pressure. *Nature* 422(6929), 292–294. (Cited on page 46.)

Held, H.; Gerstengarbe, F.-W.; Pardowitz, T.; Pinto, J. G.; Ulbrich, U.; Born, K.; Donat, M. G.; Karremann, M. K.; Leckebusch, G. C.; Ludwig, P.; Nissen, K. M.; Oesterle, H.; Prahl, B. F.; Werner, P. C.; Befort, D. J.; and Burghoff, O. (2013) Projections of global warming-induced impacts on winter storm losses in the German private household sector. *Climatic Change* 121(2), 195–207. (Cited on page 115.)

Hoerling, M. P.; Hurrell, J. W.; and Xu, T. Y. (2001) Tropical origins for recent North Atlantic climate change. *Science* 292(5514), 90–92. (Cited on page 3.)

Hoerling, M. P.; Hurrell, J. W.; Xu, T.; Bates, G. T.; and Phillips, A. S. (2004) Twentieth century North Atlantic climate change. Part II: Understanding the effect of Indian Ocean warming. *Climate Dynamics* 23(3-4), 391–405. (Cited on pages 47, 75 and 128.)

Hofherr, T. and Kunz, M. (2010) Extreme wind climatology of winter storms in Germany. *Climate Research* 41(2), 105–123. (Cited on pages 10 and 41.)

Holton, J. R. (2004) *An Introduction to Dynamic Meteorology*. Academic Press. (Cited on page 68.)

Hoskins, B. J. and Valdes, P. J. (1990) On the Existence of Storm-tracks. *Journal of the Atmospheric Sciences* 47(15), 1854–1864. (Cited on pages 45, 49 and 55.)

Huebener, H.; Cubasch, U.; Langematz, U.; Spangehl, T.; Niehorster, F.; Fast, I.; and Kunze, M. (2007) Ensemble climate simulations using a fully coupled ocean-troposphere-stratosphere general circulation model. *Philosophical Transactions of the Royal Society A* 365(1857), 2089–2101. (Cited on page 11.)

Hurrell, J. W. (1995) Decadal Trends In the North-atlantic Oscillation - Regional Temperatures and Precipitation. *Science* 269(5224), 676–679. (Cited on page 48.)

Hurrell, J. W.; Hoerling, M. P.; Phillips, A. S.; and Xu, T. (2004) Twentieth century North Atlantic climate change. Part 1: assessing determinism. *Climate Dynamics* 23 (3-4), 371–389. (Cited on pages 3, 47 and 128.)

IPCC (2000) *Special Report on Emission Scenarios*. Cambridge University Press. (Cited on page 125.)

IPCC (2007a) *Climate Change 2007: The Physical Science Basis. Contribution of Working Group I to the Fourth Assessment Report of the Intergovernmental Panel on Climate Change*. Cambridge University Press, Cambridge, UK, 996 pp. (Cited on page 1.)

IPCC (2007b) *Climate Change 2007: Impacts, Adaptation and Vulnerability. Contribution of Working Group II to the Fourth Assessment Report of the Intergovernmental Panel on Climate Change*. Cambridge University Press, Cambridge, UK, 976pp. (Cited on pages 1 and 4.)

IPCC (2012) *Managing the Risks of Extreme Events and Disasters to Advance Climate Change Adaptation. A Special Report of Working Groups I and II of the Intergovernmental Panel on Climate Change*. Cambridge University Press, Cambridge, UK, and New York, NY, USA, 582 pp. (Cited on pages 2, 3, 129 and 130.)

IPCC (2013) *Climate Change 2013: The Physical Science Basis. Contribution of Working Group I to the Fifth Assessment Report of the Intergovernmental Panel on Climate Change*. Cambridge University Press, Cambridge, United Kingdom and New York, NY, USA, 1535 pp. (Cited on pages 2, 3 and 126.)

Jacob, D. and Podzun, R. (1997) Sensitivity studies with the regional climate model REMO. *Meteorology and Atmospheric Physics* 63(1-2), China Meteorol Adm; World Meteorol Org. (Cited on page 84.)

Jaeger, E. B.; Anders, I.; Luthi, D.; Rockel, B.; Schar, C.; and Seneviratne, S. I. (2008) Analysis of ERA40-driven CLM simulations for Europe. *Meteorologische Zeitschrift* 17 (4), 349–367. (Cited on page 84.)

Johannessen, O. M.; Bengtsson, L.; Miles, M. W.; Kuzmina, S. I.; Semenov, V. A.; Alekseev, G. V.; Nagurnyi, A. P.; Zakharov, V. F.; Bobylev, L. P.; Pettersson, L. H.; Hasselmann, K.; and Cattle, A. P. (2004) Arctic climate change: observed and modelled temperature and sea-ice variability. *Tellus A* 56(4), 328–341. (Cited on pages 68, 72 and 74.)

Johanson, C. M. and Fu, Q. (2009) Hadley Cell Widening: Model Simulations versus Observations. *Journal of Climate* 22(10), 2713–2725. (Cited on page 50.)

Jones, R. G.; Murphy, J. M.; and Noguer, M. (1995) Simulation of Climate-change Over Europe Using A Nested Regional-climate Model Part 1. Assessment of Control Climate, Including Sensitivity To Location of Lateral Boundaries. *Quarterly Journal of the Royal Meteorological Society* 121(526), 1413–1449. (Cited on page 84.)

Jungclaus, J. H.; Keenlyside, N.; Botzet, M.; Haak, H.; Luo, J. J.; Latif, M.; Marotzke, J.; Mikolajewicz, U.; and Roeckner, E. (2006) Ocean circulation and tropical variability in

the coupled model ECHAM5/MPI-OM. *Journal of Climate* 19(16), 3952–3972. (Cited on page 11.)

Kjellström, E.; Bärring, L.; Gollvik, S.; Hansson, U.; Jones, C.; Samuelsson, P.; Rummukainen, M.; Ullerstig, A.; Willen, U.; and Wyser, K. (2005) A 140-year simulation of European climate with the new version of the Rossby Centre regional atmospheric climate model (RCA3). Reports Meteorology and Climatology, 108, SMHI. (Cited on page 84.)

Klawa, M. and Ulbrich, U. (2003) A model for the estimation of storm losses and the identification of severe winter storms in Germany. *Natural Hazards and Earth System Science* 3(6), 725–732. (Cited on pages 4, 13, 79, 80, 81, 85 and 123.)

Knippertz, P.; Ulbrich, U.; and Speth, P. (2000) Changing cyclones and surface wind speeds over the North Atlantic and Europe in a transient GHG experiment. *Climate Research* 15(2), 109–122. (Cited on page 9.)

Kunz, M.; Mohr, S.; Rauthe, M.; Lux, R.; and Kottmeier, Ch. (2010) Assessment of extreme wind speeds from Regional Climate Models - Part 1: Estimation of return values and their evaluation. *Natural Hazards and Earth System Sciences* 10, 907–922. (Cited on pages 10 and 41.)

Lamb, H. H. (1991) *Historic Storms of the North Sea, British Isles and Northwest Europe.* Cambridge Press. (Cited on pages 79, 85 and 123.)

Lambert, S. J. and Fyfe, J. C. (2006) Changes in winter cyclone frequencies and strengths simulated in enhanced greenhouse warming experiments: results from the models participating in the IPCC diagnostic exercise. *Climate Dynamics* 26(7-8), 713–728. (Cited on page 9.)

Le Quere, C.; Raupach, M. R.; Canadell, J. G.; Marland, G.; Bopp, L.; Ciais, P.; Conway, T. J.; Doney, S. C.; Feely, R. A.; Foster, P.; Friedlingstein, P.; Gurney, K.; Houghton, R. A.; House, J. I.; Huntingford, C.; Levy, P. E.; Lomas, M. R.; Majkut, J.; Metzl, N.; Ometto, J. P.; Peters, G. P.; Prentice, I. C.; Randerson, J. T.; Running, S. W.; Sarmiento, J. L.; Schuster, U.; Sitch, S.; Takahashi, T.; Viovy, N.; van der Werf, G. R.; and Woodward, F. I. (2009) Trends in the sources and sinks of carbon dioxide. *Nature Geoscience* 2(12), 831–836. (Cited on pages 125 and 126.)

Leckebusch, G. C. and Ulbrich, U. (2004) On the relationship between cyclones and extreme windstorm events over Europe under climate change. *Global and Planetary Change* 44(1-4), 181–193. (Cited on page 2.)

Leckebusch, G. C.; Koffi, B.; Ulbrich, U.; Pinto, J. G.; Spangehl, T.; and Zacharias, S. (2006) Analysis of frequency and intensity of European winter storm events from a multi-model perspective, at synoptic and regional scales. *Climate Research* 31(1), 59–74. (Cited on pages 9 and 43.)

Leckebusch, G. C.; Ulbrich, U.; Froehlich, L.; and Pinto, J. G. (2007) Property loss potentials for European midlatitude storms in a changing climate. *Geophysical Research Letters* 34(5), L05703. (Cited on pages 79, 80, 81 and 124.)

Leckebusch, G. C.; Renggli, D.; and Ulbrich, U. (2008) Development and application of an objective storm severity measure for the Northeast Atlantic region. *Meteorologische Zeitschrift* 17(5), 575–587. (Cited on pages 9, 12, 13, 41, 42, 73 and 84.)

Legutke, S. and Voss, R. (1999) The Hamburg atmosphere-ocean coupled circulation model ECHO-G. Technical Report 18. German Climate Computer Centre (DKRZ). (Cited on page 11.)

Lenderink, G.; van den Hurk, B.; van Meijgaard, E.; van Ulden, A.; and Cujipers, H. (2003) Simulation of present-day climate in RACMO2: first results and model developments. KNMI Technical Report, 252, 24. (Cited on page 84.)

Liberato, M. L. R.; Pinto, J. G.; Trigo, R. M.; Ludwig, P.; Ordonez, P.; Yuen, D.; and Trigo, I. F. (2013) Explosive development of winter storm Xynthia over the subtropical North Atlantic Ocean. *Natural Hazards and Earth System Sciences* 13(9), 2239–2251. (Cited on page 60.)

Lindzen, R. S. and Farrell, B. (1980) A Simple Approximate Result For the Maximum Growth-rate of Baroclinic Instabilities. *Journal of the Atmospheric Sciences* 37(7), 1648–1654. (Cited on pages 49 and 55.)

Lu, J.; Vecchi, G. A.; and Reichler, T. (2007) Expansion of the Hadley cell under global warming. *Geophysical Research Letters* 34(6), L06805. (Cited on pages 45, 47, 50, 62, 64 and 74.)

Lunkeit, F.; Ponater, M.; Sausen, R.; Sogalla, M.; Ulbrich, U.; and Windelband, M. (1996) Cyclonic Activity in a Warmer Climate. *Beitraege zur Physik der Atmosphaere* 69(3), 393–407. (Cited on pages 46, 55, 56 and 73.)

Manzini, E. and McFarlane, N. A. (1998) The effect of varying the source spectrum of a gravity wave parameterization in a middle atmosphere general circulation model. *Journal of Geophysical Research* 103(D24), 31523–31539. (Cited on page 11.)

Marshall, J.; Kushner, Y.; Battisti, D.; Chang, P.; Czaja, A.; Dickson, R.; Hurrell, J.; McCartney, M.; Saravanan, R.; and Visbeck, M. (2001) North Atlantic climate variability: Phenomena, impacts and mechanisms. *International Journal of Climatology* 21(15), 1863–1898. (Cited on page 47.)

Marti, O.; Braconnot, P.; Bellier, J.; Benshila, R.; et al. (2005) The new IPSL climate system model: IPSL-CM4. Note 26. IPSL Global Climate Modeling Group. (Cited on page 11.)

Mitas, C. M. and Clement, A. (2005) Has the Hadley cell been strengthening in recent decades? *Geophysical Research Letters* 32(3), L030809. (Cited on pages 50 and 62.)

Montani, A.; Capaldo, M.; Cesari, D.; Marsigli, C.; Modigliani, U.; Nerozzi, F.; Paccagnella, T.; Patruno, P.; and Tibaldi, S. (2003) Operational limited-area ensemble forecasts based on the 'Lokal Modell'. Technical Report No. 98. (Cited on page 100.)

MunichRe (1993) Winterstürme in Europa. Münchener Rückversicherungs-Gesellschaft. (Cited on pages 79, 85 and 123.)

MunichRe (1999) Naturkatastrophen in Deutschland: Schadenerfahrungen und Schadenpotentiale. Münchener Rückversicherungs-Gesellschaft. URL `www.munichre.com/publications/302-01037_de.pdf`. (Cited on pages 1 and 9.)

MunichRe (2002) Winter Storms in Europe (III) Analysis of loss potentials. (Cited on page 123.)

MunichRe (2007) Zwischen Hoch und Tief - Wetterrisiken in Mitteleuropa. Münchener Rückversicherungs-Gesellschaft. URL `www.munichre.com/publications/302-05481_de.pdf`. (Cited on page 9.)

MunichRe (2012) GeoRisikoForschung, NatCatSERVICE, Stand Januar 2012. URL `http://www.munichre.com/de/reinsurance/business/non-life/natcatservice/index.html`. (Cited on page 1.)

Nakicenovic, N.; Alcamo, J.; and Davis, G. (2000) *Emission Scenarios, A Special Report of Working Group III of the Intergovernmental Panel on Climate Change*. Cambridge University Press, Cambridge, U. K. (Cited on pages 12, 25, 48, 78, 80, 83, 106 and 118.)

Nissen, K. M.; Leckebusch, G. C.; Pinto, J. G.; Renggli, D.; Ulbrich, S.; and Ulbrich, U. (2010) Cyclones causing wind storms in the Mediterranean: characteristics, trends and links to large-scale patterns. *Natural Hazards and Earth System Sciences* 10(7), 1379–1391. (Cited on pages 41 and 73.)

O'Gorman, P. A. (2010) Understanding the varied response of the extratropical storm tracks to climate change. *Proceedings of the National Academy of Sciences of the United States of America* 107(45), 19176–19180. (Cited on page 3.)

Oort, A. H. and Yienger, J. J. (1996) Observed interannual variability in the Hadley circulation and its connection to ENSO. *Journal of Climate* 9(11), 2751–2767. (Cited on pages 50, 62 and 64.)

Osborn, T. J. (2004) Simulating the winter North Atlantic Oscillation: the roles of internal variability and greenhouse gas forcing. *Climate Dynamics* 22(6-7), 605–623. (Cited on page 46.)

Paciorek, C. J.; Risbey, J. S.; Ventura, V.; and Rosen, R. D. (2002) Multiple indices of Northern Hemisphere cyclone activity, winters 1949-99. *Journal of Climate* 15(13), 1573–1590. (Cited on pages 49 and 55.)

Palmer, T. N.; Buizza, R.; Leutbecher, M.; Hagedorn, R.; Jung, T.; Rodwell, M.; Vitart, F.; Berner, J.; Hagel, E.; Lawrence, A.; Pappenberger, F.; Park, Y-Y.; von Bremen, L; and Gilmour, I. (2007) The Ensemble Prediction System - Recent and Ongoing Developments. Technical Memorandum 540. European Centre for Medium Range Weather Forecasts. Paper presented to the 36th Session of the SAC, 8-10 Oct 2007. (Cited on pages 100 and 121.)

Palutikof, J. P. and Skellern, A. R. (1991) Storm Severity over Britain, A Report to Commercial Union General Insurance. Report. Climatic Research Unit, School of Environmental Sciences, University of East Anglia, Norwich (UK). (Cited on pages 79, 85 and 123.)

Pardowitz, T.; Befort, D. J.; Leckebusch, G. C.; and Ulbrich, U. (2014) Estimating uncertainties from high resolution simulations of extreme wind storms and consequences for impacts. *Submitted to Meteorologische Zeitschrift*. (Not cited.)

Pinto, J. G. and Raible, C. C. (2012) Past and recent changes in the North Atlantic oscillation. *Wiley Interdisciplinary Reviews* 3(1), 79–90. (Cited on pages 3, 46, 48 and 49.)

Pinto, J. G.; Froehlich, E. L.; Leckebusch, G. C.; and Ulbrich, U. (2007) Changing European storm loss potentials under modified climate conditions according to ensemble simulations of the ECHAM5/MPI-OM1 GCM. *Natural Hazards and Earth System Science* 7(1), 165–175. (Cited on pages 12, 80, 81 and 124.)

Pinto, J. G.; Zacharias, S.; Fink, A. H.; Leckebusch, G. C.; and Ulbrich, U. (2008) Factors contributing to the development of extreme North Atlantic cyclones and their

relationship with the NAO. *Climate Dynamics* 32(5), 711–737. (Cited on pages 45, 46, 56, 57 and 73.)

Pinto, J. G.; Neuhaus, C. P.; Leckebusch, G. C.; Reyers, M.; and Kerschgens, M. (2010) Estimation of wind storm impacts over Western Germany under future climate conditions using a statistical-dynamical downscaling approach. *Tellus A* 62A, 188–201. (Cited on page 81.)

Pinto, J. G.; Karremann, M. K.; Born, K.; Della-Marta, P. M.; and Klawa, M. (2012) Loss potentials associated with European windstorms under future climate conditions. *Climate Research* 54(1), 1–20. (Cited on pages 81, 121 and 123.)

Pinto, J. G.; Bellenbaum, N.; Karremann, M. K.; and Della-Marta, P. M. (2013) Serial clustering of extratropical cyclones over the North Atlantic and Europe under recent and future climate conditions. *Journal of Geophysical Research* 118(22), 12476–12485. (Cited on page 1.)

Prahl, B. F.; Rybski, D.; Kropp, J. P.; Burghoff, O.; and Held, H. (2012) Applying stochastic small-scale damage functions to German winter storms. *Geophysical Research Letters* 39, L06806. (Cited on page 79.)

Renggli, D.; Leckebusch, G. C.; Ulbrich, U.; Gleixner, S. N.; and Faust, E. (2011) The Skill of Seasonal Ensemble Prediction Systems to Forecast Wintertime Windstorm Frequency over the North Atlantic and Europe. *Monthly Weather Review* 139(9), 3052–3068. (Cited on page 42.)

Rockel, B.; Will, A.; and Hense, A. (2008) The Regional Climate Model COSMO-CLM(CCLM). *Meteorologische Zeitschrift* 17(4), 347–348. (Cited on page 84.)

Roeckner, E.; Lautenschlager, M.; and Schneider, H. (2006) IPCC-AR4 MPI-ECHAM5 T63L31 MPI-OM GR1.5L40. Technical report. (Cited on page 101.)

Salas-Melia, D.; Chauvin, F.; Deque, M.; Douville, H.; Gueremy, J. F.; Marquet, P.; Planton, S.; Royer, J. F.; and Tyteca, S. (2005) Description and validation of the CNRM-CM3 global coupled model. Technical Report 103. Meteo-France, 42 Avenue Gaspard Coriolis, 31057 Toulouse Cedex, France. (Cited on page 11.)

Samuelsson, Patrick; Jones, Colin G.; Willen, Ulrika; Ullerstig, Anders; Gollvik, Stefan; Hansson, Ulf; Jansson, Christer; Kjellstrom, Erik; Nikulin, Grigory; and Wyser, Klaus. (2011) The Rossby Centre Regional Climate model RCA3: model description and performance. *Tellus A* 63(1), 4–23. (Cited on page 84.)

Sasse, R. and Schädler, G. (2013) Generation of regional climate ensembles using Atmospheric Forcing Shifting. *International Journal of Climatology* pages n/a–n/a. (Cited on pages 100, 121 and 122.)

Schultz, D. M.; Keyser, D.; and Bosart, L. F. (1998) The effect of large-scale flow on low-level frontal structure and evolution in midlatitude cyclones. *Monthly Weather Review* 126(7), 1767–1791. (Cited on page 45.)

Schulz, J.-P. (2008) Revision of the Turbulent Gust Diagnostics in the COSMO Model. Technical Report 8. Deutscher Wetterdienst Offenbach a. M., Germany. (Cited on page 101.)

Schulz, J.-P. and Heise, E. (2003) A New Scheme for Diagnosing Near-Surface Convective Gusts. Technical Report 3. Deutscher Wetterdienst Offenbach a. M., Germany. (Cited on page 101.)

Schwierz, C.; Koellner-Heck, P.; Mutter, E. Z.; Bresch, D. N.; Vidale, P.; Wild, M.; and Schaer, C. (2010) Modelling European winter wind storm losses in current and future climate. *Climatic Change* 101, 485–514. (Cited on pages 80, 81, 121, 122 and 123.)

Seidel, D. J.; Fu, Q.; Randel, W. J.; and Reichler, T. J. (2008) Widening of the tropical belt in a changing climate. *Nature Geoscience* 1(1), 21–24. (Cited on pages 45 and 47.)

Selten, F. M.; Branstator, G. W.; Dijkstra, H. A.; and Kliphuis, M. (2004) Tropical origins for recent and future Northern Hemisphere climate change. *Geophysical Research Letters* 31(21), L21205. (Cited on pages 47, 75 and 128.)

Sienz, F.; Schneidereit, A.; Blender, R.; Fraedrich, K.; and Lunkeit, F. (2010) Extreme value statistics for North Atlantic cyclones. *Tellus A* 62(4), 347–360. (Cited on page 42.)

Stephenson, D. B.; Pavan, V.; Collins, M.; Junge, M. M.; and Quadrelli, R. (2006) North Atlantic Oscillation response to transient greenhouse gas forcing and the impact on European winter climate: a CMIP2 multi-model assessment. *Climate Dynamics* 27(4), 401–420. (Cited on pages 46 and 72.)

Steppeler, J.; Doms, G.; Schättler, U.; Bitzer, H. W.; Gassmann, A.; Damrath, U.; and Gregoric, G. (2003) Meso-gamma scale forecasts using the nonhydrostatic model LM. *Meteorology and Atmospheric Physics* 82(1-4), 75–96. (Cited on page 84.)

Timmermann, A.; Latif, M.; Voss, R.; and Grotzner, A. (1998) Northern Hemispheric interdecadal variability: A coupled air-sea mode. *Journal of Climate* 11(8), 1906–1931. (Cited on page 47.)

Uccellini, L. W. and Johnson, D. R. (1979) Coupling of Upper and Lower Tropospheric Jet Streaks and Implications For the Development of Severe Convective Storms. *Monthly Weather Review* 107(6), 682–703. (Cited on page 45.)

Ulbrich, U. and Christoph, M. (1999) A shift of the NAO and increasing storm track activity over Europe due to anthropogenic greenhouse gas forcing. *Climate Dynamics* 15(7), 551–559. (Cited on pages 46, 47, 55, 56, 72 and 73.)

Ulbrich, U.; Fink, A. H.; Klawa, M.; and Pinto, J. G. (2001) Three extreme storms over Europe in December 1999. *Weather* 56(3), 70–80. (Cited on page 45.)

Ulbrich, U.; Pinto, J. G.; Kupfer, H.; Leckebusch, G. C.; Spangehl, T.; and Reyers, M. (2008) Changing northern hemisphere storm tracks in an ensemble of IPCC climate change simulations. *Journal of Climate* 21(8), 1669–1679. (Cited on page 42.)

Ulbrich, U.; Leckebusch, G. C.; and Pinto, J. G. (2009) Extra-tropical cyclones in the present and future climate: a review. *Theoretical and Applied Climatology* 96(1-2), 117–131. (Cited on pages 2 and 101.)

UNEP (2004) Impacts of summer 2003 heat wave in Europe. Report 2. (Cited on page 1.)

Uppala, S. M.; Kallberg, P. W.; Simmons, A. J.; Andrae, U.; Bechtold, V. D.; Fiorino, M.; Gibson, J. K.; Haseler, J.; Hernandez, A.; Kelly, G. A.; Li, X.; Onogi, K.; Saarinen, S.; Sokka, N.; Allan, R. P.; Andersson, E.; Arpe, K.; Balmaseda, M. A.; Beljaars, A. C. M.; Van De Berg, L.; Bidlot, J.; Bormann, N.; Caires, S.; Chevallier, F.; Dethof, A.; Dragosavac, M.; Fisher, M.; Fuentes, M.; Hagemann, S.; Holm, E.; Hoskins, B. J.; Isaksen, L.; Janssen, P. A. E. M.; Jenne, R.; McNally, A. P.; Mahfouf, J. F.; Morcrette, J. J.; Rayner, N. A.; Saunders, R. W.; Simon, P.; Sterl, A.; Trenberth, K. E.; Untch, A.; Vasiljevic, D.; Viterbo, P.; and Woollen, J. (2005) The ERA-40 re-analysis. *Quarterly Journal Of The Royal Meteorological Society* 131(612), 2961–3012. (Cited on page 11.)

van der Linden, P.; Mitchell, J.; and Gilbert, P. (2009) ENSEMBLES - Climate change and its impacts. Final report. Met Office Hadley Centre. (Cited on pages 11, 12, 48, 83, 84 and 126.)

Visbeck, M. H.; Hurrell, J. W.; Polvani, L.; and Cullen, H. M. (2001) The North Atlantic Oscillation: Past, present, and future. *Proceedings of the National Academy of Sciences of the United States of America* 98(23), 12876–12877. (Cited on page 46.)

Walker, G.T. (1924) Correlation in seasonal variation of weather. *IX Memoirs of the India Meteorological Department* 25, 275–332. (Cited on page 48.)

Walker, G.T. and Bliss, E.W. (1932) World Weather V. *Memoirs of the Royal Meteorological Society* 4(36), 53–84. (Cited on pages 45, 46, 48 and 72.)

Wang, X. L.; Wan, H.; Zwiers, F. W.; Swail, V. R.; Compo, G. P.; Allan, R. J.; Vose, R. S.; Jourdain, S.; and Yin, X. (2011) Trends and low-frequency variability of storminess over western Europe, 1878-2007. *Climate Dynamics* 37(11-12), 2355–2371. (Cited on page 73.)

Wang, X. L. L.; Zwiers, F. W.; Swail, V. R.; and Feng, Y. (2009) Trends and variability of storminess in the Northeast Atlantic region, 1874-2007. *Climate Dynamics* 33(7-8), 1179–1195. (Cited on page 73.)

Wanner, H.; Bronnimann, S.; Casty, C.; Gyalistras, D.; Luterbacher, J.; Schmutz, C.; Stephenson, D. B.; and Xoplaki, E. (2001) North Atlantic Oscillation - Concepts and studies. *Surveys In Geophysics* 22(4), 321–382. (Cited on pages 46 and 73.)

Wu, W.; Lynch, A. H.; and Rivers, A. (2005) Estimating the Uncertainty in a Regional Climate Model Related to Initial and Lateral Boundary Conditions. *Journal of Climate* 18(7), 917–933. (Cited on page 122.)

Wu, Y.; Ting, M.; Seager, R.; Huang, H.-P.; and Cane, M. A. (2010) Changes in storm tracks and energy transports in a warmer climate simulated by the GFDL CM2.1 model. *Climate Dynamics* 37(1-2), 53–72. (Cited on page 47.)

Yin, J. H. (2005) A consistent poleward shift of the storm tracks in simulations of 21st century climate. *Geophysical Research Letters* 32(18), L18701. (Cited on pages 47, 49, 55 and 74.)

Appendix A

Supplementary Material

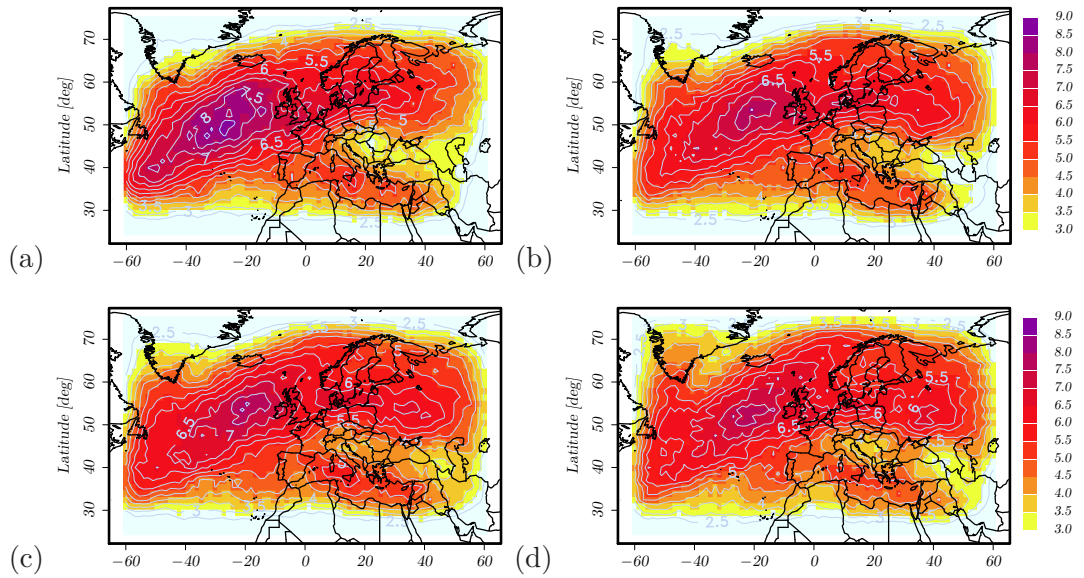

Figure A.1: Additional Figure for Section 2.3: Track density (in units of tracks per year) of identified winter storm events in the extended winter season October through March for (a) ERA Interim (1979-2010) with a resolution of 0.7° x 0.7°, (b) ERA 40 (1958-2001) with a resolution of 1.125° x 1.125°, (c) ERA 40 interpolated to a 2.5° x 2.5° grid, (d) ERA 40 interpolated to a 3.5° x 3.5° grid.

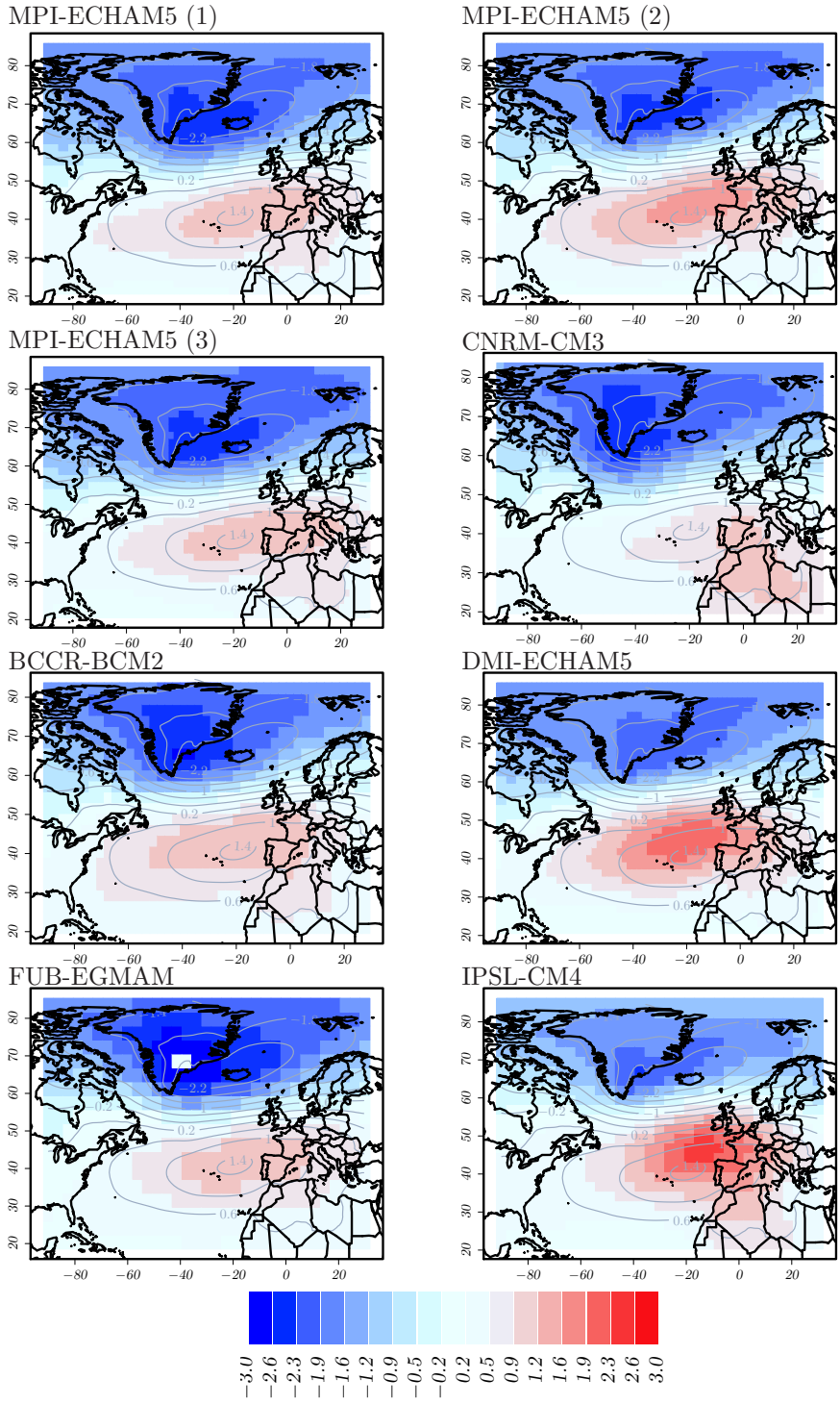

Figure A.2: Additional Figure for Section 3.3.1: NAO patterns derived from the individual GCM simulations. Patterns are calculated as the leading EOF using monthly mean MSLP fields for October through March for the reference period 1971-2000 under recent climate conditions.

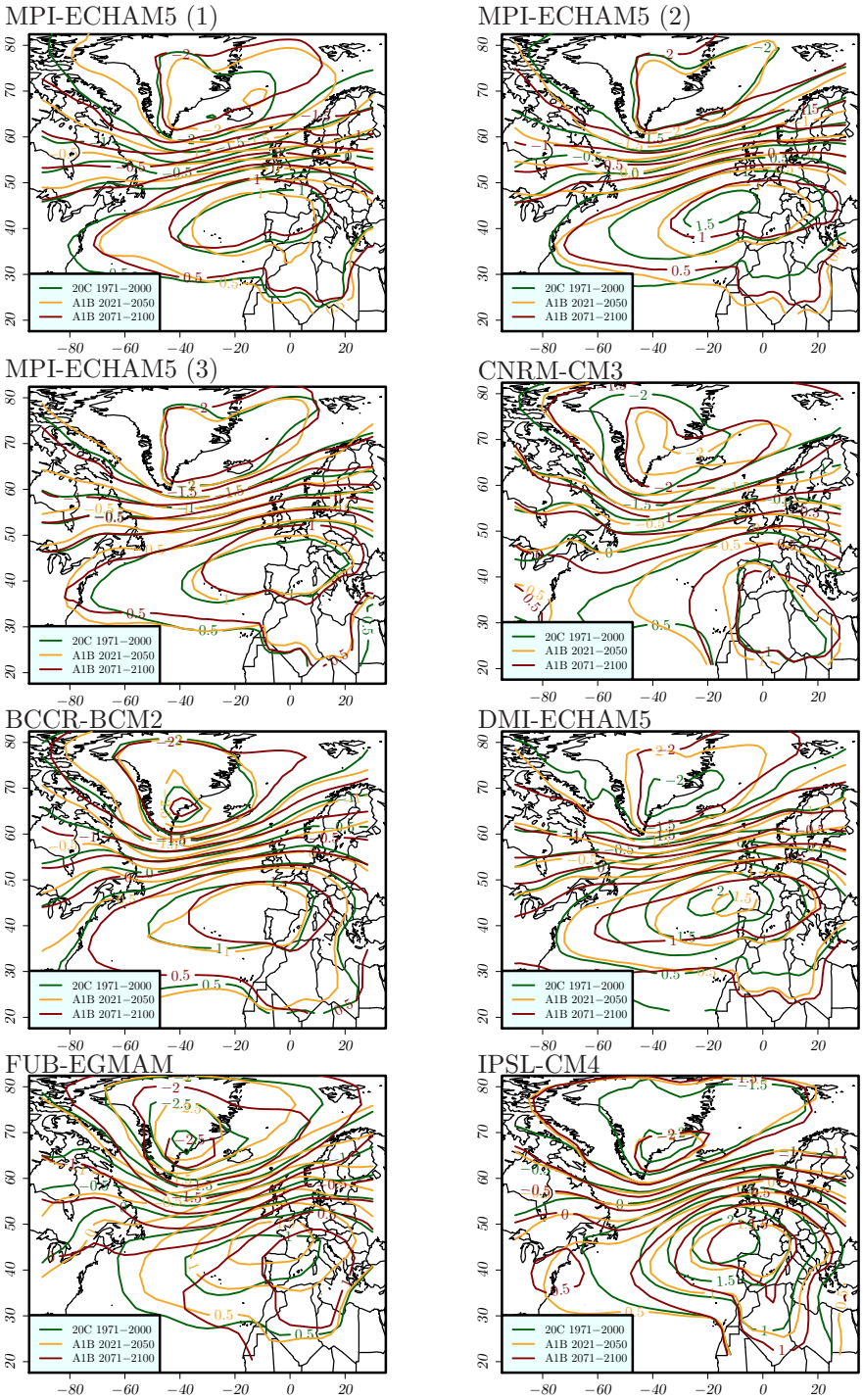

Figure A.3: Additional Figure for Section 3.3.3: Changes in the NAO pattern, calculated as the leading EOF of monthly MSLP fields for the individual GCM simulations. Green contours show patterns derived from recent climate simulations (1971-2000), yellow and red contours show the corresponding patterns for SRES-A1B conditions for 2021-2050 and 2071-2100 respectively.

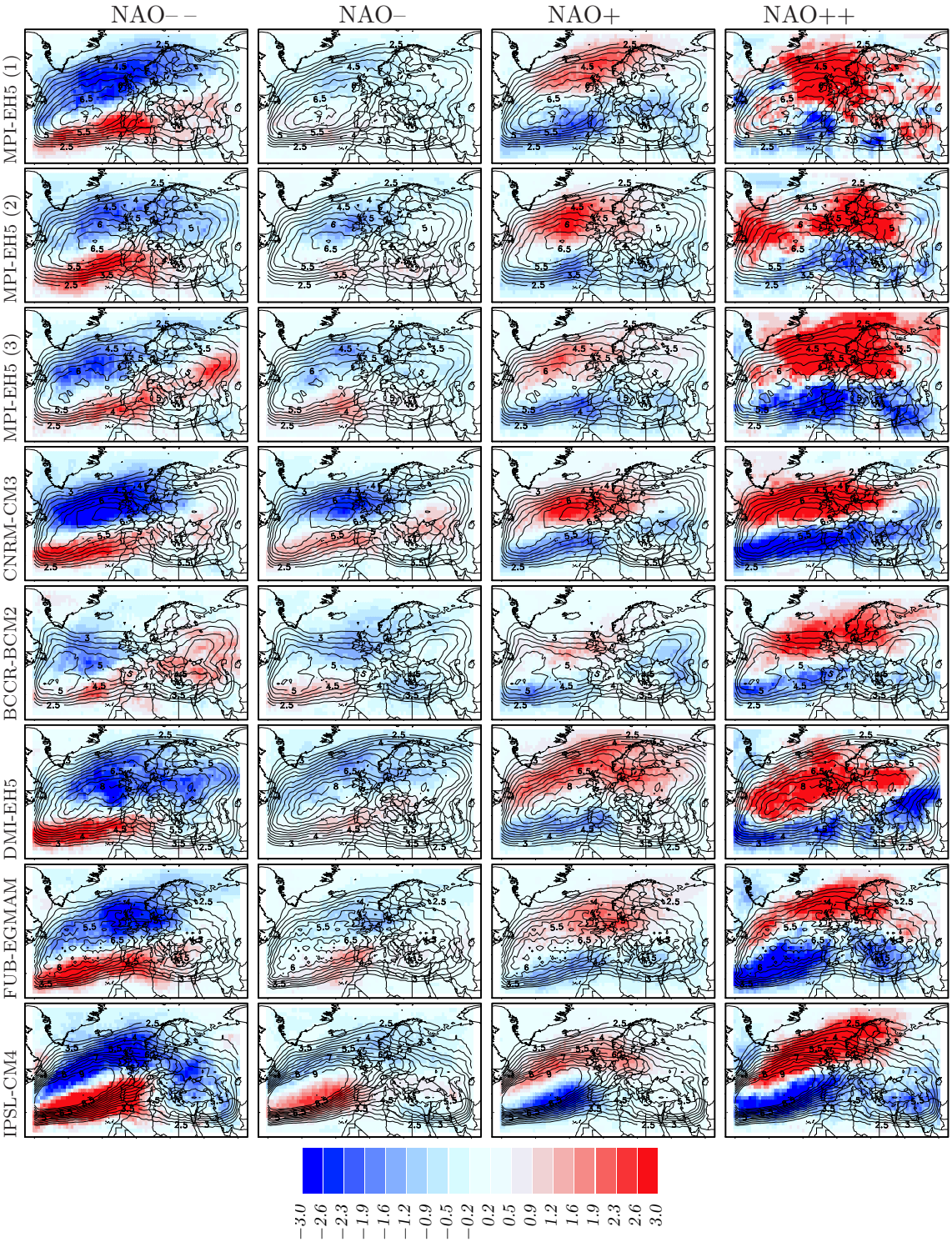

Figure A.4: Additional Figure for Section 3.5.1: Difference of track density composites (tracks per year) to climatological track density shown in black isolines. Track density composites are calculated for the different NAO phases according to Table 3.2.

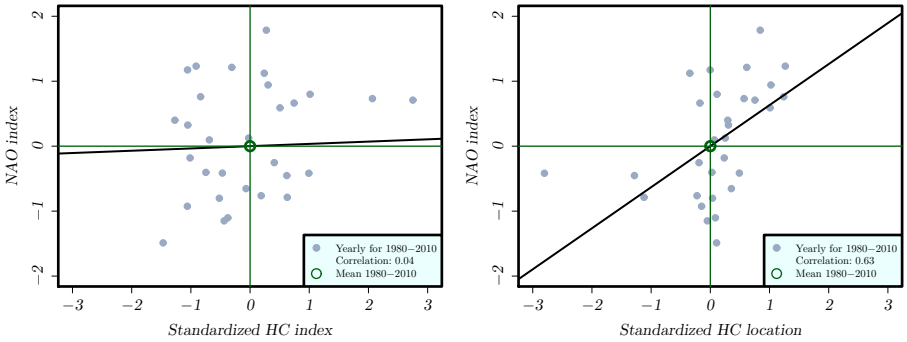

Figure A.5: Additional Figure for Section 3.6.2: Dependence of the NAO index on the standardized Hadley cell strength index (left) and on the standardized displacement of the Hadley cell's northward boundary (right) for ERA-Interim (1979-2010).

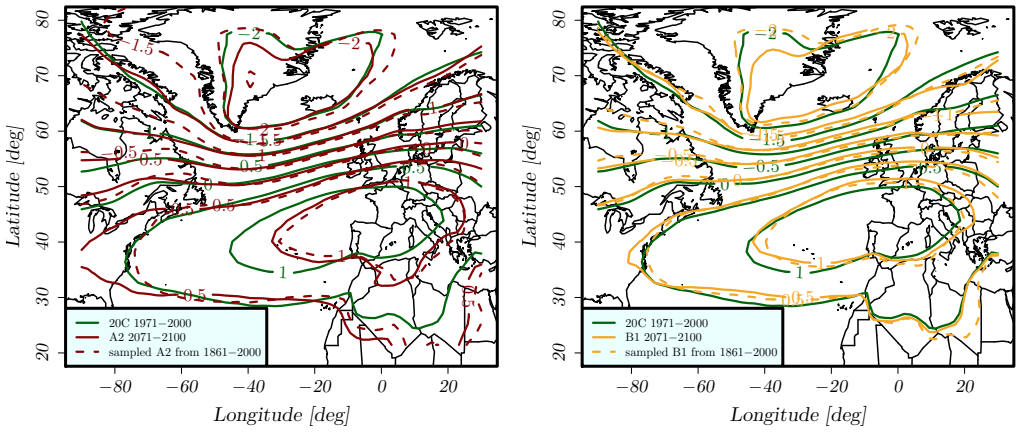

Figure A.6: Additional Figure for Section 3.6.2: Same as Figure 3.14 (right) for the SRES-A2 scenario (left) and for the SRES-B1 scenario (right).

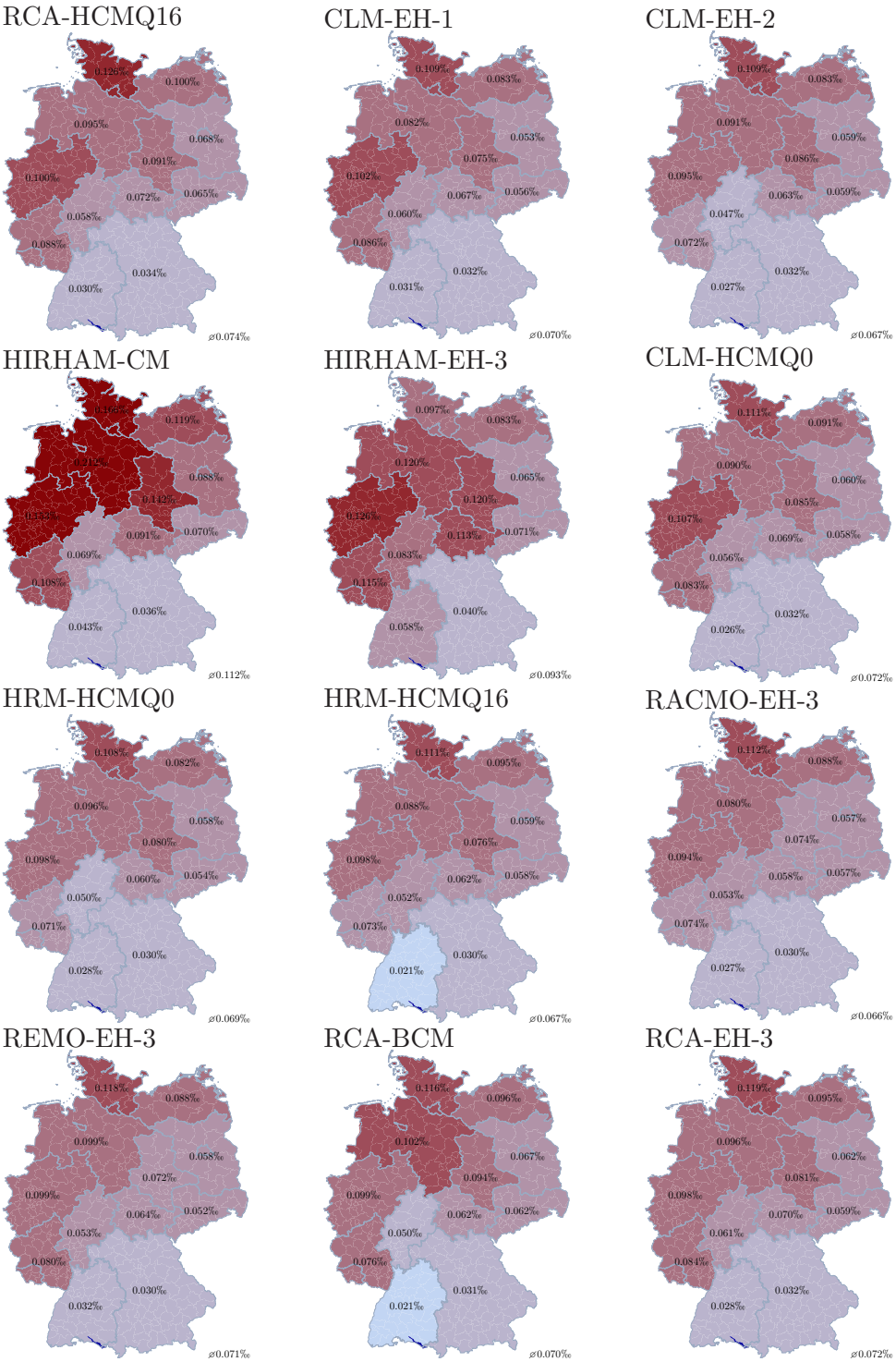

Figure A.7: Additional Figure for Section 4.5.2: Mean yearly loss ratio in ‰, as modeled from the individual RCM simulations under recent climate conditions (1971-2000).

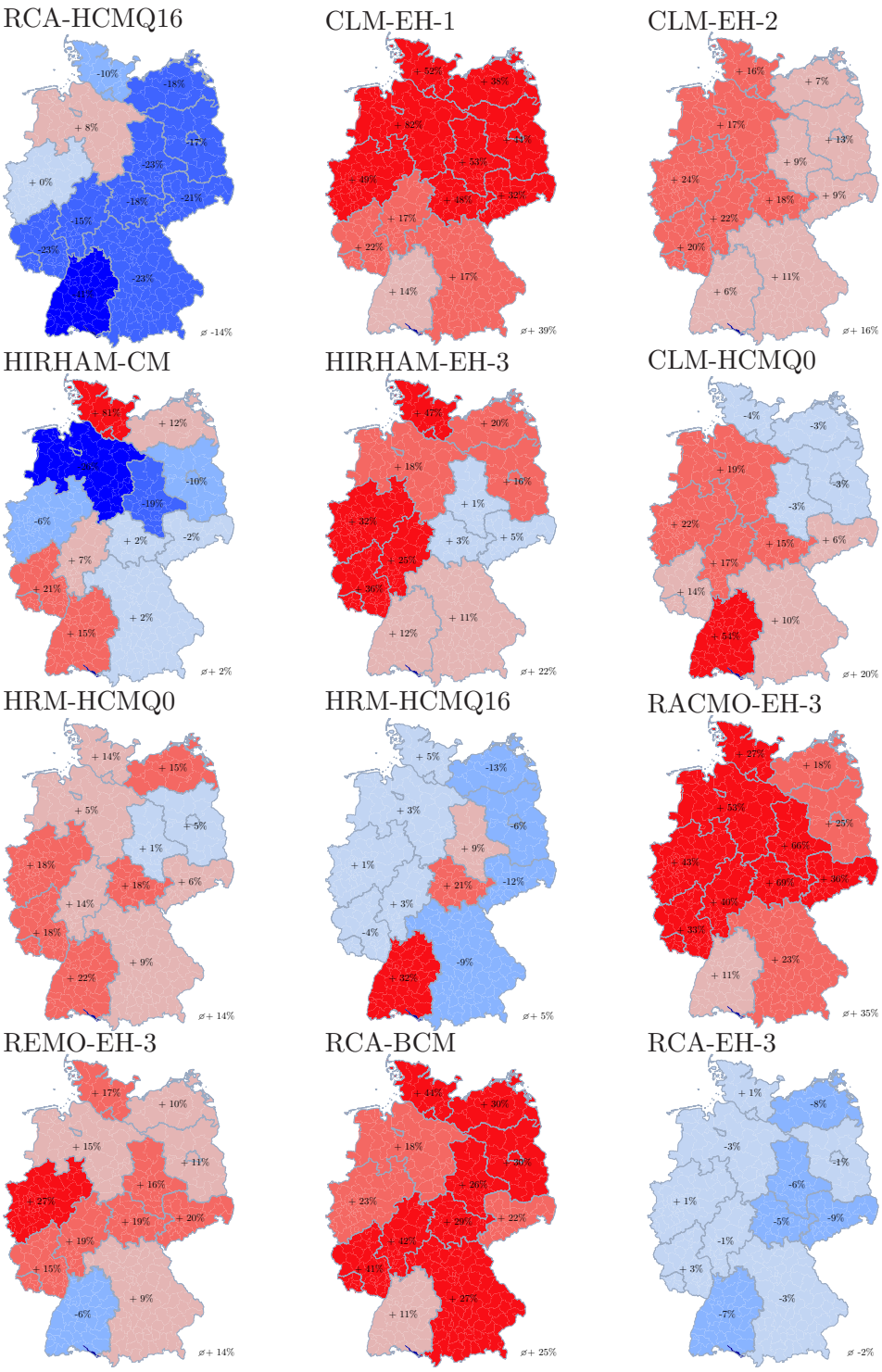

Figure A.8: Additional Figure for 4.5.3: Relative difference (%) in mean yearly losses projected for 2071-2100 analyzing the individual RCM simulations under SRES-A1B conditions.

Acknowledgement

I wish to thank Uwe Ulbrich and Gregor Leckebusch for giving me the possibility to create this thesis. I much appreciate your support and supervision during the past years, giving me the opportunity to work in exciting projects contributing much to my learning process. Also, I wish to express my thanks to Peter Névir for sharing his thoughts in many fruitful discussions over lunch. I like to thank the former and present members of my working group, in particular Markus Donat, Daniel Befort, Dominik Renggli, Tim Kruschke, Henning Rust and Martin Göber for valuable discussions, fruitful exchange of thoughts but especially for creating a pleasant working atmosphere during the past years. Finally, I am deeply grateful to my parents, my family and especially Susanne for far too much to be listed here.